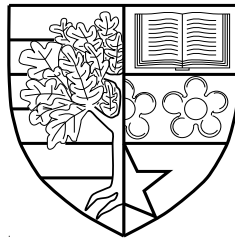


Propagation Channel Characterisation and Modelling for High-Speed Train Communication Systems

by

Ammar Ghazal



Submitted for the degree of Doctor of Philosophy
at

Heriot-Watt University

School of Engineering and Physical Sciences

September 2015

The copyright in this thesis is owned by the author. Any quotation from the thesis or use of any of the information contained in it must acknowledge this thesis as the source of the quotation or information.

Abstract

High-mobility scenarios, e.g., High-Speed Train (HST) scenarios, are expected to be typical scenarios for the Fifth Generation (5G) communication systems. With the rapid development of HSTs, an increasing volume of wireless communication data is required to be transferred to train passengers. HST users demand high network capacity and reliable communication services regardless of their locations or speeds, which are beyond the capability of current HST communication systems. The features of HST channels are significantly different from those of low-mobility cellular communication systems. For a proper design and evaluation of future HST wireless communication systems, we need accurate channel models that can mimic the underlying channel characteristics, especially the non-stationarity for different HST scenarios. Inspired by the lack of such accurate HST channel models in the literature, this PhD project is devoted to the modelling and simulation of non-stationary Multiple-Input Multiple-Output (MIMO) channels for HST communication systems.

In this thesis, we first give a comprehensive review of the measurement campaigns conducted in different HST scenarios and address the recent advances in HST channel models. We also highlight the key challenges of HST channel measurements and models. Then, we study the characterisation of non-stationary channels and propose a theoretical framework for deriving the statistical properties of these channels.

HST wireless communication systems encounter different channel conditions due to the difference of surrounding geographical environments or scenarios. HST channel models in the literature have either considered large-scale parameters only and/or neglected the non-stationarity of HST channels and/or only consider one of the HST scenarios. Therefore, we propose a novel generic non-stationary Geometry-Based Stochastic Model (GBSM) for wideband MIMO HST channels in different HST scenarios, i.e., open space, viaduct, and cutting. The corresponding simulation model is then developed with angular parameters calculated by the Modified Method of Equal Area (MMEA). The system functions and statistical properties of the proposed channel models are thoroughly studied. The proposed generic non-stationary HST channel models are verified by measurements in terms of stationary time for the open space scenario and the Autocorrelation Function (ACF), Level Crossing Rate (LCR), and stationary distance for the viaduct and cutting scenarios.

Transmission techniques which are capable of utilising Three-Dimensional (3D) spatial dimensions are significant for the development of future communication systems. Consequently, 3D MIMO channel models are critical for the development and evaluation of these techniques. Therefore, we propose a novel 3D generic non-stationary GBSM for wideband MIMO HST channels in the most common HST scenarios. The corresponding simulation model is then developed with angular parameters calculated by the Method of Equal Volume (MEV). The proposed models considers several time-varying channel parameters, such as the angular parameters, the number of taps, the Ricean K -factor, and the actual distance between the Transmitter (Tx) and Receiver (Rx). Based on the proposed generic models, we investigate the impact of the elevation angle on some of the channel statistical properties. The proposed 3D generic models are verified using relevant measurement data.

Most standard channel models in the literature, like Universal Mobile Telecommunications System (UMTS), COST 2100, and IMT-2000 failed to introduce any of the HST scenarios. Even for the standard channel models which introduced a HST scenario, like IMT-Advanced (IMT-A) and WINNER II channel models, they offer stationary intervals that are noticeably longer than those in measured HST channels. This has inspired us to propose a non-stationary IMT-A channel model with time-varying parameters including the number of clusters, powers, delays of the clusters, and angular parameters. Based on the proposed non-stationary IMT-A channel model, important statistical properties, i.e., the time-variant spatial Cross-correlation Function (CCF) and time-variant ACF, are derived and analysed. Simulation results demonstrate that the stationary interval of the developed non-stationary IMT-A channel model can match that of relevant HST measurement data.

In summary, the proposed theoretical and simulation models are indispensable for the design, testing, and performance evaluation of 5G high-mobility wireless communication systems in general and HST ones in specific.

To Dana, Joud, Lama, Hazem, and my parents

Acknowledgments

My greatest appreciation goes to my primary supervisor Prof. Cheng-Xiang Wang for the guidance, encouragement, and the support he gave for accomplishing this work. Your constructive feedbacks have helped me in my endeavour. Special thanks are also extended to my second and local supervisors, Prof. Harald Haas and Dr. Mohamed Khaled Chahine, respectively, for the help and support they have offered throughout my course of study.

I am extremely delighted to have the privilege of knowing my colleagues of past and present in the Advanced Wireless Technologies (AWiTec) Group, namely, Xuemin Hong, Xiang Cheng, Zengmao Chen, Omar Salih, Margaret Anyaegbu, Pat Chambers, Yi Yuan, Yu Fu, Fourat Haider, Ahmed Al-Kinani, Shangbin Wu, Sandy Weir, Yan Zhang, and Qianru Zhou. I thank all of you for sharing wonderful moments and hope our friendship will last forever.

Finally, I also wish to convey my heartfelt gratitude and appreciation to my parents, Abdulhamid Ghazal & Sooad Alhajji, my wife, Dana Khartabil, my son, Joud Ghazal, and my friends for their ultimate support and unconditional love. You represent the true treasure in my life. Many thanks and best wishes to all of you.

Ammar Ghazal

Edinburgh, September 2015.

Declaration of Authorship

I, Ammar Ghazal, declare that this thesis titled, ‘Propagation Channel Characterisation and Modelling for High-Speed Train Communication Systems’ and the work presented in it are my own. I confirm that:

- This work was done wholly while in candidature for a research degree at Heriot-Watt University.
- Where I have consulted the published work of others, this is always clearly attributed.
- Where I have quoted from the work of others, the source is always given. With the exception of such quotations, this thesis is entirely my own work.
- I have acknowledged all main sources of help.
- Where the thesis is based on work done by myself jointly with others, I have made clear exactly what was done by others and what I have contributed myself.

Signed:

Date:

Contents

Abstract	i
Acknowledgments	iv
Declaration of Authorship	v
List of Figures	x
List of Tables	xiii
Abbreviations	xiv
Symbols	xviii
1 Introduction	1
1.1 Background	1
1.2 Motivation	4
1.3 Contributions	5
1.4 Publications	7
1.4.1 Journals	7
1.4.2 Conferences	8
1.5 Thesis Organisation	8
2 Channel Measurements and Models for High-Speed Train Communication Systems	10
2.1 Introduction	10
2.2 HST Channel Measurements	11
2.2.1 HST Propagation Scenarios	12
2.2.2 Channel Statistics	16
2.2.3 Measurement's Setup Parameters	17
2.3 HST Channel Models	17

2.3.1	Large-Scale Fading Models	19
2.3.2	Cellular Architectures and Scenarios	19
2.3.3	Modelling Approaches of HST Small-Scale Fading Models	21
2.3.3.1	Deterministic channel models	21
2.3.3.2	GBSMs	23
2.3.3.3	NGSMs	24
2.4	Research Gaps in HST Channel Measurements and Models	24
2.4.1	Non-Stationarity of HST Channels	24
2.4.2	Statistical Properties of HST Channels	25
2.4.3	HST Scenarios	25
2.4.4	3D HST Channel Models	26
2.5	Summary	26
3	Characterisation of Non-Stationary MIMO Channels	27
3.1	Introduction	27
3.2	System Functions of Non-WSSUS Channels	28
3.3	Correlation Functions of Non-WSSUS Channels	29
3.4	System Functions and Correlation Functions of Non-Stationary MIMO Channels	33
3.5	Summary	36
4	A Generic 2D Non-Stationary Wideband MIMO Channel Model for Different High-Speed Train Scenarios	37
4.1	Introduction	37
4.2	The Non-Stationary Wideband Theoretical GBSM	40
4.2.1	Description of the Wideband MIMO Theoretical Model	40
4.2.1.1	Open space	46
4.2.1.2	Viaduct	46
4.2.1.3	Cutting	47
4.2.2	Statistical Properties of the Theoretical Model	48
4.2.2.1	Time-variant ST CF	49
4.2.2.2	Time-variant SD PSD	51
4.2.2.3	LSF	51
4.2.2.4	Time-variant LCR	53
4.3	The Simulation Model for Wideband MIMO HST channels	54
4.3.1	Description of the Wideband MIMO Simulation Model	54
4.3.2	Statistical Properties of the Simulation Model	56
4.3.2.1	Time-variant ST CF	56
4.3.2.2	Time-variant SD PSD	57
4.3.2.3	LSF	57
4.3.2.4	Time-variant LCR	58
4.4	Results and Analysis	58
4.4.1	Open space	59
4.4.1.1	Time-variant ST CFs	59

4.4.1.2	Time-variant SD PSDs	62
4.4.1.3	LSFs	63
4.4.1.4	Stationary Interval/Stationary Distance	64
4.4.2	Viaduct	66
4.4.2.1	Time-variant ACF	66
4.4.2.2	Time-variant LCR	66
4.4.3	Cutting	68
4.4.3.1	Time-variant ACF	68
4.4.3.2	Time-variant LCR	68
4.4.3.3	Stationary Distance	69
4.5	Summary	70
5	A Generic 3D Non-Stationary Wideband MIMO Channel Model for Different High-Speed Train Scenarios	72
5.1	Introduction	72
5.2	Novel 3D Wideband Non-stationary MIMO HST Theoretical Channel Models	74
5.2.1	Description of the 3D Wideband MIMO Theoretical Model	74
5.2.1.1	First tap	76
5.2.1.2	Other taps	78
5.2.2	Time-varying Channel Parameters	81
5.2.2.1	The total number of taps	81
5.2.2.2	Time-varying distance between BS and MRS	83
5.2.2.3	Time-varying AoDs and AoAs	83
5.2.2.4	Time-varying Ricean K-factor	85
5.2.3	Statistical Properties of the Proposed 3D Wideband Non-stationary MIMO HST Channel Model	85
5.2.3.1	Time-variant ST CF	85
5.2.3.2	Time-variant ACF	87
5.2.3.3	Time-variant space CCF	87
5.3	3D Non-stationary Wideband Simulation Model for MIMO HST Channels	88
5.3.1	Description of the 3D Wideband MIMO Simulation Model	88
5.3.2	Statistical Properties of The 3D Simulation Model	90
5.3.2.1	Time-variant ST CF	90
5.3.2.2	Time-variant ACF	91
5.3.2.3	Time-variant space CCF	92
5.4	Results and Analysis	92
5.4.1	Time-variant ACF	94
5.4.2	Time-variant space CCF	95
5.4.3	Stationary Interval	97
5.5	Summary	98
6	A Non-Stationary IMT-Advanced MIMO Channel Model for High-Mobility Wireless Communication Systems	99

6.1	Introduction	99
6.2	Overview of The Original IMT-A MIMO Channel Model	102
6.3	A Novel Non-Stationary IMT-A Channel Model with Time-Varying Parameters	103
6.3.1	Update MCs and MS locations	105
6.3.2	The number of clusters	107
6.3.3	Time-varying delays	110
6.3.4	Time-varying power of clusters	111
6.3.5	Time-varying AoDs	111
6.3.6	Time-varying AoAs	112
6.4	Statistical Properties of Non-Stationary IMT-A MIMO Channel Models	113
6.4.1	Local spatial CCF	113
6.4.2	Local temporal ACF	114
6.4.3	Stationary Interval	114
6.5	Simulation Results and Analysis	115
6.5.1	Local spatial CCF	115
6.5.2	Local temporal ACF	115
6.5.3	Stationary Interval	117
6.6	Summary	120
7	Conclusions and Future Work	121
7.1	Summary of Results	121
7.2	Future Research Topics	124
7.2.1	Channel Measurements and Models for HST-to-HST Commu- nication	124
7.2.2	Massive MIMO for HST Communication Systems	124
7.2.3	Tunnel Scenario	125
7.2.4	Indoor Scenario	125
	References	127

List of Figures

2.1	Classification of HST Scenarios.	13
2.2	Three typical HST propagation scenarios: (a) viaduct, (b) cutting, and (c) tunnel.	15
2.3	A HST communication system deploying MRSs.	20
2.4	Classification of non-stationary HST channel models	21
3.1	Relationship of system functions for non-WSSUS channels	29
3.2	Relationship of CFs for non-WSSUS channels	30
3.3	Relationship of 6D CFs and LSF for non-WSSUS channels	32
3.4	Relationship of 6D CFs and channel CF for non-WSSUS channels	32
3.5	Relationship of CFs for non-stationary channels	34
3.6	Characterisation of non-stationary channels	35
3.7	Relationship for CFs for WSSUS channel models	35
4.1	A HST communication system deploying MRSs.	41
4.2	The GBSM for a wideband MIMO HST channel.	42
4.3	The time-varying angular parameters in the HST channel model.	45
4.4	The viaduct scenario.	46
4.5	The cutting scenario.	47
4.6	(a) The absolute values of the time-variant space CCF of different taps of the proposed HST channel model at different time instants. (b) The absolute values of the time-variant space CCF of the second tap with/without time-varying angular parameters.	60
4.7	Comparison between the time-variant space CCFs of the second tap of the theoretical model and simulation model for different time instants.	60
4.8	(a) The absolute values of the time-variant ACF of different taps of the proposed HST channel model at different time instants. (b) The absolute values of the time-variant ACF with/without time-varying angular parameters.	61
4.9	Comparison between the time-variant ACFs of the second tap of the theoretical model and simulation model for different time instants.	62
4.10	Time-variant SD PSDs of the theoretical model for different scenarios ($v_R = 360$ km/h, $f_{\max} = 1.34$ KHz): isotropic: $k_R = 0$ & non-isotropic: $k_R = 3$ & 11.	63

4.11	Time-variant SD PSDs of the theoretical and simulation models for different angular parameters ($v_R = 360$ km/h, $f_{\max} = 1.34$ KHz, $k_R = 11$).	63
4.12	Comparison between the LSFs of the second tap of the theoretical model and the simulation model for different time instants.	64
4.13	The empirical CCDFs of stationary intervals for the proposed HST simulation model and a measured HST channel [77].	65
4.14	The absolute values of the time-variant ACFs of the generic HST channel model a measured HST channel in viaduct scenario [63] ($f_c = 930$ MHz, $v_R = 180$ km/h, $L = 15$ m, $H_{\text{viad}} = 20$ m, $H_{\text{BS}} = 44$ m, $H_{\text{MRS}} = 30$ cm, $H_{\text{train}} = 3.8$ m, $D_{BP} = 400$ m, $\gamma_R = 0$, $\beta_R = \beta_T = 45^\circ$, $\mu_R^{(i)}(t_0) = 63^\circ$, $k_R^{(i)} = 2.7$, $N = 50$).	67
4.15	The LCRs of the generic HST channel model and a measured HST channel in viaduct scenario [63] ($f_c = 930$ MHz, $v_R = 180$ km/h, $L = 15$ m, $H_{\text{viad}} = 20$ m, $H_{\text{BS}} = 44$ m, $H_{\text{MRS}} = 30$ cm, $H_{\text{train}} = 3.8$ m, $D_{BP} = 400$ m, $\gamma_R = 0$, $\beta_R = \beta_T = 60^\circ$, $\mu_R^{(i)}(t_0) = 85^\circ$, $k_R^{(i)} = 7.3$, $N = 50$).	67
4.16	The absolute values of the time-variant ACFs of the generic HST channel model for different cuttings' dimensions [71] (Cutting 1: $W_{\text{up}} = 53.93$ m & $W_{\text{down}} = 14.78$ m, Cutting 2: $W_{\text{up}} = 58.30$ m & $W_{\text{down}} = 15.16$ m, $f_c = 930$ MHz, $v_R = 260$ km/h, $L = 15$ m, $H_{\text{cut}} = 7.1$ m, $H_{\text{BS}} = 28$ m, $H_{\text{MRS}} = 30$ cm, $H_{\text{train}} = 3.8$ m, $D_{BP} = 200$ m, $\gamma_R = 0$, $\beta_R = \beta_T = 45^\circ$, $\mu_R^{(i)}(t_0) = 63^\circ$, $k_R^{(i)} = 15$, $N = 50$).	69
4.17	The LCRs of the generic HST channel model and a measured HST channel in cutting scenario [71] ($f_c = 930$ MHz, $v_R = 260$ km/h, $L = 15$ m, $H_{\text{cut}} = 7.1$ m, $H_{\text{BS}} = 28$ m, $H_{\text{MRS}} = 30$ cm, $H_{\text{train}} = 3.8$ m, $W_{\text{up}} = 53.93$ m, $W_{\text{down}} = 14.78$ m, $D_{BP} = 200$ m, $\gamma_R = 0$, $\beta_R = \beta_T = 60^\circ$, $\mu_R^{(i)}(t_0) = 145^\circ$, $k_R^{(i)} = 4$, $N = 50$).	70
4.18	The stationary distances of the generic HST channel model in viaduct and cutting scenarios (viaduct: $f_c = 1.890$ GHz, $v_R = 285$ km/h, $L = 15$ m, $H_{\text{viad}} = 20$ m, $H_{\text{BS}} = 20$ m, $H_{\text{MRS}} = 30$ cm, $H_{\text{train}} = 3.8$ m, cutting: $f_c = 2.35$ GHz, $v_R = 200$ km/h, $L = 20$ m, $H_{\text{cut}} = 5$ m, $H_{\text{BS}} = 28$ m, $H_{\text{MRS}} = 30$ cm, $H_{\text{train}} = 3.8$ m, $W_{\text{up}} = 40$ m, $W_{\text{down}} = 16$ m).	71
5.1	HST communication system in cutting scenario with LoS and single-bounced rays.	75
5.2	The proposed 3D Generic RS-GBSM combining circular-cylinder and multiple confocal elliptic-cylinder models with LoS, single-bounced rays for a wideband MIMO HST channel (Blue solid line: tap 1; Green dash-dot line: tap 2).	75
5.3	The detailed geometry of the single-bounced rays in the circular-cylinder and the second tap elliptic-cylinder model (Blue solid line: tap 1; Green dash-dot line: tap 2).	76
5.4	The total number of taps $I(t)$ as a function of distance from BS.	83

5.5	The absolute values of the time-variant ACF of the 3D theoretical model, the 3D simulation model, the 3D simulation result, and the 2D simulation model in (a) open space scenario, (b) viaduct scenario, and (c) cutting scenario.	94
5.6	The absolute values of the time-variant ACF of the proposed 3D theoretical model, the proposed 3D simulation model, and the corresponding 3D simulation result in cutting scenario at different time instants.	95
5.7	The absolute values of the time-variant space CCF of the 3D theoretical model, the 3D simulation model, the 3D simulation result, and the 2D simulation model in (a) open space scenario, (b) viaduct scenario, and (c) cutting scenario.	96
5.8	The empirical CCDFs of stationary intervals for the proposed 3D HST simulation model, the 2D HST simulation model, and a measured HST channel.	97
6.1	BS and MS angular parameters in the IMT-A channel model.	105
6.2	The non-stationary IMT-A channel coefficients generation procedure.	106
6.3	Time-varying clusters with death/birth process. ($N(t_0) = 20$, $\lambda_G = 0.8/\text{m}$, $\lambda_R = 0.04/\text{m}$, $v_{MS} = 60\text{ m/s}$, $v_A = 15\text{ m/s}$, $v_Z = 5\text{ m/s}$, and $P_c = 0.3$)	109
6.4	The total number of clusters $N(t)$ vs. time. ($N(t_0) = 20$, $\lambda_G = 0.8/\text{m}$, $\lambda_R = 0.04/\text{m}$, $v_{MS} = 60\text{ m/s}$, $v_A = 15\text{ m/s}$, $v_Z = 5\text{ m/s}$, and $P_c = 0.3$)	109
6.5	The absolute value of the local spatial CCFs of the non-stationary IMT-A channel model (UMa NLoS scenario, $\phi_{n,m}(t_0) = \text{random}$, $c(t_0) = 100\text{ m}$, $\theta_c = 15^\circ$, $v_c = 30\text{ m/s}$, $\varphi_{n,m}(t_0) = \text{random}$, $a(t_0) = 150\text{ m}$, $\theta_v = 120^\circ$, and $v = 20\text{ m/s}$).	116
6.6	The analytical and simulated local spatial CCFs of the non-stationary IMT-A at different time instants (UMa NLoS scenario, $\phi_{n,m}(t_0) = \text{random}$, $c(t_0) = 100\text{ m}$, $\theta_c = 15^\circ$, $v_c = 30\text{ m/s}$, $\varphi_{n,m}(t_0) = \text{random}$, $a(t_0) = 150\text{ m}$, $\theta_v = 120^\circ$, and $v = 20\text{ m/s}$).	117
6.7	The absolute value of the local temporal ACFs of the non-stationary IMT-A channel model (UMa NLoS scenario, $\phi_{n,m}(t_0) = \text{random}$, $c(t_0) = 100\text{ m}$, $\theta_c = 15^\circ$, $v_c = 30\text{ m/s}$, $\varphi_{n,m}(t_0) = \text{random}$, $a(t_0) = 70\text{ m}$, $\theta_{MC} = -140^\circ$, $v_{MC} = 5\text{ m/s}$, $\theta_{MS} = 120^\circ$, and $v_{MS} = 20\text{ m/s}$).	118
6.8	The analytical and simulated local temporal ACFs of the non-stationary IMT-A at different time instants (UMa NLoS scenario, $\phi_{n,m}(t_0) = \text{random}$, $c(t_0) = 100\text{ m}$, $\theta_c = 15^\circ$, $v_c = 30\text{ m/s}$, $\varphi_{n,m}(t_0) = \text{random}$, $a(t_0) = 70\text{ m}$, $\theta_{MC} = -140^\circ$, $v_{MC} = 5\text{ m/s}$, $\theta_{MS} = 120^\circ$, and $v_{MS} = 20\text{ m/s}$).	119
6.9	The empirical CCDF of stationary intervals for the proposed non-stationary IMT-A model, the original IMT-A model, and a measured HST channel ($f_c = 2\text{ GHz}$, $v = 90\text{ m/s}$, $N_{PDP} = 15$, $c_{\text{thresh}} = 0.8$).	119
6.10	The empirical CCDF of stationary intervals for the original IMT-A model and the proposed non-stationary IMT-A model with all time-variant parameters, time-variant delays and powers, and time-variant angular parameters ($f_c = 2\text{ GHz}$, $v = 60\text{ m/s}$, $N_{PDP} = 15$, $c_{\text{thresh}} = 0.8$).	120

List of Tables

2.1	Important HST channel measurements.	12
2.2	PL and shadow fading models for HST channels.	18
2.3	Important HST small-scale fading channel models.	19
4.1	Definition of parameters in Fig. 4.2.	42
4.2	Typical values of parameters in Figs. 4.4 & 4.5.	48
5.1	Definition of parameters in Figs. 5.2 and 5.3.	77
6.1	Definitions of channel parameters in Fig. 6.1.	104

Abbreviations

2D	Two-Dimensional
3D	Three-Dimensional
3GPP	3rd Generation Partnership Project
4D	four-Dimensional
5D	five-Dimensional
5G	Fifth Generation
6D	six-Dimensional
AAoA	Azimuth AoA
AAoD	Azimuth AoD
ACF	Autocorrelation Function
AFD	Average Fade Duration
AoA	Angle of Arrival
AoD	Angle of Departure
APDP	Averaged Power Delay Profile
BER	Bit Error Rate
BS	Base Station
CCDF	Complementary Cumulative Distribution Function
CCF	Cross-correlation Function
CF	Correlation Function

CIR	Channel Impulse Response
CoMP	Coordinated Multi-Point
DAS	Distributed Antenna System
DS	Delay Spread
EAoA	Elevation AoA
EAoD	Elevation AoD
EM	Electro-Magnetic
EMEDS	Extended Method of Exact Doppler Spread
FD	Fade Depth
FDTD	Finite-Difference Time-Domain
FLoS	Far Line-of-Sight
FS	Frequency Selectivity
GBDM	Geometry-Based Deterministic Model
GBSM	Geometry-Based Stochastic Model
GSM-R	Global System for Mobile Communication Railway
HST	High-Speed Train
i.i.d.	Independent and Identically Distributed
IMT-A	IMT-Advanced
InH	Indoor Hotspot
IS-GBSM	Irregular-Shaped Geometry-Based Stochastic Model
ITS	Intelligent Transportation Systems
LCR	Level Crossing Rate
LoS	line-of-Sight
LPNM	L_p -Norm Method

LSF	Local Scattering Function
LTE-A	Long-Term Evolution-Advanced
LTE-R	Long-Term Evolution-Railway
MC	Moving Cluster
MEV	Method of Equal Volume
MIMO	Multiple-Input Multiple-Output
MISO	Multiple-Input Single-Output
MMEA	Modified Method of Equal Area
MPC	Multi-Path Component
MRS	Mobile Relay Station
MS	Mobile Station
NGSM	Non-Geometrical Stochastic Model
NLoS	Non-Line-of-Sight
PDF	Probability Density Function
PDP	Power Delay Profile
PL	Path Loss
PSD	Power Spectrum Density
RAU	Radio Antenna Unit
RMa	Rural Macro-cell
RoF	Radio over Fiber
RS-GBSM	Regular-Shaped Geometry-Based Stochastic Model
Rx	Receiver
SB	Single-Bounced
SCM	Spatial Channel Model
SCM-E	SCM-Extension
SD	Space Doppler

SF	Shadow Fading
SIMO	Single-Input Multiple-Output
SISO	Single-Input Single-Output
SMa	Suburban Macro-cell
SNR	Signal-to-Noise Ratio
SoS	Sum-of-Sinusoids
SSP	Small-Scale Parameters
ST	Space-Time
TDL	Tapped Delay Line
Tx	Transmitter
ULA	Unifrom Linear Array
UMa	Urban Macro-cell
UMi	Urban Micro-cell
UMTS	Universal Mobile Telecommunications System
US	Uncorrelated Scattering
V2I	Vehicle-to-Infrastructure
V2R	Vehicle-to-Roadside
V2V	Vehicle-to-Vehicle
VMF	von Mises-Fisher
WSS	Wide Sense Stationary
WSSUS	Wide Sense Stationary Uncorrelated Scattering
ZoA	Zenith Angles of Arrival
ZoD	Zenith Angles of Departure

Symbols

$(\cdot)^*$	complex conjugate
$\dot{(\cdot)}$	first derivative
$\cosh(\cdot)$	hyperbolic cosine function
$\text{erf}(\cdot)$	error function
$\tilde{(\cdot)}$	corresponding parameters of stochastic simulation models
$ \cdot $	absolute value (amplitude) of a complex vector
$\mathbf{max}\{\cdot\}$	maximum value of a vector
$\mathbf{min}\{\cdot\}$	minimum value of a vector
v_R	MRS speed
γ_R	MRS angle of motion
τ	delay
τ_i	delay of the i th tap
τ_{pq}	waves travel time through the link $T_p - R_q$
τ_{pq,n_i}	waves travel time through the link $T_p - s^{(n_i)} - R_q$
$\tau_{pq,n_{1,m}}(t)$	waves travel times through the link $T_p - s^{(n_{1,m})} - T_q$
$\tau_{pq,n_{i,2}}$	waves travel time through the link $T_p - s^{(n_{i,2})} - T_q$
τ_n	delay of the n th cluster
ν	Doppler frequency
Ω	direction of an antenna element in an antenna array
$\delta_{P,k}$	movement of the MC and MS
$\delta_{MC,k}$	movement of the MC

$\delta_{MS,k}$	movement of the MS
Δd_s	antenna elements spacing at the BS in IMT-A
Δd_u	antenna elements spacing at the MRS in IMT-A
Δt	time difference (time lag)
$\Delta \tau$	delay lag
Δf	frequency lag
$\Delta \nu$	Doppler lag
Δx	space lag (antenna element spacing)
Δx_T	antenna element spacings of the BS
Δx_R	antenna element spacings of the MRS
$\Delta \varphi_{n,m}$	AoA offset
$\Delta \phi_{n,m}$	AoD offset
$\Delta \Omega$	direction lag
$\rho(t, \tau; \Delta x)$	time-delay-variant space CCF
$\rho(t, \Delta x_T, \Delta x_R)$	time-variant space CCF
$\rho^{\text{LoS}}(t, \Delta x_T, \Delta x_R)$	time-variant space CCF of the LoS component
$\rho^{\text{SBi}}(t, \Delta x_T, \Delta x_R)$	space CCF of the SB components of i th tap
$\rho_{s_2 u_2}^{s_1 u_1}(\Delta d_s, \Delta d_u, \tau)$	ST CF between $h_{s_1 u_1}(t)$ and $h_{s_2 u_2}(t)$
β_R	tilt angles of the MRS antenna array
β_T	tilt angles of the BS antenna array
ϕ	azimuth angle of the VMF PDF
$\phi_{T_p}^{\text{LoS}}(t)$	AoA of the LoS path
$\phi_R^{(n_i)}(t)$	AoA of the wave travelling from $s^{(n_i)}$ to the MRS
$\phi_T^{(n_i)}(t)$	AoD of the wave that impinges on $s^{(n_i)}$
$\phi_{T_p}^{\text{LoS}}(t)$	AoA of the LoS path in 2D model
ϕ_R^{LoS}	AAoA of the LoS paths in 3D model
$\phi_T^{(n_i, m)}$	AAoD of the waves that impinge on $s^{(n_i, m)}$
$\phi_R^{(n_i, m)}$	AAoA of the waves travelling from $s^{(n_i, m)}$
ϕ_{LoS}	LoS AoD in IMT-A
$\phi_{n,m}(t)$	AoD related to the m th ray within the n th cluster in IMT-A
$\Phi_{n,m}$	random phase m th ray within the n th cluster

φ_{LoS}	LoS AoA in IMT-A
$\varphi_{n,m}(t)$	AoA related to the m th ray within the n th cluster in IMT-A
φ_R^{LoS}	E AoA of the LoS paths in 3D model
$\varphi_T^{(n_i,m)}$	E AoD of the waves that impinge on $s^{(n_i,m)}$
$\varphi_R^{(n_i,m)}$	E AoA of the waves travelling from $s^{(n_i,m)}$
φ	elevation angle of the VMF PDF
ξ	distance $d(T_p, \text{MRS})$
$\xi_T^{(n_i)}(t)$	distance $d(\text{BS}, s^{(n_i)})$
$\xi_R^{(n_i)}(t)$	distance $d(s^{(n_i)}, \text{MRS})$
ξ_n	per cluster shadowing term in dB
ε_{pq}	distance $d(T_p, R_q)$
ε_{pn_i}	distance $d(T_p, s^{(n_i)})$
$\varepsilon_{n_i q}$	distance $d(s^{(n_i)}, R_q)$
$\Omega_{i,pq}$	mean power for the i th tap
ψ_{n_i}	phase of the n th SB in the i th tap
$\mu_R^{(i)}$	mean angular value of the AoA in the i th tap
θ_T	orientation of the BS antenna array in the x - y plane
θ_R	orientation of the MRS antenna array in the x - y plane
θ_A	MC A direction of travel
θ_Z	MC Z direction of travel
θ_{MS}	MS direction of travel
$\theta_{MS/Z}$	MS direction of travel relative to MC Z
η_{SB_i}	power-related parameter of i th single-bounced ray
$\eta_{SB_{1,i}}$	power-related parameter of i th single-bounced ray in first tap
$\eta_{SB_{l,i}}$	power-related parameter of i th single-bounced ray in l th tap
λ	carrier wavelength
λ_G	generation rate of new clusters
λ_R	recombination rate of existing clusters
σ_{DS}	delay spread
$v_{n,m}$	Doppler frequency component related to the m th ray within the n th cluster in IMT-A

a_i	semi-major axis of the i th ellipse
$a(t_0)$	initial distance between MC Z and MS
$A_H(\Delta t, \Delta f, \Delta \tau, \Delta \nu)$	channel CF
b_i	semi-minor axis of the i th ellipse
c	speed of light
$c(t_0)$	initial distance between BS and MC A
c_{thresh}	threshold of the correlation coefficient
$C_H(t, f, x, \tau, \nu, \Omega)$	LSF
D_s	distance between the BS and MRS
D_{min}	minimum distance between the BS and the mid of the railway track
D_{proj}	projection of D_s on the railway track plane
D_{ver}	vertical distance between the bottom of the BS and the projection of the MRS location on the railway track plane
D_{BP}	breakpoint distance
$D_{\text{BS}}(t)$	distance between the BS and MC A
$D_{\text{MS}}(t)$	distance between the MS and MC Z
$D_{\text{LoS}}(t)$	distance of the LoS components between BS and MS
$E\{\cdot\}$	statistical expectation
f	frequency
$f(\phi, \varphi)$	3D VMF PDF
f_c	carrier frequency
f_s	half length of the distance between the two foci of ellipses
f_{max}	maximum Doppler shift related to the MRS
h	relative height between BS and MRS
$h(t, \tau, x)$	space-time-variant channel impulse response
$h_{pq}(t)$	complex tap coefficients between the p th and q th antenna elements
$h_{p'q'}(t)$	complex tap coefficients between the p' th and q' th antenna elements
$h_{1,pq}^{\text{LoS}}(t)$	complex tap coefficients of the LoS component

$h_{i,pq}^{\text{SB}}(t)$	complex tap coefficients of the SB components of the the i th tap
$h_{i,pq}(t)$	complex space-time-variant tap coefficients of the i th tap
$h_{pq}^I(t)$	in-phase component of the complex fading envelope $h_{pq}(t)$
$h_{pq}^Q(t)$	quadrature component of the complex fading envelope $h_{pq}(t)$
$H(f, \nu, x)$	space-variant Doppler-spread transfer function
$h_{u,s}(t, \tau)$	complex tap coefficients between the s th and u th antenna elements in IMT-A
$h_{u,s,n}(t)$	complex tap coefficients between the s th and u th antenna elements in the n th tap
H_{BS}	height of the BS
H_{cut}	height of the cutting
H_{MRS}	height of the MRS
H_{train}	height of the HST
H_{viad}	height of the viaduct
I	total number of taps
$I_0(\cdot)$	zeroth-order modified Bessel function of the first kind
k	a parameter of VMF PDF that controls the angle spread
$k^{(i,1)}$	a parameter of VMF PDF at the Rx sphere in 1th tap
$k^{(i,2)}$	a parameter of VMF PDF at the i th elliptic-cylinder
K_{pq}	Ricean factor
L	distance between the BS and the railway track
$L(r)$	envelope LCR
$L(t, r)$	time-variant LCR
$L_H(t, f, x)$	space-time-variant transfer function
m	m th sub-path
M	total number of sub-paths (irresolvable rays)
n	n th effective scatterers
N_i	total number of effective scatterers on the i th tap
N_1	number of effective scatterers around the Rx lying on a sphere
N_2	number of effective scatterers lying on an elliptic-cylinder
N_{PDP}	number of power delay profiles to be averaged

$N_{\text{new},k}$	number of new clusters at time t_k
$\overline{P}_h(t_k, \tau)$	APDP of $\tilde{h}_{pq}(t_k, \tau)$
P_c	percentage of moving clusters
P_n	power of the n th cluster
$r(t, \tau; \Delta t)$	time-delay-variant ACF
$r(t, \Delta t)$	time-variant ACF
$r^{\text{LoS}}(t, \Delta t)$	time-variant ACF of the LoS component
$r^{\text{SB}_i}(t, \Delta t)$	time-variant ACF of the SB components of i th tap
r_{DS}	delay distribution proportionality factor
$R_h(t, \tau, \Delta t, \Delta x)$	time-delay-variant space-time CF
$R_h(t, \tau, x; \Delta t, \Delta x)$	space-time-delay-variant space-time CF
$R_h(t, \tau; \Delta t, \Delta \tau, \Delta x)$	time-delay-variant space-time-delay CF
$R_h(t, \Delta x_T, \Delta x_R, \Delta t)$	ST CF
$R_h^{\text{LoS}}(t, \Delta x_T, \Delta x_R, \Delta t)$	ST CF of the LoS component
$R_h^{\text{SB}_i}(t, \Delta x_T, \Delta x_R, \Delta t)$	ST CF of the SB components of i th tap
$R_L(t; \Delta t, \Delta f, \Delta x)$	time-variant space-time-frequency CF
$R_L(t, f; \Delta t, \Delta f, \Delta x)$	time-frequency-variant space-time-frequency CF
$R_L(t, x; \Delta t, \Delta f, \Delta x)$	space-time-variant space-time-frequency CF
R_q	q th antenna element of the MRS array
R_R	radius of the circular-cylinder around the MRS
$s^{(n_i)}$	n_i th effective scatterer located on the i th ellipse
$s^{(n_{i,1})}$	$n_{i,1}$ th effective scatterer located on the Rx sphere
$s^{(n_{i,2})}$	$n_{i,2}$ th effective scatterer located on the i th elliptic-cylinder
S	Tx antenna array
$SD(t_k)$	stationary distance
$S_H(\nu, \tau, x)$	space-variant Doppler-spread impulse response
t	time
t_k	time of the k -th drop (snapshot)
T_p	p th antenna element of the BS array
$T_s(t_k)$	stationary interval
U	Rx antenna array

\vec{v}_A	velocity vector of MC A
\vec{v}_Z	velocity vector of MC Z
\vec{v}_{MS}	velocity vector of MS
v_R	Rx velocity
v_A	MC A velocity
v_Z	MC Z velocity
v_{MS}	MS velocity
$v_{MS/Z}$	MS velocity relative to MC Z
$W(t, \tau, \nu, \Delta x)$	time-delay variant SD PSD
$W(t, \nu, \Delta x_T, \Delta x_R)$	time-variant SD PSD
$W^{\text{LoS}}(t, \nu, \Delta x_T, \Delta x_R)$	time-variant SD PSD of the LoS component
$W^{\text{SB}i}(t, \nu, \Delta x_T, \Delta x_R)$	time-variant SD PSD of the SB components of i th tap
$W(t, \tau, \Omega)$	time-variant direction-spread impulse response
W_{down}	width of the cutting's bottom
W_{up}	width of the cutting's crown
W_{viad}	width of the viaduct
x	space
$X(\nu, \tau, \Omega)$	direction-Dopplerspread impulse response
$Y(t, f, \Omega)$	time-variant direction-spread transfer function
$Z(f, \nu, \Omega)$	direction-Doppler-spread transfer function

Introduction

1.1 Background

The Fifth Generation (5G) communication systems are requested to meet new and unprecedented demands beyond the capability of existing communication systems [1]. Among these demands are the capability of delivering a consistent experience across a variety of scenarios including the cases of high traffic volume density, high connection density, and high mobility [2], [3]. Furthermore, 5G communication systems are required to provide reliable communication services and achieve high peak data rates as ambitious as 1 Gb/s for high-mobility scenarios [1], e.g., High-Speed Train (HST) and highway. To meet these requirements future HST wireless communication systems have to overcome many challenges resulting from the high speed of the train that can easily exceed 250 km/h, such as fast handover, fast travel through widely diverse scenarios, large Doppler shifts, and large delay spreads [4]–[6] besides some challenges inherited from conventional trains such as high penetration losses, limited visibility in tunnels, and the harsh electromagnetic environment [7].

Since 1998, the Global System for Mobile Communication Railway (GSM-R) has widely been adopted as Europe’s standard for train communications and control. However, GSM-R can only provide a data rate of up to 200 kbps [8], besides the fact that it is mainly used for train control rather than providing communications for

train passengers [9]. Therefore, GSM-R cannot meet the requirements for future high speed data transmissions [10] and International Union of Railways has recommended that GSM-R has to be replaced by Long-Term Evolution-Railway (LTE-R) [11]–[14], which is a broadband railway wireless communication system based on Long-Term Evolution-Advanced (LTE-A) [15]. LTE-R is expected to offer higher data capacity than GSM-R and reduced deployment and maintenance costs [16]. Nevertheless, both systems still adopt the conventional cellular architecture where the Mobile Station (MS) inside trains communicates directly with the outdoor Base Station (BS). Such an architecture leads to a spotty coverage and high penetration losses of wireless signals traveling through the metal carriages of HSTs. In addition, the receiving signals at MSs on board will experience fast changing channels resulting in high signaling overhead and high possibility of drop calls and handover failure [17].

The aforementioned problems can be mitigated by deploying other cellular architectures, such as Distributed Antenna System (DAS) [18]–[20], Coordinated Multi-Point (CoMP) [21], [22], Mobile Relay Station (MRS) [23]–[26] (or Mobile Femtocell [1], [27], [28]) technologies, or a combination of these architectures, e.g., DAS with MRS [29] or CoMP with MRS [30]. In a DAS, distributed antenna elements are connected to a BS via wires or fibers (Radio over Fiber (RoF)) [31], [32] to provide considerable gain in coverage and capacity in comparison with the conventional cellular architecture. The spatially separated antenna elements can be used to transmit the same signal at different locations to provide spatial diversity against fading. Combined with spatial diversity, frequency reuse in the DAS is an effective technique to increase system capacity. The enhancement in spectral efficiency of DASs in comparison with conventional systems was presented in [18]. In [19], the authors analysed the deployment of DAS over HST communication systems and some of the resulting problems such as the coverage of the Radio Antenna Unit (RAU) and echo channel effect. In CoMP systems, the transmission of neighbouring BSs will be coordinated in the downlink while the received signals at the uplink will be jointly processed. This will reduce the inter-cell interference and improve the cell edge throughput. CoMP systems will also provide an enhanced channel capacity by using the statistically independent properties of the channels resulting from the wide spatial separation of antenna elements.

Adopting mobile Femtocell architecture in HST communication systems can be performed by deploying dedicated MRSs on the surface of the train to extend the coverage of the outdoor BS into train carriages. In this case, the BS will mainly communicate with the MRS at high data rates instead of communicating with large numbers of MSs directly. An MRS and its associated MSs within a train carriage are all viewed as a single unit to the BS, while the MSs will see the relevant MRS as a regular BS. It follows that an MRS can perform a group handover on behalf of all its associated MSs, which can greatly reduce the frequent handover burden of the HST system [28]. Since the complexity of radio resource allocation (i.e., transmit power, data rates, scheduling, power and frequency allocation, and antenna selection) in a BS is related to the number of active users [18], the radio resource management complexity in one BS will be reduced significantly when dealing with a “group of users” rather than individuals. This promising MRS technology has been adopted by IMT-Advanced (IMT-A) [33] and WINNER II [34] and recommended to be supported by future IMT systems [35].

The Path Loss (PL) and multipath effects are in disparity under various propagation environments, leading to the impossibility of accurate predictions under different propagation environments with the same channel model. Therefore, radio wave propagation scene partitioning plays an important role in wireless channel modeling [36]. Special HST scenarios such as cuttings, viaducts, and tunnels have significant impact on the propagation characteristics. HSTs can operate across one or more of these scenarios during its travel. Most standard channel models in the literature, like the Universal Mobile Telecommunications System (UMTS) [37], COST 2100 [38], and IMT-2000 [39], failed to introduce any of the HST scenarios. The moving networks scenario in the WINNER II channel model [34] and Rural Macro-cell (RMa) scenario in the IMT-A channel model [33] have only considered a rural environment for HSTs, while neglecting other HST scenarios.

The prerequisite of any wideband mobile radio system is a thorough knowledge of the propagation characteristics of the mobile radio channel. The features of HST channels, e.g., non-stationarity and large Doppler shift, are significantly different from those

of low-mobility mobile cellular communication channels. Therefore, novel channel models of HST wireless channels are indispensable for the design and the development of future HST communication systems.

1.2 Motivation

Accurate channel models that are able to mimic key characteristics of wireless channels play an important role in designing and testing HST communication systems. They are also indispensable in evaluating different algorithms and transmission schemes, such as diversity of transmission/reception, error correction coding, interleaving, and equalisation algorithms. Inaccurate channel models may lead to over-optimistic or over-pessimistic performance evaluation results that will result in misjudgments in product development. Moreover, inaccurate channel models may lead to inaccurate link budgets that will result in huge errors of the estimated maximum distance between adjacent BSs. Consequently, this will cause poor coverage and increased drop calls due to failed handovers between BSs when the distance is underestimated and unnecessary overlapped coverage area with unjustified installation and maintenance cost of the extra installed BSs when the distance is overestimated.

Multiple-Input Multiple-Output (MIMO) technology, in which multiple antennas are deployed at both the Tx and Rx, presents an attractive solution for meeting the requirements of next generation wireless communication systems for the high speed railway. Since a high speed data rate in the future railways and the bandwidth resources for the railway are limited, the capacity cannot be improved through increasing bandwidth. Therefore, MIMO is considered as an effective technique in LTE-R to ensure the efficiency and reliability for data transmissions [40]. The channel measurement, particularly the MIMO channel measurement at high moving speeds, remains to be challenging task. Furthermore, MIMO channel models for HSTs based on measurements has not been completed yet and no standard HST channel models have been developed yet.

In Geometry-Based Stochastic Model (GBSM), the impulse responses of wireless channels are characterised by the law of wave propagation applied to specific Transmitter (Tx), Receiver (Rx), and scatterer geometries. These geometries are predefined in a stochastic fashion according to certain probability distributions. Due to their close agreement with measurements, reasonable complexity, and mathematical traceability, GBSMs have been widely used to simulate wireless channels in different propagation environments.

Due to lack of accurate generic wideband MIMO HST channel models that take into account the non-stationarity of the communication channel due to the high-mobility of the MSs or MRSs, this PhD project is devoted to the modelling and simulation of non-stationary MIMO channels for HST communication systems using the geometry-based modelling approach.

1.3 Contributions

The key contributions of the thesis are summarised as follows:

- Review the measurement campaigns conducted in different HST scenarios and address the recent advances in HST channel models. Important existing channel models are reviewed and classified. Research gaps in HST channel measurements and models are discussed and outlined.
- Propose a novel theoretical framework for deriving the system functions and correlation functions of non-stationary channels.
- Propose a generic theoretical GBSM for wideband non-stationary MIMO HST channels in the most common HST scenarios, i.e., the open space, the viaduct, and the cutting scenarios. The proposed model has time-varying angular parameters, time-varying Ricean K -factor, and time-varying distance between the Tx and the Rx. Comprehensive statistical properties are derived and thoroughly for the novel theoretical GBSM in open space scenario, i.e., time-variant

Space-Time (ST) Correlation Function (CF), time-variant Space Doppler (SD) Power Spectrum Density (PSD), and Local Scattering Function (LSF).

- Develop a corresponding Sum-of-Sinusoids (SoS) based simulation model for wideband non-stationary MIMO HST channels with reasonable complexity, i.e., a finite number of sinusoids or effective scatterers. The angle parameters of the proposed simulation model are calculated by adopting the Modified Method of Equal Area (MMEA).
- Derive the relevant statistical properties of the developed simulation model, verify them by simulations, and compare with those of the proposed theoretical GBSM. Furthermore, the utility of the proposed simulation model is validated using measurement data.
- Propose a novel generic Three-Dimensional (3D) wideband non-stationary MIMO HST GBSM for HST channels in different HST scenarios. The proposed 3D model considers several time-varying parameters such as, the angular parameters, the number of taps, the Ricean K -factor, and the distance between Tx and Rx.
- Derive the statistical properties of the proposed 3D simulation model, verify them by simulations, and compare with those of the proposed theoretical 3D non-stationary HST GBSM. Furthermore, the utility of the proposed 3D simulation model is validated using relevant measurement data.
- Develop a non-stationary IMT-A channel model with time-varying small-scale parameters, i.e., the number of clusters, delays, the power of each cluster, angular parameters.
- Derive and analyse important statistical properties of the proposed non-stationary IMT-A channel model, i.e., the local spatial Cross-correlation Function (CCF) and local temporal Autocorrelation Function (ACF) are derived and analysed.
- Investigate the stationary interval of the proposed non-stationary IMT-A channel model and compare it with the one of the standard IMT-A channel model and with a measurement data.

1.4 Publications

The work presented in this thesis has led to the following publications:

1.4.1 Journals

1. **A. Ghazal**, C.-X. Wang, B. Ai, D. Yuan, and H. Haas, “A non-stationary wideband MIMO channel model for high-mobility intelligent transportation systems,” *IEEE Trans. Intell. Transp. Syst.*, vol. 16, no. 2, pp. 885–897, Apr. 2015.
2. C. X. Wang, **A. Ghazal**, B. Ai, Y. Liu, and P. Fan, “Channel measurements and models for high-speed train communication systems: a survey,” *IEEE Commun. Surveys Tuts.*, submitted for publication.
3. Y. Fu, C.-X. Wang, **A. Ghazal**, H. M. Aggoune, and M. M. Alwakeel, “Performance investigation of spatial modulation systems under non-stationary wideband high-speed train channel models,” *IEEE Trans. Wireless Commun.*, submitted for publication.
4. **A. Ghazal**, Y. Yuan, C.-X. Wang, Y. Zhang, Q. Yao, H. Zhou, and W. Duan, “A non-stationary IMT-Advanced MIMO channel model for high-mobility wireless communication systems,” *IEEE Trans. Wireless Commun.*, to be submitted.
5. **A. Ghazal**, C.-X. Wang, B. Ai, P. Fan, and Y. Yang “A generic 3D non-stationary MIMO channel model for different high-speed train scenarios,” *IEEE Trans. Wireless Commun.*, to be submitted.
6. Y. Liu, **A. Ghazal**, C. X. Wang, X. Ge, and Y. Yang, “Channel measurements and models for high-speed train wireless communication systems in tunnel scenarios,” *IEEE Wireless Commun. Mag.*, to be submitted.

7. Y. Zhang, **A. Ghazal**, C.-X. Wang, H. Zhou, and W. Duan, “Complexity analysis of the original and non-stationary IMT-Advanced MIMO channel models,” *IEEE Trans. Wireless Commun.*, to be submitted.

1.4.2 Conferences

1. **A. Ghazal**, C.-X. Wang, Y. Liu, P. Fan, and M. K. Chahine, “A generic non-stationary MIMO channel model for different high-speed train scenarios,” in *Proc. IEEE ICC’15*, Shenzhen, China.
2. **A. Ghazal**, C.-X. Wang, H. Haas, M. A. Beach, X. Lu, and D. Yuan, “A non-stationary MIMO channel model for high speed train communication systems,” in *Proc. IEEE VTC’12-Spring*, Yokohama, Japan, May. 2012, pp. 1–5.
3. **A. Ghazal**, C.-X. Wang, H. Haas, M. Beach, R. Mesleh, D. Yuan, X. Ge, and M. K. Chahine, “A non-stationary geometry-based stochastic model for MIMO high-speed train channels,” invited paper, in *Proc. ITST’12*, Taipei, Taiwan, Nov. 2012, pp. 7–11.
4. Y. Liu, C.-X. Wang, **A. Ghazal**, S. Wu, and W. Zhang, “A multi-mode waveguide tunnel channel model for high-speed train wireless communication systems,” in *Proc. EuCAP’15*, Lisbon, Spain, Apr. 2015.
5. Q. Yao, Y. Yuan, **A. Ghazal**, C.-X. Wang, L. Luan, and X. Lu, “Comparison of the statistical properties of the LTE-A and IMT-A channel models,” in *Proc. IEEE WCNC’12*, Paris, France, Apr. 2012, pp. 393–398.

1.5 Thesis Organisation

The remainder of this thesis is organised as follows:

Chapter 2 gives a comprehensive review of the measurement campaigns conducted in different HST scenarios and addresses the recent advances in HST channel models. It also highlights the research gaps in HST channel measurements and models.

Chapter 3 studies the characterisation of non-stationary channels and proposes a theoretical framework for deriving the statistical properties of these channels.

Chapter 4 introduces a novel and generic non-stationary GBSM with time-variant angular parameters for wideband MIMO HST channels in the most common HST scenarios, namely, the open space, the viaduct, and the cutting scenarios. The corresponding simulation model is then developed with angle parameters calculated by using the MMEA. The system functions and statistical properties of the proposed channel models are thoroughly investigated based on the theoretical framework in Chapter 3. Finally, this Chapter provides verifications of the proposed generic model using measurement of HST channels in different scenarios.

Chapter 5 introduces a generic 3D non-stationary GBSM for wideband MIMO HST channels. The generic channel model can describe the propagation environments for different HST scenarios with one mathematical framework by using different parameter sets. The system functions and statistical properties of the proposed channel models will also be investigated based on the theoretical framework in Chapter 3. The impact of the elevation angle on the channel statistics will be investigated and the proposed 3D simulation model will be verified using real measurement data.

Chapter 6 introduces a non-stationary IMT-A channel model for HST channels with time-varying parameters including the number of clusters, the powers and the delays of the clusters, the Angle of Departure (AoD), and the Angle of Arrival (AoA). The proposed model will be verified using relevant HST measurement data and important statistical properties will be derived and investigated thoroughly.

Finally, Chapter 7 concludes the thesis by summarising our key research findings and gives some suggestions for future research topics in wireless HST channel modelling.

Chapter 2

Channel Measurements and Models for High-Speed Train Communication Systems

2.1 Introduction

With the rapid development of HSTs, an increasing volume of wireless communication data is required to be transferred to train passengers. HST users demand high network capacity and reliable communication services regardless of their locations or speeds. To satisfy these demands, HST wireless communication systems have to overcome many challenges resulting from the high speed of the train.

The Tx and Rx of a HST wireless communication system encounter different channel conditions due to the difference of surrounding geographical environments. The HST environment can be generally classified into the following main scenarios: open space, viaduct, cutting, hilly terrain, tunnels, and stations. Considering some unique setup of the aforementioned scenarios and some other special HST scenarios, HST environment can be further classified into 12 scenarios [36]. The propagation characteristics change significantly with the change of environments and the distance between the Tx and Rx, even in the same terrain. Scenarios have close relationship with channel modelling and measurements. Most standard channel models in the literature failed

to introduce any of the HST scenarios. The moving networks scenario in the WINNER II channel model [34] and RMa scenario in the IMT-A channel model [33] have only considered a rural environment for HSTs, while neglecting other HST scenarios. The aforementioned propagation scenarios will be introduced and explained in detail in the following Section.

Many measurement campaigns have been conducted in the literature to understand the underlying physical phenomenon in HST propagation environments. Accurate channel models that are able to mimic key characteristics of wireless channels play an important role in designing and testing HST communication systems. Realistic and reliable large-scale fading channel models, i.e., PL and Shadow Fading (SF) models, are indispensable for efficient and trustworthy network deployment and optimisation. Small-scale fading channel models are crucial in physical layer design in order to develop and test different schemes, such as diversity of transmission/reception, error correction coding, interleaving, and equalisation algorithms. In the literature, several large-scale and small-scale fading HST channel models were proposed. This chapter will give a brief overview of existing HST measurement campaigns and HST propagation models. It will highlight recent advances in HST channel measurements and will introduce important approaches for the modelling and simulation of HST channels. This chapter is concluded by outlining some of the research gaps that can be found in the literature and that we will cover in this thesis.

2.2 HST Channel Measurements

Special attention has been given to HST channel measurements in recent years. Due to the high speed of the train and the hostile HST environments, conducting accurate channel measurements for HST communication systems is challenging and needs to address particular hardware and software requirements, e.g., robustness, scalability, hardware redundancy and traceability [41]. Many measurement campaigns [42]–[85] for different HST environments were presented in the literature. Here, we will briefly review and classify the important measurements for HST communications according

to the scenarios, measurements' setup parameters (i.e., antenna configuration, carrier frequency, and bandwidth), and measured channel statistics, as shown in Table 2.1.

TABLE 2.1: Important HST channel measurements.

Ref.	Scenario	Freq.	BW	Antenna	Speed	Channel Statistics
[42]	N/A	2.2 GHz	20 MHz	SISO	270 km/h	PL
[43]	N/A	2.35 GHz	100 MHz	SISO	N/A	PL, DS, K
[44]	Open space	2.6 GHz	20 MHz	SISO	370 km/h	PL, DS, DF, PDP
[46]	Open space	2.5 GHz	50 MHz	MISO	290 km/h	DS, AoA, PAS, DF
[45]	Open space	5.2 GHz	120 MHz	SIMO	350 km/h	PL, SF, K , DS, PDP, AS
[47]	Open space	930 MHz	200 kHz	SISO	350 km/h	PL, SF
[50]	Viaduct	930 MHz	200 kHz	SISO	340 km/h	PL, K
[51]	Viaduct	930 MHz	200 kHz	SISO	N/A	PL
[52], [61]	Viaduct	930 MHz	200 kHz	SISO	300 km/h	K
[53]	Viaduct	930 MHz	200 kHz	SISO	350 km/h	PL, SF
[54]–[56]	Viaduct	930 MHz	200 kHz	SISO	350 km/h	PL
[57], [64]	Viaduct	930 MHz	200 kHz	SISO	350 km/h	SF
[58]	Viaduct	930 MHz	200 kHz	SISO	300 km/h	PDF, LCR, AFD, CDF, FM
[59]	Viaduct	2.35 GHz	10 MHz	SISO	240 km/h	PL, DS, K
[62]	Viaduct	2.35 GHz	50 MHz	SISO	196 km/h	DS, K , SF
[60], [63]	Viaduct	930 MHz	200 kHz	SISO	360 km/h	PL, K , SF, FD, LCR, AFD
[65]	Viaduct	2.6 GHz	20 MHz	SISO	370 km/h	PL, SF, DS, K
[66], [67]	Viaduct	2.35 GHz	50 MHz	SISO	200 km/h	PSD, DF, K
[68]	Cutting	930 MHz	200 kHz	SISO	320 km/h	PL, SF
[69]	Cutting	930 MHz	200 kHz	SISO	350 km/h	PL, K
[70]	Cutting	930 MHz	200 kHz	SISO	295 km/h	K , FD
[71]	Cutting	930 MHz	200 kHz	SISO	350 km/h	PL, K , SF, FD, LCR, AFD
[72]	Cutting	2.35 GHz	50 MHz	SISO	200 km/h	PL, K , SF, DF
[73]	Cutting	2.35 GHz	50 MHz	SISO	200 km/h	DS, DF
[48], [49]	Hilly Terrain	2.4 GHz	40 MHz	SISO	295 km/h	PL, SF, K
[75]	Tunnel	2.154 GHz	30 MHz	SISO	N/A	PL, DS
[74]	Tunnel	930 MHz	200 kHz	SISO	N/A	PL
[80]	Station	930 MHz	200 kHz	SISO	N/A	PL
[81]	Station	930 MHz	200 kHz	SISO	N/A	PL, K , SF, FD, LCR, AFD
[76]	Various	930 MHz	200 kHz	SISO	350 km/h	PL, PDF, DS, PDP
[77]	Various	930 MHz	200 kHz	SISO	340 km/h	SI
[83], [84]	Various	930 MHz	200 kHz	SISO	340 km/h	SF
[85]	Various	930 MHz	200 kHz	SISO	290 km/h	K , LCR, AFD
[78], [79]	Various	2.1 GHz	3.84 MHz	SISO	240 km/h	PL, K , DS, PDP

SISO: single-input single-output; MISO: multiple-input single-output; SIMO: single-input multiple output; PL: path loss; DS: RMS delay spread; K : Ricean K -factor; PDP: power delay profile; AS: angular spread; AoA: angle of arrival; PAS: power azimuth spectrum; DF: Doppler frequency; SF: shadow fading; FD: fade depth; LCR: level crossing rate; AFD: average fade duration; PDF: probability density function; CDF: cumulative distribution function; FM: fading margin; PSD: power spectrum density; SI: stationarity interval

2.2.1 HST Propagation Scenarios

HST environments can be roughly classified into the following 6 scenarios: open space, viaduct, cutting, hilly terrain, tunnels and stations.

1) In the open space scenario [46], also called plain scenario [44], the Rx is moving at a very high speed in a rural area where the BS antenna is much higher than the surroundings [47]. This environment focuses on large cells and continuous coverage

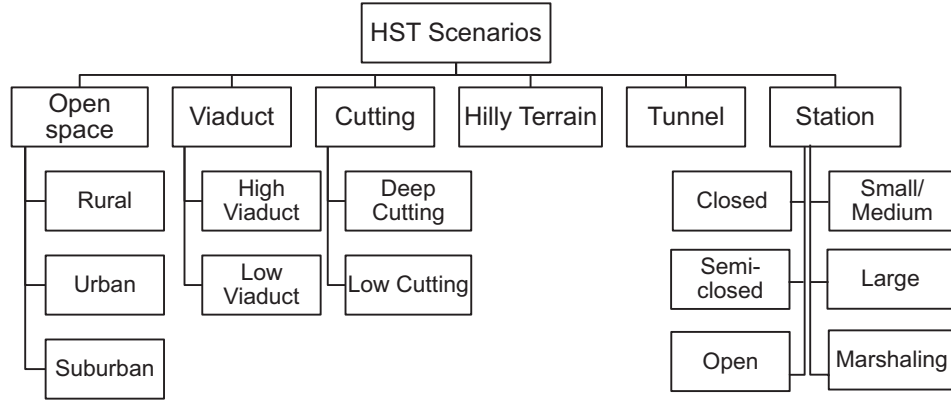


FIGURE 2.1: Classification of HST Scenarios.

where the link between the fixed Tx and moving Rx normally has a dominant line-of-Sight (LoS) component. However, after a certain distance, called breakpoint distance, the impact of the sparse scatterers will be noticed at the Rx represented by Non-Line-of-Sight (NLoS) components. As a result, the breakpoint distance is the point at which the slopes of the PL and Ricean K -factor will be noticeably changed, e.g., dual-slope PL model [86, p. 50]. It has been proved that there is a strong link between the breakpoint distance and the antenna height. For a certain site, as the antenna height decreases, the breakpoint moves closer to the Tx. This is because a bigger Fresnel zone is intercepted by the ground, usually covered by vegetation, when the antenna height is lower. Furthermore, due to the influences of different environments, slight variations in the breakpoint distance can be noticed in different scenarios. Therefore, it can be concluded that the breakpoint distance is mainly determined by the antenna height with slight environmental effects [87]. Based on the geographic nature and the distribution/height of the surrounding scatterers, the open scenarios can be further classified into rural [45], urban, and suburban as illustrated in Fig. 2.1.

2) The viaduct scenario is common for HSTs as they often operate on viaducts [50]–[66]. The main purpose of viaducts is to ensure the smoothness of the rail, high speed of the train, and reduce the reflection, scattering, and diffraction caused by nearby scatterers, e.g., trees and buildings. The viaduct height and relative BS height have great influence on the received signal. Because of the relatively high altitude of the viaduct in comparison with the surrounding terrain, the LoS component is dominant in this scenario. However, the sparsity of the scatterers in the environment

around the viaduct will still influence the received signal at the Rx [53]. Based on the relative altitude between the scatterers and the viaduct, this scenario can be further classified into high viaduct and low viaduct scenarios. In the former, most scatterers located within 50 m from the viaduct are lower than the surface of the viaduct and therefore their impact on the propagation characteristics is negligible. In the low viaduct scenario [66], [67], some of the nearby scatterers are higher than the surface of the viaduct and consequently they introduce rich reflections and scattering components that may result in a severe shadow fading and/or extra PL [36].

3) The cutting scenario is another common scenario for HST wireless communications [68]–[73]. It represents an environment where the HST passes a U-shaped geographical cut surface between the hills. The cutting is widely used for HST construction to ensure the smoothness of the rail and help to achieve a high speed of the train when passing through hills. The propagation of radio waveforms in this scenario is significantly affected by the steep walls on both sides. The LoS component can be observed along the route of the HST in this scenario. Here, we can recognise between two cutting scenarios: deep cutting if the receive antenna mounted on top of the train is lower than the upper eave of the cutting and low cutting if the height of the upper eave is lower than the top of the receive antenna.

4) In the hilly terrain scenario [48], [49], the surrounding environment is densely scattered with objects distributed irregularly and non-uniformly. With high-altitude transmit antennas and low-altitude obstacles, the LoS component is observable and can be detected along the entire railway. However, multipath components scattered/reflected from the surrounding obstacles will cause serious constructive or destructive effects on the received signal and therefore influence the channel's fading characteristics.

5) The tunnel scenario represents an environment where HST passes through tunnels [74], [75] with different lengths ranging from hundreds of meters to several kilometers. The length, size, and shape of the tunnels and the encountered waveguide phenomena have significant impact on the communication channel. Because of the long limited space, bounding of tunnel, and poor smoothness of the interior wall,

propagation characteristics of signals in tunnels are quite different from other scenarios. To overcome the problem of the limited visibility encountered in tunnels and to design an optimal wireless communication network, leaky feeders and DAS were often deployed. However, as HST may require long tunnels, leaky feeder solution are more expensive especially at high operating frequencies and its maintenance is considerable complex [88]. As a result, DAS is more practical [89]. It can provide considerable gain in coverage and capacity, and provide spatial diversity against the fading by using the antenna elements at different locations. It also has advantages in future applications such as higher distance between repeaters, and easy maintenance after being opened, which can meet the continuous and high quality wireless communication of users in the train inside the tunnel. Fig. 2.2 illustrates viaduct, cutting, and tunnel scenarios.

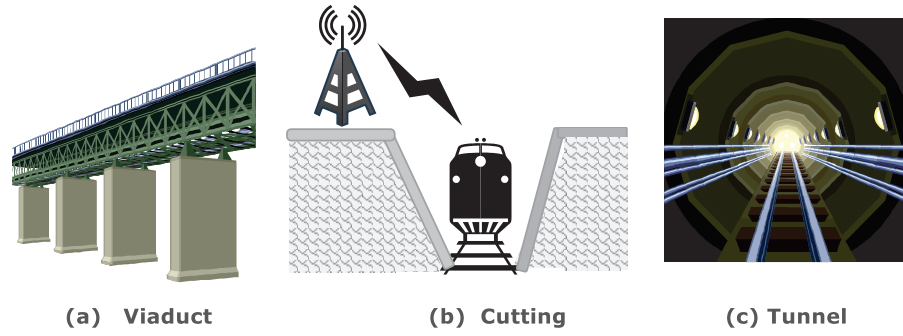


FIGURE 2.2: Three typical HST propagation scenarios: (a) viaduct, (b) cutting, and (c) tunnel.

6) The stations scenario represents the railway facility where HSTs stop regularly to load/unload passengers stations [80], [81]. HST stations can be classified according to their size or architecture. Based on the size of the station, which reflects the estimated communication traffic, station scenario can be categorised into small to medium size stations, large stations, and marshalling stations [36]. From the architecture perspective, that impacts the propagation characteristics inside the station, three HST station scenarios can be recognised, i.e., open station, semi-closed station, and closed station [81] as illustrated in Fig. 2.1.

The aforementioned scenarios are the most encountered ones in HST environment. However, recent measurement campaigns have shed some light on other special HST scenarios such as crossing bridges [82]. Besides the previous “individual” scenarios,

HST may encounter more than one scenario in one wireless communication cell in what so called combination scenarios [36]. Two combination scenarios are reported in the literature. The first one is a combination between tunnel and viaduct where viaducts are usually used as transition between tunnels in mountain environment. The frequent transition between tunnel and viaduct will increase the severity of fading at the transition points causing a drop in the communication quality. The second combination is between cutting scenarios, i.e., deep and low cuttings, and rural scenario. The frequent and fast transition between these scenarios can degrade the quality of the communication link and makes signal prediction quite challenging.

2.2.2 Channel Statistics

Channel statistics are essential for the analysis and design of a communication system. Most of HST measurement campaigns have concentrated on large-scale fading statistics, like PL and shadowing. PL models for HST channels have been reported in [42]–[45], [47], [48], [50], [51], [53]–[56], [59], [60], [63], [68], [69], [71], [72], [74]–[76], [78], [79] and shadowing has generally been modelled as log-normal distributed. Various channel statistics studied in HST channel measurement campaigns are shown in Table 2.1. The Ricean K -factor is a very important parameter in link budget and channel modelling. Therefore, many papers presented the estimation of K -factor in different scenarios, e.g., open space [45], viaduct [50], [52], [59]–[63], cutting [68]–[72], and hilly terrain [48]. In [58], [60], [63], [71], the spatial/temporal variations, e.g., Fade Depth (FD), Level Crossing Rate (LCR), and Average Fade Duration (AFD), were statistically modeled as functions of the structural parameters of the viaduct and cutting scenarios. Doppler behaviour and angular information of HST channels in open space scenario were analysed in [46] while Power Delay Profile (PDP) was investigated in [44], [45], [76], [78], [79]. The stationarity interval, defined as the maximum time duration over which the channel satisfies the Wide Sense Stationary (WSS) condition, of HST channels was investigated in [77] based on measurements. In the future, more channel statistics, especially those related to small-scale fading parameters, are necessary to be investigated in measurements.

2.2.3 Measurement's Setup Parameters

Carrier Frequency and Bandwidth: most of the measurement campaigns in the literature were conducted at the carrier frequency of 930 MHz in GSM-R systems [47], [50]–[52], [54]–[58], [60], [61], [63], [68]–[71], [74], [76], [77]. Correspondingly, all of the aforementioned measurements were for narrowband channels with bandwidth of 200 kHz. Wideband channel measurements with higher bandwidths, i.e., 10–100 MHz, and higher carrier frequencies, i.e., 2.1–5.2 GHz, were reported in [42]–[46], [48], [59], [62], [72], [73], [75], [78], [79].

Antenna Configuration: The majority of HST measurements campaigns so far have focused on Single-Input Single-Output (SISO) systems [42]–[44], [47], [48], [50]–[63], [68]–[79]. MIMO systems, where multiple antennas are equipped at both ends, are essential for providing higher capacity to meet the requirements of future high speed data transmissions. However, only very few measurement campaigns were conducted using multiple antennas at either the Tx, i.e., Single-Input Multiple-Output (SIMO) systems [45], [46], or Rx, i.e., Multiple-Input Single-Output (MISO) systems [46]. Hence, HST MIMO wideband channel measurement campaigns with carrier frequency and bandwidth larger GSM-R ones are needed for future HST communication system developments.

2.3 HST Channel Models

HST channel models in the literature can be categorised as large-scale fading models [34], [43], [44], [48], [51], [54]–[56], [59], [63], [68], [69], [72], i.e., PL and shadowing, and small scale-fading models [15], [33], [34], [90]–[101]. The state-of-the-art of HST channel models has not been investigated yet. Therefore, we will first categorise PL models in Table 2.2. In Table 2.3, the important HST small-scale fading channel models are briefly reviewed and classified according to the modelling approach, scenario, stationarity, antenna configuration, Frequency Selectivity (FS), scatterer region, and cellular architecture.

TABLE 2.2: PL and shadow fading models for HST channels.

Ref.	Scenario	PL exponent (n)	Intercept (A)	SF std (dB)	Notes
[43]	Indoor	2.16 1.8	49.8 39.9	2.8 2.3	Using planner antenna at Tx Using omni-directional antenna at Tx
[34]	RMa	2.15 4	44.2 10.5 - 18.5 $\log_{10}(\frac{h_{BS}}{h_{MS}})$	4 6	$30m < d < d_{BP}$ $d_{BP} < d < 10km$
[51]	Viaduct	3.665 4.326	71.83	N/A	Open viaduct Non-open viaduct
[54]	Viaduct	$0.000194h_{BS} + \frac{42.84}{h_{BS}} + 0.705$	85.5	2.1–3.1	n value is related to h_{BS}
[55]	Viaduct	-0.0012308 d_0 +3.94 -0.0037949 d_0 +6.4333 -0.00044615 d_0 +3.596	$20\log_{10}(\frac{4\pi d_0}{\lambda})$	2.1–3.1	$200 \leq d_0 \leq 900$ $d_0 > 900$, High Viaduct: $h_v > 25m$ $d_0 > 900$, Low Viaduct: $h_v < 25m$
[56]	Viaduct	$0.000194h_{BS} + \frac{42.84}{h_{BS}} + 0.04798H_{BS}$	85.5	2.1–3.1	n is related to h_{BS} and H_{BS}
[59]	Viaduct	3.03	12.4	2	
[63]	Viaduct	-0.043 h_v +0.236 -0.02 h_v +1.65	$0.61h_v+91.75$ 54.95	4.93 2.47	$d \leq d_{BP}$ $d > d_{BP}$
[68]	Cutting	4.3	71.83	3.5	
[69]	Cutting	$13.05 e^{-0.039(w_{down}-w_{up})}$ $1.66w_{down}^2 - 58.51w_{down} + 517.6$	85.5	4 3	Deep cutting Low cutting
[48]	Hilly Terrain	2.4 3.88	31.31 -11.6	3.3 4.2	$d < d_{BP}$ $d \geq d_{BP}$
d_{BP} : breakpoint distance, h_{BS} : BS antenna height, h_{MS} : MS antenna height, H_{BS} : BS effective antenna height, d_0 : reference distance, λ : wavelength, h_v : viaduct height, w_{down} and w_{up} : cutting dimensions					

TABLE 2.3: Important HST small-scale fading channel models.

Ref.	Channel Model	Scenario	NS	Antenna	FS	SR	CA
[15]	Non-fading	Open space	No	MIMO	NB	N/A	Conventional
[90]	GBDM	Open space	Yes	MIMO	WB	Non-isotropic	Conventional
[91]	GBDM	Open space	Yes	MISO	WB	Non-isotropic	Conventional
[102]	GBDM	Various	Yes	SISO	NB	Non-isotropic	Conventional
[92], [93]	GBDM	Tunnel	Yes	SISO	NB	Non-isotropic	Conventional
[94]	RS-GBSM	Open space	No	MIMO	NB	Non-isotropic	Conventional
[95]	RS-GBSM	Open space	No	MIMO	WB	Isotropic	Conventional
[33], [34]	IS-GBSM	Open space	No	MIMO	WB	Non-isotropic	Mobile Relay
[94], [103]	IS-GBSM	Cutting	No	MIMO	NB	Isotropic	Conventional
[99], [100]	NGSM	Open space	Yes	MIMO	WB	Non-isotropic	Conventional
[101]	NGSM	Viaduct	Yes	MIMO	WB	Non-isotropic	Mobile Relay

NS: Non-stationarity, SR: Scatterer Region, CA: Cellular architecture

2.3.1 Large-Scale Fading Models

PL estimation is essential for wireless link budget computation and wireless network planning. PL and shadow fading channel models for various HST scenarios have been developed based on measurement results conducted in the open literature. These PL models are typically expressed as

$$PL(d) = A + 10n \log_{10}(d), \quad (2.1)$$

where d is the distance between the Tx and Rx in unit of meters (m), n is the PL exponent and A is the intercept. Note that SF follows log-normal distributions with the standard deviation for each model is given in Table 2.2.

2.3.2 Cellular Architectures and Scenarios

As mentioned in Chapter 1, adopting conventional cellular architecture in HST wireless communication systems may lead to several problems in terms of providing reliable and fast communication to HST passengers. Therefore, other cellular architectures, such as DAS, CoMP, and MRS need to be considered. In the literature, most of the proposed channel models have considered the conventional architecture where fixed BSs are installed on the track-side to provide wireless coverage to HST passengers inside carriages [15], [90]–[95], [99]. By considering MRS solution, we will have two channels, outdoor channel between the BS and the MRS and an indoor one between MRS and train passengers. As a result, we will have two channels: an outdoor channel

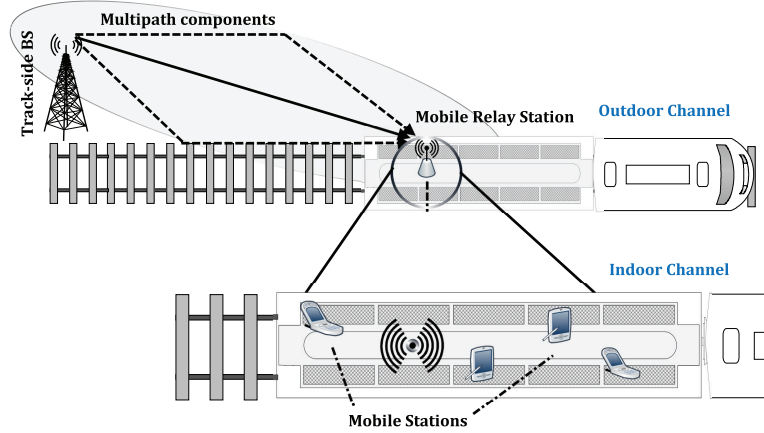


FIGURE 2.3: A HST communication system deploying MRSs.

between the BS and MRS, and an indoor one between the MRS and an MS of a train passenger as illustrated in Fig. 2.3. The properties of radio channels in the carriages resemble indoor environment and hence they can be modelled using existing indoor channel models [43]. Therefore, [33], [34], [101] have focused on modelling the outdoor channel because of the challenges that this channel faces due to the high velocity of the Rx.

HST scenarios have been presented in details earlier in this chapter. While most of these scenarios can only be encountered in railway environments, open space scenario is similar to the rural or urban scenarios that can be found in conventional Vehicle-to-Infrastructure (V2I) or Vehicle-to-Vehicle (V2V) communication systems. Therefore, most of the current HST channel models, developed from V2I and V2V channel models by taking into account the effect of the high velocity of the Rx on the channel parameters, have been proposed for open space scenario [15], [33], [34], [90], [91], [95], [99]. Channel models for tunnel, cutting, and viaduct scenarios were studied in [93], [94], and [101], respectively.

In summary, more HST channel models that consider other cellular architectures, such as DAS, are needed in the future. In addition, more HST scenarios should be considered in proposing future HST channel models.

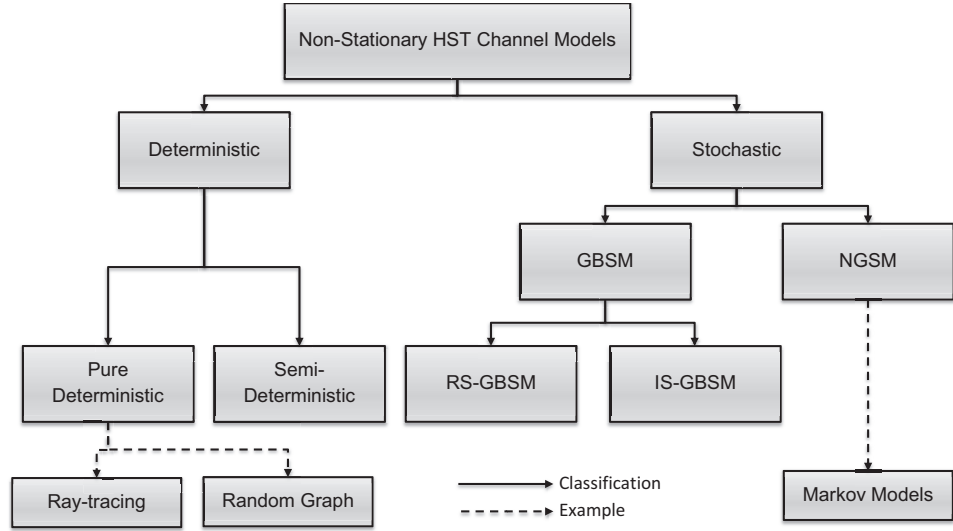


FIGURE 2.4: Classification of non-stationary HST channel models

2.3.3 Modelling Approaches of HST Small-Scale Fading Models

In terms of modelling approach, the current HST channel models in the literature, presented in Table 2.1, can be classified as deterministic [90]–[93], [102] and stochastic channel models. The latter can be further classified into GBSM [33], [34], [94], [95] and Non-Geometrical Stochastic Model (NGSM) [99], [101] as illustrated in Fig. 2.4.

2.3.3.1 Deterministic channel models

Deterministic channel models are usually based on the detailed description of specific propagation environment and antenna configuration. The amplitudes, phases and delays of the propagated waves are obtained using intensive simulations that incorporate details of propagation environments like, roads, building, trees, houses, ...etc. Therefore, deterministic models are physically meaningful and potentially accurate. This category can be further classified into the Geometry-Based Deterministic Model (GBDM) and the Finite-Difference Time-Domain (FDTD) model. GBDMs based on ray-tracing method were proposed in [91]–[93], [102] to model HST propagation channels in different HST scenarios. In [93], a 3D ray-tracing approach for wave propagation modelling in HST tunnels was presented. The proposed model resulted in

a complex channel impulse response that incorporates channel information, e.g., the wave-guide effect observed in tunnels and the impact of another train passing in the opposite direction on the Doppler shift and time delay. Authors of [102] implemented similar approach to model HST channels in various scenarios. Both of [93] and [102] have used measurement results to verify the proposed channel models. Another HST channel model based on 3D ray-tracing approach has been implemented in [91] to analyse the channel characteristic, e.g., the frequency-selectivity and time-variance (Doppler spread). The objects, e.g., trees, buildings, or barriers, on both sides of the railway track were modeled using rectangular boxes with scattering wave propagation characteristics where the dimensions of the boxes are statistically generated. Since the propagation characteristics of Electro-Magnetic (EM) waves in tunnels are significantly different from those in other HST environments, a multi-mode waveguide channel model is proposed in [104]. The proposed model, which is a hybrid model that combines the geometrical optical model and waveguide model, can characterise the wave propagation both in near and far regions of the source. However, the aforementioned model failed to discuss the Far Line-of-Sight (FLoS) phenomena observed inside tunnels [105] or provide a mechanism to determine the breakpoint for different propagation regions in tunnels [7]. A GBDM based on random propagation-graph was proposed in [90] to characterise time-variant HST channels in open space scenario. Similar to ray-tracing method, propagation-graph can predict channel impulse responses by thorough searching for propagation paths that connect Tx and Rx. This modelling approach can be performed by considering the geometry of the simulated environments, e.g., the distribution, mobility, and visibility of the scatterers. Despite their high accuracy, GBDMs require detailed descriptions of the propagation environments and extensive computational resources to be implemented. To avoid the high complexity of implementing GBDMs while maintaining sufficient accuracy, semi-deterministic models for viaduct and cutting scenarios of HST were proposed in [106]. However, the proposed models have only considered large-scale fading, i.e., PL and SF, and neglected the effect of small-scale fading parameters on the received signal.

2.3.3.2 GBSMs

In GBSMs, the impulse responses of HST channels are characterised by the law of wave propagation applied to specific Tx, Rx, and scatterer geometries which are predefined in a stochastic fashion according to certain probability distributions. Different types of GBSMs differ mainly in the proposed scatterer distributions. Based on the position of the effective scatterers, GBSM can be further classified into Regular-Shaped Geometry-Based Stochastic Model (RS-GBSM) such as one-ring [95], two-ring, and ellipses, and Irregular-Shaped Geometry-Based Stochastic Model (IS-GBSM) [33], [34], [94].

RS-GBSMs assume that all the effective scatterers are placed on regular shapes, and therefore different RS-GBSMs have different shapes of scatterer distributions, e.g., one-ring, two-ring, and ellipses for Two-Dimensional (2D) models and one sphere, two-spheres, elliptic-cylinders for 3D ones. RS-GBSMs often result in closed-form solutions or at least mathematically tractable formulas. In [95], a one-ring RS-GBSM was proposed to model HST channel in open space scenario. The scatterers are assumed to be distributed on a ring around the MS where different PDF of the scatterers were analysed. Considering the narrowband GSM-R for HST communication system, a 3D one-sphere RS-GBSM was proposed in [94] for open space scenario. The proposed model used Von Mises distribution to describe the azimuth angles and the ST CF was derived. However, both of the aforementioned models have assumed that the HST channel satisfies the WSS condition that has been proved incorrect by measurements [46].

IS-GBSMs place the effective scatterers with predefined properties at random locations with certain statistical distributions usually obtained/approximated from measurements [107]. Unlike RS-GBSMs, the random locations of the scatterers do not form regular shapes. IS-GBSMs for HST channels have been introduced in the RMa scenario in WINNER II [34] and moving networks scenario in IMT-A channel models [33] with the train speed can be up to 350 km/h and the MRS technology is employed. In [94], IS-GBSM has been proposed for HST channel in cutting scenario assuming the scatterers to be uniformly distributed on the surface of the two slopes of the cutting.

However, the aforementioned channel models have neglected the non-stationarity of HST channels and assumed that the WSS assumption can still be applied.

2.3.3.3 NGSMs

NGSMs characterise physical parameters of a HST propagation channel in a completely stochastic manner by providing their underlying probability distribution functions without assuming an underlying geometry. An NGSM based on finite-state Markov chains for HST wireless communication channels was proposed in [99]. The proposed model is able to capture the characteristics of time-varying HST wireless channel by using Markov chain to track the channel state variation at different received Signal-to-Noise Ratio (SNR) intervals. However, the model has not been verified by using real-field measurements and thus deserves more investigation. Authors of [101] have followed similar approach to model the dynamic evolution of multi-path components, i.e., birth-death process, using four-state Markov chain model. The transition matrix of the birth-death process was calculated based on the measurement presented in [59].

2.4 Research Gaps in HST Channel Measurements and Models

2.4.1 Non-Stationarity of HST Channels

Measurements in the literature have demonstrated that HST channels are non-stationary since the stationary conditions, measured by stationary interval, retain to a very short period of time in comparison with other types of channels, e.g., V2I and V2V channels [77]. This is mainly caused by the very high speed of the trains and the encountered changes in surrounding areas. Although the non-stationarity of HST channels has been implicitly considered in GBDMs [90], [91], [93], [102], but these models are mainly site-specific and cannot be easily generalised to a variety of scenarios. The

non-stationarity feature of HST channels has been considered in NGSM proposed in [99] by implementing the birth-death process to simulate the appearance and disappearance of the scatterers. However, verifying the proposed models by real-field measurements was not performed and therefore more comprehensive investigations are required to validate the accuracy of those models. Non-stationary channel models should consider several time-variant model parameters, such as angular parameters, Doppler frequency, Ricean K -factor and the distance between Tx and Rx.

2.4.2 Statistical Properties of HST Channels

Investigating the statistical properties of HST channels is essential for understanding and analysing the HST communication system. In Table 2.1, several channel statistics obtained from measurements were presented. However, most of proposed HST channel models in the literature have failed to provide the corresponding theoretical analysis. It is highly desirable to investigate different statistical properties of HST channel models, such as the ST CF, the ACF, the space CCF, the PSD, the LSF, the LCR, and the AFD.

2.4.3 HST Scenarios

HST scenarios were classified and thoroughly explained in Section 2.2. During its travel and due to its high velocity, HST runs across diverse scenarios so rapidly that a single model is incapable of capturing accurately the variations of HST channels. While most standard channel models did not consider any of the HST scenarios, IMT-A channel model, WINNER II channel model, and most of the non-standard HST channel models were proposed for open space scenario only. Therefore, it is essential that new HST channel models consider other scenarios and preferably take into account the impact of diverse scenarios on HST channels.

2.4.4 3D HST Channel Models

Apart from the GBDMs that use 3D ray-tracing tool to model HST channels [91]–[93], [102], HST channels were generally proposed and measured assuming that propagation waves are travelling in two dimensions and therefore ignore the impact of the elevation angle on channel statistics. Thus, 3D channel measurements and models are necessary, especially when the HST is close to the BS where considering elevation angles can demonstrate the impact of the waves reflected from ground on the received signal.

2.5 Summary

This chapter has provided a survey of HST channels, that represent high-mobility V2I channels, in terms of conducted measurements and proposed channel models. We have classified HST channel measurements based on the scenarios, carrier frequencies, bandwidths, measured channels, antenna configurations, train speeds, and channel statistics. We have also presented various HST large-scale fading channel models in the literature. Then, we have classified HST small-scale fading channel models based on their modelling approaches, scenarios, stationarity, FS, and cellular architecture. Finally, we have highlighted some research gaps in HST channel measurements and modelling.

Chapter 3

Characterisation of Non-Stationary MIMO Channels

3.1 Introduction

In wireless communication systems, the assumption of time-invariant, or strictly stationary, channels has become unrealistic since the Tx, the Rx, or the scatterers can be in motion. To characterise linear time-variant channels, Bello has proposed his famous framework of system functions in terms of time, frequency, delay, and Doppler in [108]. However, the proposed system functions can only characterise non-directional channels. For direction channels, Bello's system functions were extended in terms of direction and space in [109], [110]. Bello has also introduced the assumption of Wide Sense Stationary Uncorrelated Scattering (WSSUS) that has been commonly used since. In time domain, the WSS assumption means that the statistical properties of the mobile radio channels do not change over a short time interval [111, p. 110]. The Uncorrelated Scattering (US) assumption is defined, in time domain, as contributions with different delays are uncorrelated. The WSSUS channels combines both the WSS assumption in terms of time and the US assumption in terms of delay [112, p. 109] in the time domain. In HST communication systems, in which the train is moving in high speeds that can easily exceed 250 km/h, the WSS assumption is violated [7].

Establishing a theoretical framework that explains in details the characterisation of non-stationary mobile fading channels is essential for understanding and modelling them properly. Therefore, we will briefly review the characterisation of non-stationary channels and further extend the work presented in the literature. The rest of the chapter is organised as follows. In Section 3.2, we explain the system functions that describe non-WSSUS mobile radio channels, and then the CFs will be derived in Section 3.3. By considering the assumption of US and antenna stationarity, the system functions and the CFs of non-stationary systems and the relationship between them will be presented in Section 3.3. Finally, the conclusions are drawn in Section 3.4.

3.2 System Functions of Non-WSSUS Channels

In this section, we will derive the system functions and CFs that describe non-WSSUS wideband MIMO channels. The received signal experiencing non-WSSUS wideband mobile channels can be defined as a 3D stochastic process in terms of time t , delay τ , and space x , which denotes the location of an antenna element in the antenna array in the Tx/Rx [109]. It can be described by the space-time-variant channel impulse response $h(t, \tau, x)$ [109], [113]. Other 3D system functions can be obtained by using Fourier transforms as Fig. 3.1 illustrates.

The eight system functions in Fig. 3.1 are the

- Space-time-variant channel impulse response, $h(t, \tau, x)$
- Space-variant Doppler-spread impulse response, $S_H(\nu, \tau, x)$
- Space-time-variant transfer function, $L_H(t, f, x)$
- Space-variant Doppler-spread transfer function, $H(f, \nu, x)$
- Time-variant direction-spread impulse response, $W(t, \tau, \Omega)$
- Direction-Dopplerspread impulse response (spread function), $X(\nu, \tau, \Omega)$
- Time-variant direction-spread transfer function, $Y(t, f, \Omega)$

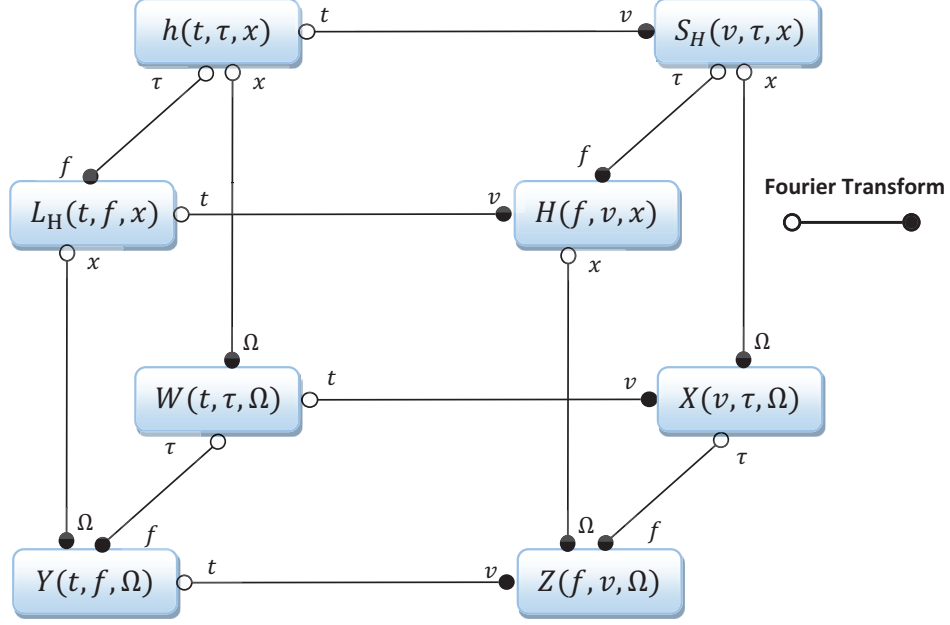


FIGURE 3.1: Relationship of system functions for non-WSSUS channels

- Direction-Doppler-spread transfer function, $Z(f, \nu, \Omega)$

where ν is the Doppler frequency, f is the frequency, and Ω is the direction of an antenna element in the antenna array in the Tx/Rx.

3.3 Correlation Functions of Non-WSSUS Channels

Based on the introduced 3D system functions, the six-Dimensional (6D) CFs of non-WSSUS channels can be obtained as

$$R_h(t, \tau, x; \Delta t, \Delta \tau, \Delta x) = E \{ h(t, \tau, x) h^*(t - \Delta t, \tau - \Delta \tau, x - \Delta x) \} \quad (3.1a)$$

$$R_S(\nu, \tau, x; \Delta \nu, \Delta \tau, \Delta x) = E \{ S_H(\nu, \tau, x) S_H^*(\nu - \Delta \nu, \tau - \Delta \tau, x - \Delta x) \} \quad (3.1b)$$

$$R_L(t, f, x; \Delta t, \Delta f, \Delta x) = E \{ L_H(t, f, x) L_H^*(t - \Delta t, f - \Delta f, x - \Delta x) \} \quad (3.1c)$$

$$R_H(f, \nu, x; \Delta f, \Delta \nu, \Delta x) = E \{ H(f, \nu, x) H^*(f - \Delta f, \nu - \Delta \nu, x - \Delta x) \} \quad (3.1d)$$

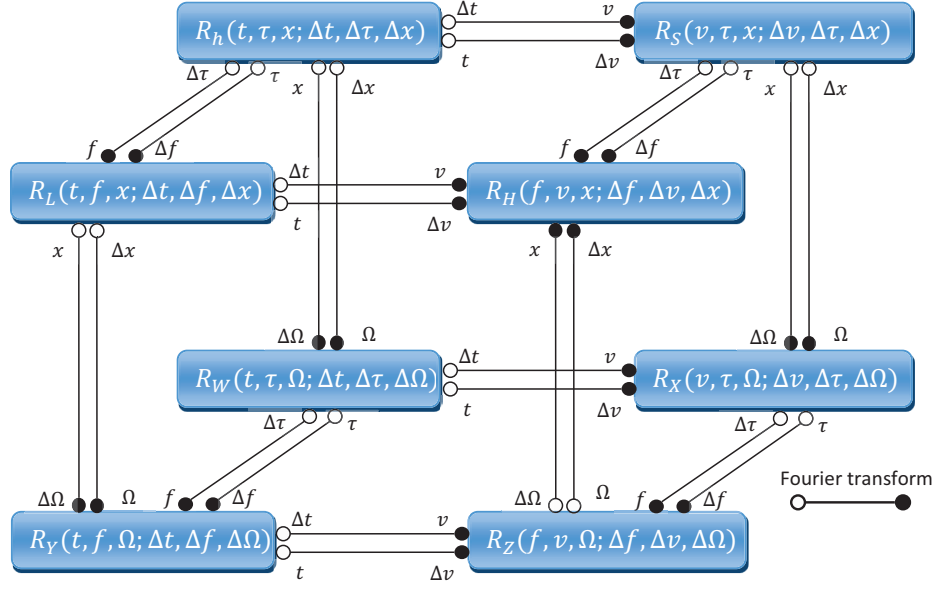


FIGURE 3.2: Relationship of CFs for non-WSSUS channels

$$R_W(t, \tau, \Omega; \Delta t, \Delta \tau, \Delta \Omega) = \mathbb{E} \{W(t, \tau, \Omega) W^*(t - \Delta t, \tau - \Delta \tau, \Omega - \Delta \Omega)\} \quad (3.1e)$$

$$R_X(v, \tau, x; \Delta v, \Delta \tau, \Delta x) = \mathbb{E} \{X(v, \tau, x) X^*(v - \Delta v, \tau - \Delta \tau, x - \Delta x)\} \quad (3.1f)$$

$$R_Y(t, f, \Omega; \Delta t, \Delta f, \Delta \Omega) = \mathbb{E} \{Y(t, f, \Omega) Y^*(t - \Delta t, f - \Delta f, \Omega - \Delta \Omega)\} \quad (3.1g)$$

$$R_Z(f, v, \Omega; \Delta f, \Delta v, \Delta \Omega) = \mathbb{E} \{Z(f, v, \Omega) Z^*(f - \Delta f, v - \Delta v, \Omega - \Delta \Omega)\} \quad (3.1h)$$

where Δt is the time lag (i.e., time difference), $\Delta \tau$ is the delay lag, Δf is the frequency lag, Δv is the Doppler lag, Δx is the space lag (i.e., antenna element spacing [109]), and $\Delta \Omega$ is the direction lag. Here, $(\cdot)^*$ denotes the complex conjugate operation and $\mathbb{E} \{\cdot\}$ designates the statistical expectation operator. The Fourier transform relationships between the eight CFs in (3.1a)–(3.1h) are illustrated in Fig. 3.2.

The 6D CFs (3.1a)–(3.1h) are spatial-direction extension of the four-Dimensional (4D) CFs proposed by Matz [114]. Matz suggested another channel statistic for non-WSSUS channels, namely, the LSF $C_H(t, f, \tau, \nu)$, which describes the mean power of the effective scatterers causing delay-Doppler shifts (τ, ν) at time t and frequency f [115]. Here, we extend the 4D LSF in [115] to the space and direction domains

resulting in the 6D LSF $C_H(t, f, x, \tau, \nu, \Omega)$, which can be obtained as follows

$$C_H(t, f, x, \tau, \nu, \Omega) = \iiint R_h(t, \tau, x; \Delta t, \Delta \tau, \Delta x) e^{-j2\pi(\nu \Delta t + f \Delta \tau + \Omega \Delta x)} d\Delta t d\Delta \tau d\Delta x \quad (3.2a)$$

$$= \iiint R_S(\nu, \tau, x; \Delta \nu, \Delta \tau, \Delta x) e^{j2\pi(t \Delta \nu - f \Delta \tau - \Omega \Delta x)} d\Delta \tau d\Delta \nu d\Delta x \quad (3.2b)$$

$$= \iiint R_L(t, f, x; \Delta t, \Delta f, \Delta x) e^{-j2\pi(\nu \Delta t - \tau \Delta f + \Omega \Delta x)} d\Delta t d\Delta f d\Delta x \quad (3.2c)$$

$$= \iiint R_H(f, \nu, x; \Delta f, \Delta \nu, \Delta x) e^{-j2\pi(\tau \Delta f + t \Delta \nu + \Omega \Delta x)} d\Delta f d\Delta \nu d\Delta x \quad (3.2d)$$

Matz also proposed the channel CF $A_H(\Delta t, \Delta f, \Delta x, \Delta \tau, \Delta \nu, \Delta \Omega)$ that can characterise the correlation of multipath components separated by Δt in time, by Δf in frequency, by $\Delta \tau$ in delay, and by $\Delta \nu$ in Doppler. Here, we will extend the 4D channel CF in [115] by further considering the multipath components separated by Δx in space and by $\Delta \Omega$ in direction. The resulting 6D channel CF can be expressed as

$$A_H(\Delta t, \Delta f, \Delta x, \Delta \tau, \Delta \nu, \Delta \Omega) = \iiint R_h(t, \tau, x; \Delta t, \Delta \tau, \Delta x) e^{-j2\pi(t \Delta \nu + \tau \Delta f + x \Delta \Omega)} dt d\tau dx \quad (3.3a)$$

$$= \iiint R_S(\nu, \tau, x; \Delta \nu, \Delta \tau, \Delta x) e^{j2\pi(\nu \Delta t - \tau \Delta f - x \Delta \Omega)} d\tau d\nu dx \quad (3.3b)$$

$$= \iiint R_L(t, f, x; \Delta t, \Delta f, \Delta x) e^{-j2\pi(t \Delta \nu - f \Delta \tau + x \Delta \Omega)} dt df dx \quad (3.3c)$$

$$= \iiint R_H(f, \nu, x; \Delta f, \Delta \nu, \Delta x) e^{-j2\pi(f \Delta \tau + \nu \Delta t + x \Delta \Omega)} df d\nu dx \quad (3.3d)$$

Figs. 3.3 and 3.4 show the Fourier transform relationship between the 6D CF and the LSF and the channel CF, respectively.

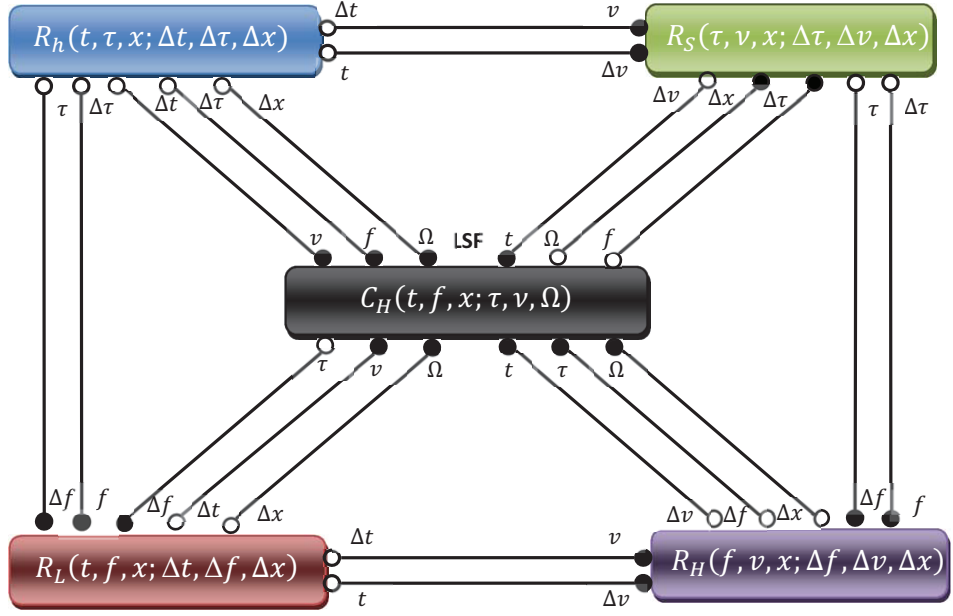


FIGURE 3.3: Relationship of 6D CFs and LSF for non-WSSUS channels

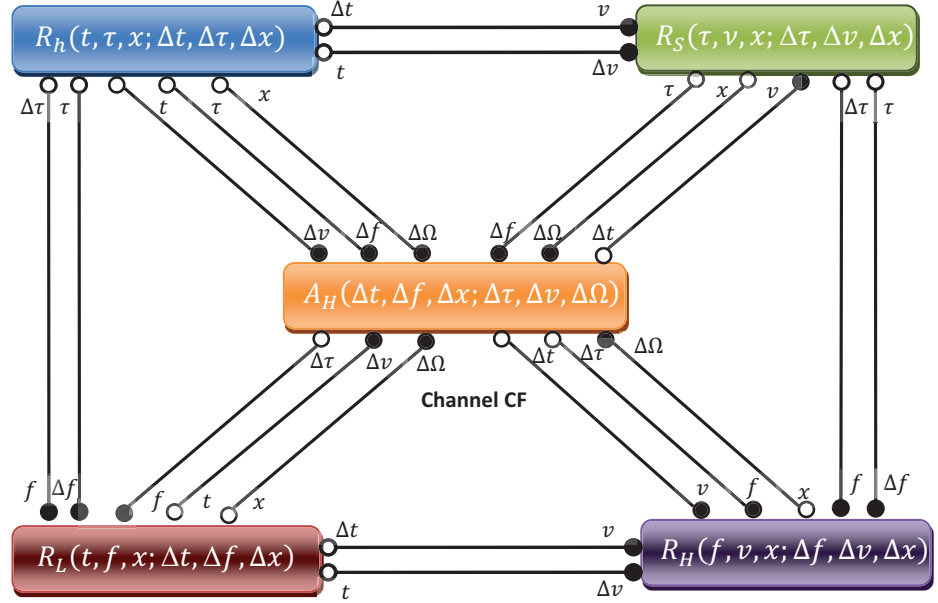


FIGURE 3.4: Relationship of 6D CFs and channel CF for non-WSSUS channels

3.4 System Functions and Correlation Functions of Non-Stationary MIMO Channels

The aforementioned general system functions and CFs of non-WSSUS channel models can be simplified by applying the following assumptions.

- *Uncorrelated scattering (US)*: US means that different channel taps with different delays are uncorrelated. In [108], Bello showed that US channels are WSS in the frequency domain. Therefore, the 6D space-time-frequency-variant space-time-frequency CF in (3.1c) will no longer depend on frequency f , i.e., it will be reduced to the five-Dimensional (5D) space-time-variant space-time-frequency CF $R_L(t, x; \Delta t, \Delta f, \Delta x)$. It follows that the 6D space-time-delay-variant space-time-delay CF in (3.1a) will be reduced to the 5D space-time-delay-variant space-time CF $R_h(t, \tau, x; \Delta t, \Delta x)$.
- *Antenna stationarity*: Antenna stationarity means that the time, frequency, and antenna statistics, i.e., the correlation between different antenna elements separated by Δx , do not depend on the selected transmit or receive antennas [116]. It follows that the 6D space-time-frequency-variant space-time-frequency CF in (3.1c) will no longer depend on space x , i.e., it will be reduced to the 5D time-frequency-variant space-time-frequency CF $R_L(t, f; \Delta t, \Delta f, \Delta x)$. Also the 6D space-time-delay-variant space-time-delay CF in (3.1a) will be reduced to the 5D time-delay-variant space-time-delay CF $R_h(t, \tau; \Delta t, \Delta \tau, \Delta x)$.

In the following chapters, we assume that the HST channel satisfies both the US and antenna stationarity conditions. Antenna stationarity assumption is common for conventional MIMO channels using limited numbers of Uniform Linear Array (ULA) antenna elements. However, this assumption becomes invalid in case of non-ULA antennas [116] and/or massive MIMO channels with a large number (tens or even hundreds) of antenna elements [117]. By applying these two assumptions, the CFs will not depend on f , $\Delta \tau$, and x . Therefore, the 6D CFs in (3.1a)–(3.1h) will be reduced to 4D ones, e.g., the space-time-delay-variant space-time-delay CF in (3.1a) will be reduced to the time-delay-variant space-time CF $R_h(t, \tau, \Delta t, \Delta x)$, and the space-time-frequency-variant space-time-frequency CF in (3.1c) will be reduced to

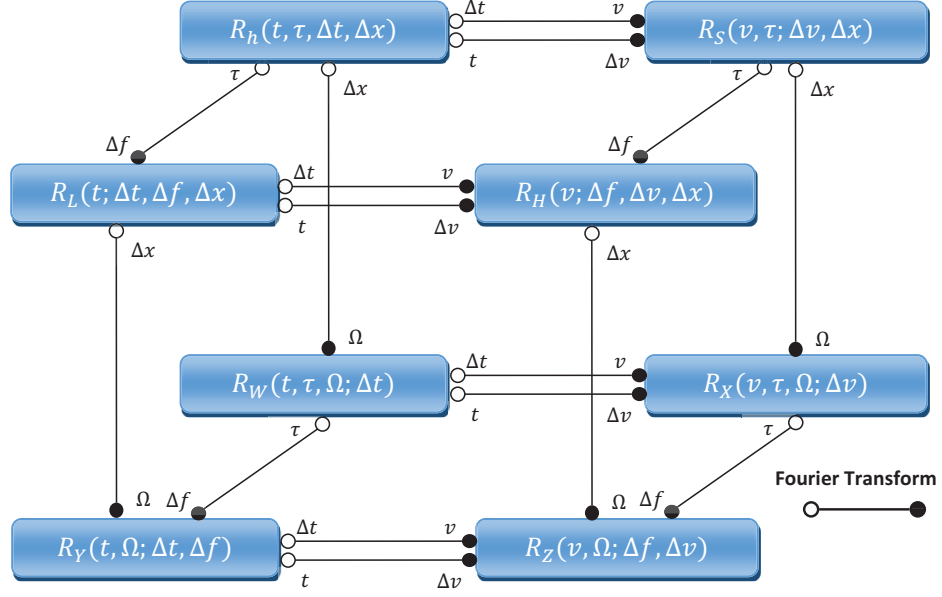


FIGURE 3.5: Relationship of CFs for non-stationary channels

the 4D time-variant space-time-frequency CF $R_L(t; \Delta t, \Delta f, \Delta x)$. Fig. 3.5 shows the relationship between the 4D CFs.

The time-delay-variant space CCF $\rho(t, \tau; \Delta x)$ and time-delay-variant ACF $r(t, \tau; \Delta t)$ can be obtained by imposing $\Delta t=0$ and $\Delta x=0$, respectively, in from $R_h(t, \tau, \Delta t, \Delta x)$. We can also derive the time-delay variant SD PSD $W(t, \tau, \nu, \Delta x)$ by applying the Fourier transform to $R_h(t, \tau, \Delta t, \Delta x)$ in terms of Δt . The relationship between some of the CFs and the LSF of non-stationary channel models that satisfy the US and antenna stationarity conditions is illustrated in Fig. 3.6, which serves as a fundamental framework for the following chapters.

By applying the WSS and US assumptions simultaneously, the CFs will not depend on t and the 4D CFs will be further reduced to 3D ones [109] as illustrated in Fig. 3.7.

Finally, the spatial extension introduced in this chapter should not be confused with the one presented in [118] where the spatial dimension is related directly to the receiver position.

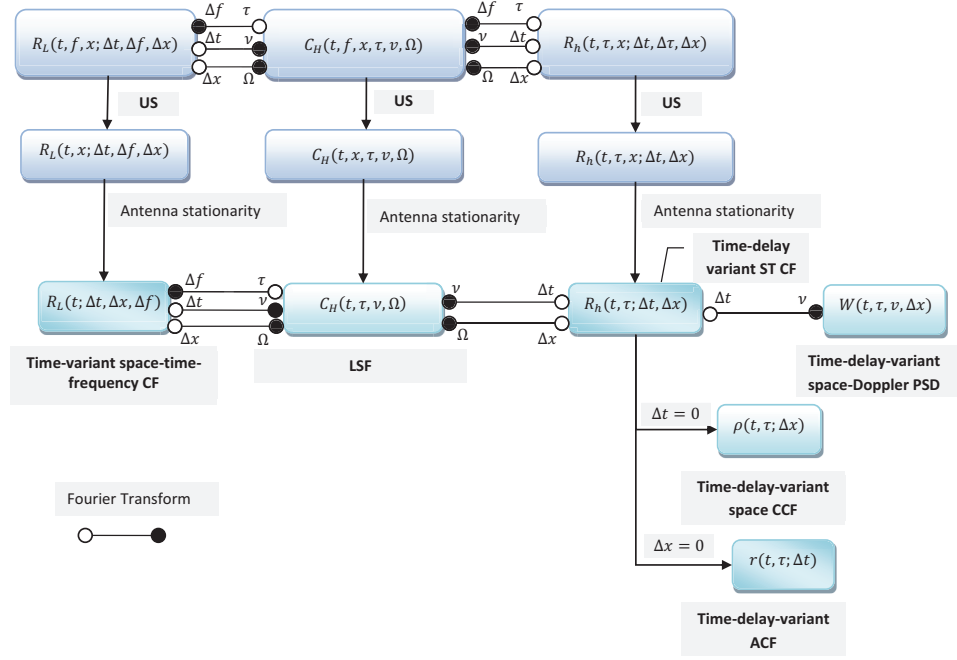


FIGURE 3.6: Characterisation of non-stationary channels

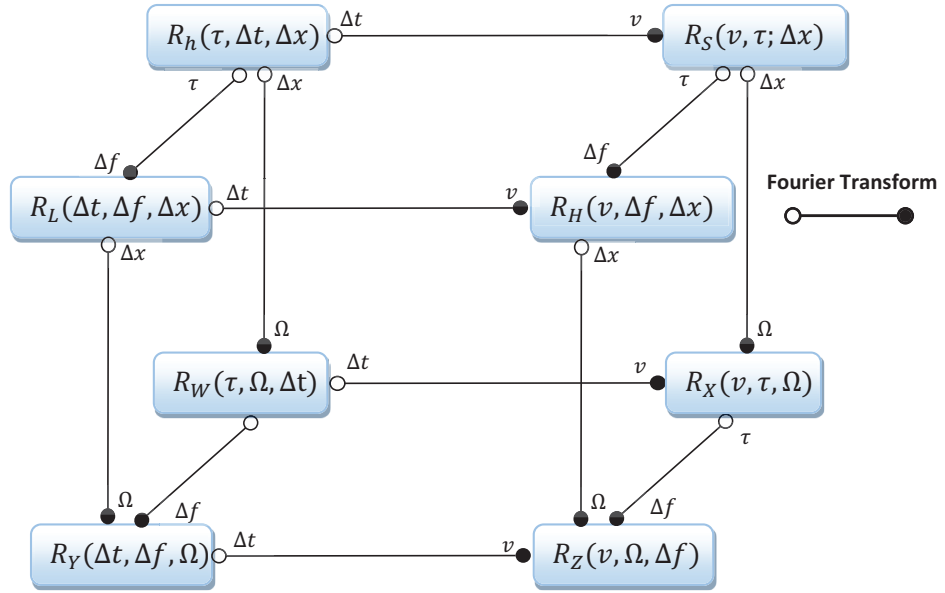


FIGURE 3.7: Relationship for CFs for WSSUS channel models

3.5 Summary

In this chapter, a theoretical framework that explains in details the characterisation of non-stationary mobile fading channels is established. The proposed framework introduces important system functions and CFs of non-stationary channel and illustrate the relation between these functions. This framework will be used as a guideline to derive the statistical properties of the non-stationary HST channel models proposed in the following chapters.

Chapter 4

A Generic 2D Non-Stationary Wideband MIMO Channel Model for Different High-Speed Train Scenarios

4.1 Introduction

Intelligent Transportation Systems (ITS) considers all types of communications between vehicles, i.e., V2V, Vehicle-to-Roadside (V2R) or V2I, and information and communication technologies for rail, water, and air transport [119]. As a fast and convenient ITS, railways that operate trains with a high speed of more than 250 km/h have attracted more and more attentions recently. With the increase of train speeds, wireless communication systems face various challenges such as fast handover [26], and large Doppler spread.

In this chapter, we will consider using the promising MRS technology that has been adopted by IMT-A [33] and WINNER II [34] systems. This is performed by deploying dedicated MRSs on the surface of the train to extend the coverage of the outdoor BS into train carriages. As a result, the effect of frequent handover will be significantly reduced by performing a group handover with the MRS instead of dealing with the individual handover of each passenger [24]. By considering MRS solution, we will

have two channels: an outdoor channel between the BS and MRS and an indoor one between the MRS and MS. Radio channels between the MRS and MSs in the carriages resemble indoor environments and hence can be possibly modelled using the existing indoor channel models [43]. Here, we will focus on the outdoor channel because of the research challenges due to the high velocity of the MRS.

Demonstrating the feasibility of wireless systems in HST scenarios before implementation is not possible without accurate channel models that are able to mimic key characteristics of HST wireless channels, such as the non-stationarity. Similar to V2V channels [22], [120]–[123], the non-stationarity of the HST channels means that the channel statistics can change rapidly over a short period of time. Several measurement campaigns [45], [46], [56], [59], [78] for different HST environments (open space, tunnels, viaducts, hilly terrains, and U-shaped) were conducted but they mainly focused on large-scale fading parameters, such as path loss and delay spread, and thus ignored small-scale fading parameters.

The propagation characteristics change significantly with the change of environments and the distance between the Tx and Rx even in the same terrain. Moreover, the features of HST channels, e.g., non-stationarity and large Doppler shift, significantly differ from those of low-mobility mobile cellular communication channels. Accurate channel models that are able to mimic key characteristics of wireless channels play an important role in designing and testing HST communication systems. Channel models in the literature have failed to demonstrate different propagation parameters of wireless channels in HST scenarios. Adopting a conventional cellular architecture, the LTE-A system [15] provided a relatively simple single-path channel model that supports two scenarios, i.e., open space and tunnels, but ignores the non-stationarity of HST channels. In [91], the propagation channels between HSTs and fixed BSs were modelled using the ray-tracing method, which incorporates a detailed simulation of the actual physical wave propagation process based on an approximation to Maxwell equations [124]. However, the implementation of ray-tracing models always requires extensive computational resources. WINNER II [34] and IMT-A channel models [33] adopted the open space HST scenario in which the MRS technology is employed.

Both channel models introduced time evolution concept to explicitly simulate the non-stationarity of channels. However, it has been demonstrated in [77] how the stationary interval, defined as the maximum time duration over which the channel satisfies the WSS condition, of these two standard channel models is considerably longer than that of real HST channels. For a train speed of 324 km/h, the reported stationary intervals of the standardised models and the measured HST channel were 37.8 ms and 20 ms, respectively [77]. Consequently, the stationary distance of the standardised channel models is equal to 3.4 m, while it is only 1.8 m for the measured HST channel. Besides, both of WINNER II and IMT-A channel models have only considered a rural environment for HSTs, while neglecting other HST scenarios. The statistical characterisation of WSS MIMO channels has been investigated extensively in the literature [125]–[127]. In contrast, only few papers [96], [97], [108], [115], [128], [129] have studied the statistical properties of non-stationary channels.

To fill the above research gaps, we will introduce a generic HST channel model that can be applied on different HST scenarios. The described generic channel model takes into account key parameters of the considered scenarios such as the scenario-specific time-variant Ricean K -factor and time-variant distance between Tx and Rx. It also consider the non-stationarity of HST scenarios by taking into account time-varying small-scale fading parameters, like AoAs and AoDs. The proposed generic model is applicable on three of the most common HST scenarios, i.e, open space, viaduct, and cutting. For example, these three scenarios form around 84% of the HST scenarios that can be encountered along the Zhengzhou-Xian HST line in China [83]. It is noteworthy that this generic model can be further applied on other HST scenario by choosing proper values of some of its key parameters.

The major contributions and novelties of this chapter are summarised as follows.

- 1) By considering the deployment of MRS in HST communication systems, we propose a theoretical GBSM for wideband non-stationary MIMO HST channels in different HST scenarios. The proposed model has time-varying angular parameters and time-varying distance between the Tx and Rx. Then, we derive

and study its time-variant ST CF, time-variant SD PSD, LSF, and time-variant LCR.

- 2) The aforementioned theoretical (reference) model assumes an infinite number of effective scatterers and therefore cannot be used for simulations. Thus, we further develop a corresponding SoS based simulation model for wideband non-stationary MIMO HST channels with reasonable complexity, i.e., a finite number of sinusoids or effective scatterers. The angle parameters of the proposed simulation model are calculated by adopting the MMEA. The relevant statistical properties of the developed simulation model are derived, verified by simulations, and compared with those of the proposed theoretical GBSM.
- 3) The utility of the proposed simulation model is validated using measurement data from different HST scenarios, i.e., ACF in viaduct scenario, LCR in viaduct and cutting scenarios, and stationary interval in the open space, viaduct and cutting scenarios.

The rest of this chapter is organised as follows. Section 4.2 proposes a theoretical non-stationary GBSM for wideband MIMO HST channels in the aforementioned HST scenarios and studies its statistical properties. In Section 4.3, the SoS simulation model for wideband MIMO HST channels is proposed and its statistical properties are investigated. Numerical and simulation results and verification with measurement data are presented in Section 4.4. Finally, conclusions are drawn in Section 4.5.

4.2 The Non-Stationary Wideband Theoretical GBSM

4.2.1 Description of the Wideband MIMO Theoretical Model

We adopt the IMT-A cellular network architecture for the HST communication system where MRSs are deployed on the surface of the train. Therefore, the end-to-end communications between the BS and MS will consist of two channels: outdoor channel and indoor one as illustrated in Fig. 4.1. Here, we will focus on the outdoor channel

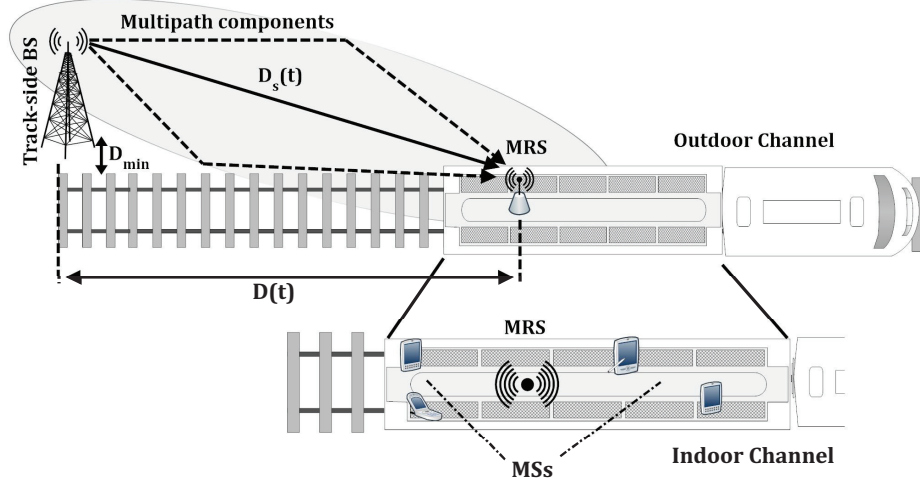


FIGURE 4.1: A HST communication system deploying MRSs.

between the BS and MRS. We consider a MIMO HST system with S transmit and U receive omni-directional antenna elements. The BS is considered to be located on the track-side with the minimum distance between the BS and the mid of the track denoted as D_{\min} m. $D_s(t) = \sqrt{(D_{\text{proj}}^2(t) + h^2)}$, where h is the relative height between BS and MRS, and $D_{\text{proj}}(t) = \sqrt{(D_{\min}^2 + D_{\text{ver}}^2(t))}$ is the projection of $D_s(t)$ on the railway track plane. The distance $D_{\text{ver}}(t)$ stands for the vertical distance between the bottom of the BS and the projection of the MRS location on the railway track plane. Fig. 4.2 illustrates the proposed GBSM, which consists of multiple confocal ellipses with single-bounced rays and the LoS component [130]. Geometric elliptical channel models have widely been used to model wideband MIMO channels [130]–[132]. Other GBSMs like one-ring and two-ring models have been mainly used to model narrowband MIMO channels and their extension to wideband channel models [133], [134] is not straightforward. For clarity purposes, we use a 2×2 MIMO channel model in Fig. 4.2 as an example. The parameters in Fig. 4.2 are defined in Table 4.1.

Based on the Tapped Delay Line (TDL) structure, the taps are represented by multiple confocal ellipses with the BS and MRS located at the foci. There are N_i effective scatterers on the i th ellipse (i.e., i th tap), where $i=1, 2, \dots, I$ and I is the total number of ellipses or taps. Each effective scatterer is intended to represent the effect of many physical scatterers within the region. The semi-major axis of the i th ellipse and the n_i th ($n_i=1, \dots, N_i$) effective scatterer are denoted by $a_i(t)$ and $s^{(n_i)}$, respectively. We

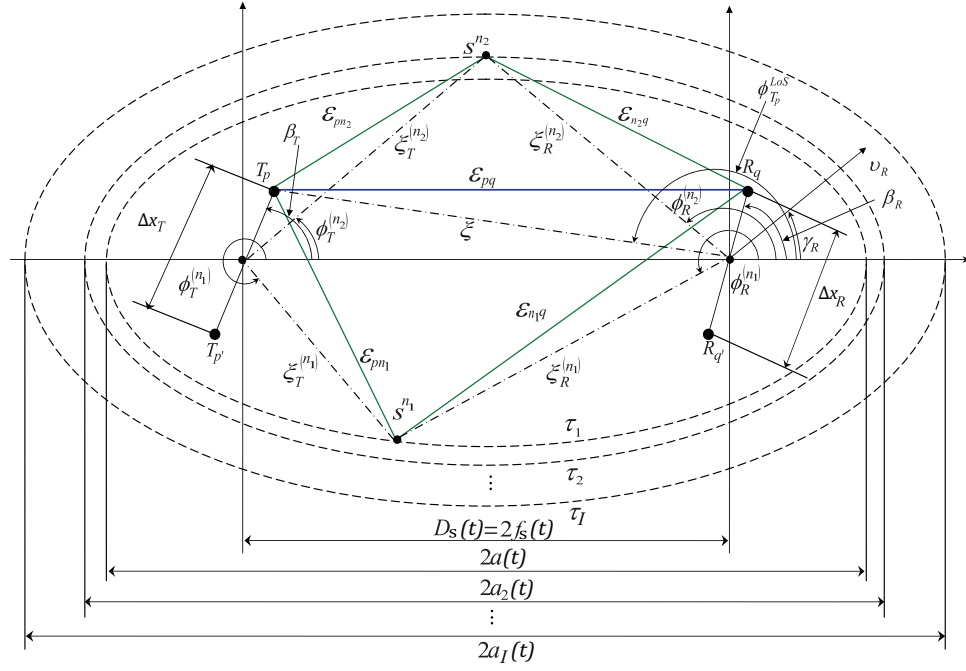


FIGURE 4.2: The GBSM for a wideband MIMO HST channel.

TABLE 4.1: Definition of parameters in Fig. 4.2.

Parameters	Definition
$D_s(t)$	distance between the BS and MRS
$f_s(t)$	half length of the distance between the two foci of ellipses
$a_i(t), b_i(t)$	semi-major axis and semi-minor axis of the i th ellipse, respectively
v_R, γ_R	MRS speed and angle of motion, respectively
$\Delta x_T, \Delta x_R$	antenna element spacings of the BS and MRS, respectively
β_T, β_R	tilt angles of the BS and MRS antenna arrays in the x-y plane, respectively
$\phi_{T_p}^{LoS}(t)$	AoA of the LoS path
$\phi_R^{(n_i)}(t)$	AoA of the wave travelling from an effective scatterer $s^{(n_i)}$ to the MRS
$\phi_T^{(n_i)}(t)$	AoD of the wave that impinges on the effective scatterer $s^{(n_i)}$
$\xi, \xi_T^{(n_i)}(t)$, and $\xi_R^{(n_i)}(t)$	distances $d(T_p, \text{MRS})$, $d(\text{BS}, s^{(n_i)})$, and $d(s^{(n_i)}, \text{MRS})$, respectively
$\epsilon_{pq}, \epsilon_{pn_i}, \epsilon_{n_iq}$	distances $d(T_p, R_q)$, $d(T_p, s^{(n_i)})$, and $d(s^{(n_i)}, R_q)$, respectively

denote the time-varying semi-minor axis of the i th ellipse as $b_i(t) = \sqrt{a_i^2(t) - f_s^2(t)}$, where $f_s(t) = D_s(t)/2$ represents a half of the distance between the two foci of ellipses. The tilt angles of the BS and MRS antenna arrays are denoted by β_T and β_R , respectively. The MRS moves with the same speed v_R as the train in the direction determined by the angle of motion γ_R . The AoA of the wave traveling from an effective scatterer $s^{(n_i)}$ to the MRS is denoted by $\phi_R^{(n_i)}(t)$. The AoD of the wave that impinges on the effective scatterer $s^{(n_i)}$ is denoted by $\phi_T^{(n_i)}(t)$, while $\phi_{T_p}^{LoS}(t)$ denotes the AoA of a LoS path.

Based on the TDL concept, the complex space-time-variant channel impulse response between the p th ($p=1, \dots, S$) element of the BS, T_p , and the q th ($q=1, \dots, U$) element of the MRS, R_q , can be expressed as $h(t, \tau, x) = h_{pq}(t, \tau) = \sum_{i=1}^I h_{i,pq}(t) \delta(\tau - \tau_i)$, where $h_{i,pq}(t)$ and τ_i denote the complex space-time-variant tap coefficients and the discrete propagation delay of the i th tap, respectively. Note that the space domain x is implicitly expressed by the subscript pq . From the above GBSM, the complex tap coefficients for the first tap ($i=1$) of the $T_p - R_q$ link is a superposition of the LoS component and Single-Bounced (SB) components, and can be expressed as

$$h_{1,pq}(t) = h_{1,pq}^{\text{LoS}}(t) + h_{1,pq}^{\text{SB}}(t) \quad (4.1)$$

where

$$h_{1,pq}^{\text{LoS}}(t) = \sqrt{\frac{K_{pq}}{K_{pq} + 1}} e^{-j2\pi f_c \tau_{pq}(t)} e^{j2\pi f_{\max} t \cos(\phi_{T_p}^{\text{LoS}}(t) - \gamma_R)} \quad (4.2a)$$

$$h_{1,pq}^{\text{SB}}(t) = \sqrt{\frac{\Omega_{1,pq}}{K_{pq}(t) + 1}} \sum_{n_1=1}^{N_1} \frac{1}{\sqrt{N_1}} e^{j(\psi_{n_1} - 2\pi f_c \tau_{pq,n_1}(t))} e^{j2\pi f_{\max} t \cos(\phi_R^{(n_1)}(t) - \gamma_R)}. \quad (4.2b)$$

The complex tap coefficients for other taps ($1 < i \leq I$) of the $T_p - R_q$ link is a sum of SB components only and can be expressed as

$$h_{i,pq}(t) = h_{i,pq}^{\text{SB}}(t) = \sqrt{\Omega_{i,pq}} \sum_{n_i=1}^{N_i} \frac{1}{\sqrt{N_i}} e^{j(\psi_{n_i} - 2\pi f_c \tau_{pq,n_i}(t))} e^{j2\pi f_{\max} t \cos(\phi_R^{(n_i)}(t) - \gamma_R)}, 1 < i \leq I. \quad (4.3)$$

It is worth mentioning that in (4.2a), (4.2b), and (4.3), we have time-varying parameters $\tau_{pq}(t)$, $\phi_{T_p}^{\text{LoS}}(t)$, $\tau_{pq,n_i}(t)$ ($i = 1, \dots, I$), and $\phi_R^{(n_i)}(t)$, which make the underlying GBSM a non-stationary one. If these parameters are not time-varying, then the GBSM can be reduced to a WSS one, as proposed in [130]. In the following, our task is to define or calculate the above time-varying parameters.

In (4.2a), (4.2b), and (4.3), $\Omega_{i,pq}$ designates the mean power for the i th tap, $\tau_{pq}(t) = \varepsilon_{pq}(t)/c$, and $\tau_{pq,n_i}(t) = (\varepsilon_{pn_i}(t) + \varepsilon_{n_iq}(t))/c$ are the travel times of the waves through the

links $T_p - R_q$ and $T_p - s^{(n_i)} - R_q$, respectively, as shown in Fig. 4.2. Here, c represents the speed of light and the symbol K_{pq} designates the Ricean factor. The phases ψ_{n_1} and ψ_{n_i} are Independent and Identically Distributed (i.i.d.) random variables with uniform distributions over $[-\pi, \pi)$ and f_{\max} is the maximum Doppler shift related to the MRS. From Fig. 4.2 and based on the law of cosines, we have [132]

$$\varepsilon_{pq}(t) \approx D_s(t) - k_p \Delta x_T \cos \beta_T - k_q \Delta x_R \cos(\phi_{T_p}^{\text{LoS}}(t) - \beta_R) \quad (4.4a)$$

$$\varepsilon_{pn_i}(t) \approx \xi_T^{(n_i)}(t) - k_p \Delta x_T \cos(\phi_T^{(n_i)}(t) - \beta_T) \quad (4.4b)$$

$$\varepsilon_{n_iq}(t) \approx \xi_R^{(n_i)}(t) - k_q \Delta x_R \cos(\phi_R^{(n_i)}(t) - \beta_R) \quad (4.4c)$$

where $k_p = (S - 2p + 1) / 2$, $k_q = (U - 2q + 1) / 2$, and $\xi_R^{(n_i)}(t) = b_i^2(t) / (a_i(t) + f_s(t) \cos \phi_R^{(n_i)}(t))$ with $\xi_T^{(n_i)}(t) = (a_i^2(t) + f_s^2(t) + 2a_i(t)f_s(t) \cos \phi_R^{(n_i)}(t)) / (a_i(t) + f_s(t) \cos \phi_R^{(n_i)}(t))$.

Note that the AoD $\phi_T^{(n_i)}(t)$ and AoA $\phi_R^{(n_i)}(t)$ are interdependent for SB rays. The relationship between the AoD and AoA for multiple confocal ellipses model can be given by [132]

$$\sin \phi_T^{(n_i)}(t) = \frac{b_i^2(t) \sin \phi_R^{(n_i)}(t)}{a_i^2(t) + f_s^2(t) + 2a_i(t)f_s(t) \cos \phi_R^{(n_i)}(t)} \quad (4.5a)$$

$$\cos \phi_T^{(n_i)}(t) = \frac{2a_i(t)f_s(t) + (a_i^2(t) + f_s^2(t)) \cos \phi_R^{(n_i)}(t)}{a_i^2(t) + f_s^2(t) + 2a_i(t)f_s(t) \cos \phi_R^{(n_i)}(t)}. \quad (4.5b)$$

The time-variant LoS AoA $\phi_{T_p}^{\text{LoS}}(t)$ can be expressed as [15]

$$\phi_{T_p}^{\text{LoS}}(t) = \begin{cases} \phi_{T_p}^{\text{LoS}}(t_0) + \arccos\left(\frac{D_s(t_0) + v_R t \cos \gamma_R}{D_s(t)}\right), & -\pi \leq \gamma_R \leq 0 \\ \phi_{T_p}^{\text{LoS}}(t_0) - \arccos\left(\frac{D_s(t_0) + v_R t \cos \gamma_R}{D_s(t)}\right), & 0 \leq \gamma_R \leq \pi \end{cases} \quad (4.6)$$

where $\phi_{T_p}^{\text{LoS}}(t_0) = \arcsin\left(\frac{k_p \Delta x_T}{D_s(t_0)} \sin \beta_T\right)$ denotes the initial LoS AoA at time $t = t_0$.

We assume that the numbers of effective scatterers in the theoretical model tend to infinity, i.e., $N_i \rightarrow \infty$. In this case, the discrete angles $\phi_T^{(n_i)}(t)$ and $\phi_R^{(n_i)}(t)$ can be replaced by continuous ones $\phi_T^{(i)}(t)$ and $\phi_R^{(i)}(t)$, respectively. scatterer distributions

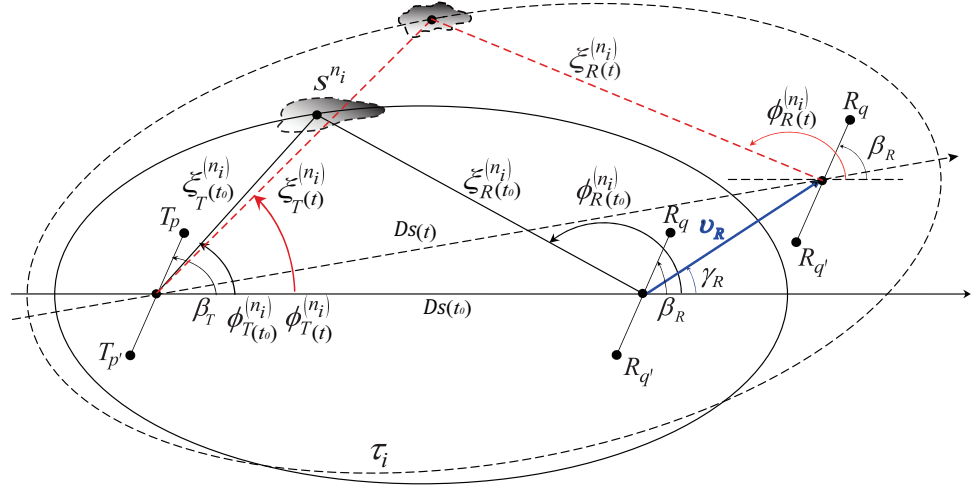


FIGURE 4.3: The time-varying angular parameters in the HST channel model.

like the uniform and Gaussian PDFs. Here, we use the von Mises PDF to describe the time-varying angles $\phi_T^{(n_i)}(t)$ and $\phi_R^{(n_i)}(t)$ as it is a general function and includes some well-known PDFs as special cases, e.g., uniform and Gaussian PDFs [132]. The von Mises PDF is defined as $f(\phi) \triangleq \exp[k \cos(\phi - \mu)] / [2\pi I_0(k)]$, where μ is the mean value of angle $\phi \in [-\pi, \pi)$, $I_0(\cdot)$ is the zeroth-order modified Bessel function of the first kind, and k ($k \geq 0$) is a positive real-valued parameter that controls the spread of ϕ . Applying the von Mises distribution to the time-varying AoAs, we get $f(\phi_R^{(i)})(t) \triangleq \exp[k_R^{(i)} \cos(\phi_R^{(i)} - \mu_R^{(i)}(t))] / [2\pi I_0(k_R^{(i)})]$, where $\mu_R^{(i)}$ is the mean angular value of the AoA $\phi_R^{(i)}$ and $k_R^{(i)}$ is the relevant von Mises parameter that controls the spread of $\phi_R^{(i)}$. Similarly, we can get $f(\phi_T^{(i)})(t)$ with $\mu_T^{(i)}$ and $k_T^{(i)}$.

In Fig. 4.3, the MRS is moving with the speed of v_R in the direction defined by the angle of motion γ_R . Correspondingly, the AoAs and the axes of the ellipses will be changed. Based on the geometric relations and by defining all the angles in Fig. 4.3, the time-varying function of mean AoA $\mu_R^{(i)}(t)$ can be derived as (4.7) [135]

$$\mu_R^{(i)}(t) = \begin{cases} \gamma_R - \arccos\left(\frac{v_R t - \xi_R^{(n_i)}(t_0) \cos(\gamma_R - \mu_R^{(i)}(t_0))}{\sqrt{\xi_R^{2(n_i)}(t_0) + (v_R t)^2 - 2\xi_R^{(n_i)}(t_0)v_R t \cos(\gamma_R - \mu_R^{(i)}(t_0))}}\right), & -\pi \leq \gamma_R \leq 0 \\ \gamma_R + \arccos\left(\frac{v_R t - \xi_R^{(n_i)}(t_0) \cos(\gamma_R - \mu_R^{(i)}(t_0))}{\sqrt{\xi_R^{2(n_i)}(t_0) + (v_R t)^2 - 2\xi_R^{(n_i)}(t_0)v_R t \cos(\gamma_R - \mu_R^{(i)}(t_0))}}\right), & 0 \leq \gamma_R \leq \pi. \end{cases} \quad (4.7)$$

4.2.1.1 Open space

The distance between the BS and the MRS can be calculated as $D_s(t) = \sqrt{D_{\text{proj}}^2(t) + h^2}$, where $h = H_{\text{BS}} - (H_{\text{train}} + H_{\text{MRS}})$, $D_{\text{proj}}(t) = \sqrt{D_{\text{min}}^2(t) + D_{\text{ver}}^2(t)}$, and $D_{\text{ver}}(t) = \left(\sqrt{D_{\text{ver}}^2(t_0) + (v_R t)^2} + 2D_{\text{ver}}(t_0) v_R t \cos \gamma_R \right)$.

4.2.1.2 Viaduct

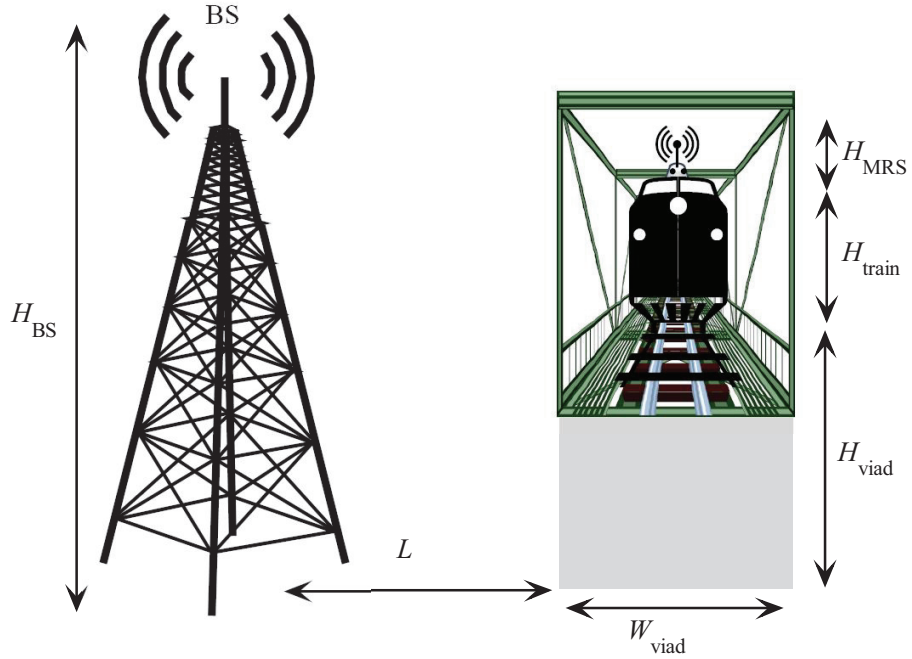


FIGURE 4.4: The viaduct scenario.

Fig. 4.4 shows a sectional view of the viaduct scenario with the main parameters of the viaduct structure that influence the wireless signal received by the MRS mounted on the top of the train. The impact of the parameters of the viaduct structure, especially the viaduct's height, H_{viad} , on the HST channel can be observed through the Ricean K -factor and the distance between BS and MRS as follows. The time-varying distance between the BS and MRS is $D_s(t) = \sqrt{(D_{\text{proj}}^2(t) + h^2)}$, where $h = H_{\text{BS}} - (H_{\text{viad}} + H_{\text{train}} + H_{\text{MRS}})$, $D_{\text{proj}}(t) = \sqrt{(D_{\text{min}}^2 + D_{\text{ver}}^2(t))}$, and $D_{\text{min}} = L + W_{\text{viad}}/2$.

The Ricean K -factor, $K_{pq}(t)$, in viaduct scenario can be expressed as

$$K_{pq}(t) = \begin{cases} 0.012D_s(t) + 0.29, & D_s(t) \leq D_{BP} \\ \left(-0.00037H_{\text{viad}} - \frac{0.18}{H_{\text{viad}}} + 0.017 \right) D_s(t) \\ \quad + \left(0.148H_{\text{viad}} + \frac{72}{H_{\text{viad}}} - 1.71 \right), & D_s(t) > D_{BP}. \end{cases} \quad (4.8)$$

where D_{BP} is the breakpoint distance that can be considered as the intercept distance used to remove the effect of the antenna.

4.2.1.3 Cutting

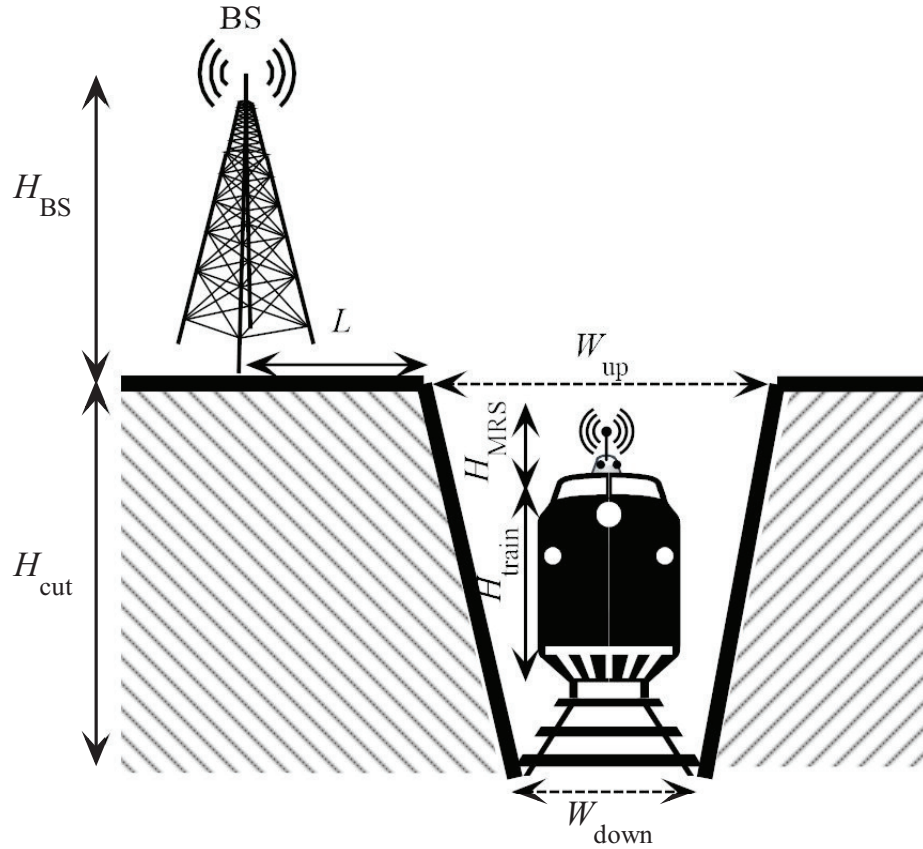


FIGURE 4.5: The cutting scenario.

A sectional view of the cutting scenario with the main parameters of the cutting structure is illustrated in Fig. 4.5. The cutting structure, especially the sides, has a significant impact on the HST wireless propagation characteristics. As we explained

earlier, the cutting scenario can be further classified into deep cutting ($H_{\text{cut}} > H_{\text{train}} + H_{\text{MRS}}$) and low cutting ($H_{\text{cut}} < H_{\text{train}} + H_{\text{MRS}}$) scenarios. While the high altitude of the BS results in a dominant LoS component at the MRS side, the richness of the scatterers at the sides of the cutting will increase the possibility of multipath components and may lead to a severe fading. The impact of the parameters of the cutting structure, especially the cuttings's dimensions, W_{up} and W_{down} are represented by the Ricean K -factor and the distance between BS and MRS. The relative height between BS and MRS can be calculated as $h = H_{\text{cut}} + H_{\text{BS}} - (H_{\text{train}} + H_{\text{MRS}})$ while $D_{\text{min}} = L + W_{\text{up}}/2$. The Ricean K -factor, $K_{pq}(t)$, in cutting scenario can be expressed as

$$K_{pq}(t) \text{ (dB)} = \begin{cases} 0.027D_s(t) + 0.41(W_{\text{up}} + W_{\text{down}}) - 30.78, & D_s(t) \leq D_{BP} \\ -0.0036D_s(t) + 0.41(W_{\text{up}} + W_{\text{down}}) - 24.66, & D_s(t) > D_{BP}. \end{cases} \quad (4.9)$$

Table 4.2 shows typical values of the different key scenario-specific parameters introduced earlier. These values are summarised based on a comprehensive survey of HST measurement campaigns in viaduct and cutting scenarios.

TABLE 4.2: Typical values of parameters in Figs. 4.4 & 4.5.

Viaduct	Values	Cutting	Values
H_{viad}	10 – 30 m	H_{cut}	2 – 10 m
H_{BS}	$H_{\text{viad}} + (20 - -30)$ m	H_{BS}	20 – 30 m
H_{MRS}	30 cm	H_{MRS}	30 cm
H_{train}	3.8 m	H_{train}	3.8 m
L	10 – 30 m	L	10 – 30 m
W_{viad}	10 – 20 m	W_{down}	14 – 20 m
		W_{up}	45 – 65 m

4.2.2 Statistical Properties of the Theoretical Model

In this subsection, we will derive the statistical properties of the proposed non-stationary HST GBSM based on the theoretical framework described in Section II under the US and antenna stationarity assumptions.

4.2.2.1 Time-variant ST CF

The correlation properties of two arbitrary channel impulse responses $h_{pq}(t, \tau)$ and $h_{p'q'}(t, \tau)$ of a wideband MIMO HST channel are determined by the correlation properties of $h_{i,pq}(t)$ and $h_{i,p'q'}(t)$ in each tap, since there is no correlation between the underlying processes in different taps. The normalised time-variant ST CF can be derived as

$$R_h(t, \Delta x_T, \Delta x_R, \Delta t) = \frac{\mathbb{E} \{h_{i,pq}(t) h_{i,p'q'}^*(t - \Delta t)\}}{\sqrt{\Omega_{i,pq} \Omega_{i,p'q'}}} \quad (4.10)$$

which can be obtained from the time-delay variant space CCF $R_h(t, \tau; \Delta t, \Delta x)$ in Fig. 3.6 with $\tau = 0$.

– In the case of the LoS component,

$$R_h^{\text{LoS}}(t, \Delta x_T, \Delta x_R, \Delta t) = K' e^{j2\pi [P \cos \beta_T - Q \cos(\phi_{T_p}^{\text{LoS}}(t) - \beta_R)]} \times e^{j2\pi f_{\max} \cos(\phi_{T_p}^{\text{LoS}}(t - \Delta t) - \gamma_R) \Delta t} \quad (4.11)$$

where $P = (p' - p) \Delta x_T / \lambda$, $Q = (q' - q) \Delta x_R / \lambda$, and $K' = \sqrt{\frac{K_{pq} K_{p'q'}}{(K_{pq} + 1)(K_{p'q'} + 1)}}$.

– In the case of the SB component,

$$R_h^{\text{SB}_i}(t, \Delta x_T, \Delta x_R, \Delta t) = \frac{1}{2\pi I_0(k_R^{(i)})} \int_{-\pi}^{\pi} e^{k_R^{(i)} \cos(\phi_R^{(i)} - \mu_R^{(i)}(t))} \times e^{j2\pi [P \cos(\phi_T^{(i)} - \beta_T) + Q \cos(\phi_R^{(i)} - \beta_R)]} e^{j2\pi \xi_{TR}^{(n_i)}(t, \Delta t)} e^{j2\pi f_{\max} \cos(\phi_R^{(i)} - \gamma_R) \Delta t} d\phi_R^{(i)} \quad (4.12)$$

where $\xi_{TR}^{n_i}(t, \Delta t) = \xi_T^{n_i}(t - \Delta t) - \xi_T^{n_i}(t) + \xi_R^{n_i}(t - \Delta t) - \xi_R^{n_i}(t)$.

By imposing $\Delta t = 0$ in (4.10), we get the normalised time-variant space CCF between two arbitrary channel coefficients as

$$\rho(t, \Delta x_T, \Delta x_R) = \frac{\mathbb{E} \{h_{i,pq}(t) h_{i,p'q'}^*(t)\}}{\sqrt{\Omega_{i,pq} \Omega_{i,p'q'}}} = R_h(t, \Delta x_T, \Delta x_R, 0). \quad (4.13)$$

– In the case of the LoS component,

$$\rho^{\text{LoS}}(t, \Delta x_T, \Delta x_R) = K' e^{j2\pi [P \cos \beta_T - Q \cos(\phi_{T_p}^{\text{LoS}}(t) - \beta_R)]}. \quad (4.14)$$

– In the case of the SB component,

$$\begin{aligned} \rho^{\text{SB}_i}(t, \Delta x_T, \Delta x_R) = & \frac{1}{2\pi I_0(k_R^{(i)})} \int_{-\pi}^{\pi} e^{k_R^{(i)} \cos(\phi_R^{(i)} - \mu_R^{(i)}(t))} \\ & \times e^{j2\pi [P \cos(\phi_T^{(i)} - \beta_T) + Q \cos(\phi_R^{(i)} - \beta_R)]} d\phi_R^{(i)}. \end{aligned} \quad (4.15)$$

The normalised time-variant space CCF for the first tap ($i=1$) can be expressed as the summation of (4.14) and (4.15) with $i=1$, i.e.,

$$\rho_1(t, \Delta x_T, \Delta x_R) = \rho^{\text{LoS}}(t, \Delta x_T, \Delta x_R) + \rho^{\text{SB}_1}(t, \Delta x_T, \Delta x_R). \quad (4.16)$$

Similarly, the normalised time-variant ACF can be obtained by imposing $\Delta x_T = 0$ and $\Delta x_R = 0$ in (4.10), i.e.,

$$r(t, \Delta t) = \frac{\mathbb{E} \{h_{i,pq}(t) h_{i,pq}^*(t - \Delta t)\}}{\sqrt{\Omega_{i,pq} \Omega_{i,p'q'}}} = R_h(t, 0, 0, \Delta t). \quad (4.17)$$

– In the case of the LoS component,

$$r^{\text{LoS}}(t, \Delta t) = \frac{K_{pq}}{1 + K_{pq}} e^{j2\pi f_{\max} \cos(\phi^{\text{LoS}}(t - \Delta t) - \gamma_R) \Delta t}. \quad (4.18)$$

– In the case of the SB component,

$$\begin{aligned} r^{\text{SB}_i}(t, \Delta t) = & \frac{1}{2\pi I_0(k_R^{(i)}) (1 + K_{pq})} \int_{-\pi}^{\pi} e^{k_R^{(i)} \cos(\phi_R^{(i)} - \mu_R^{(i)}(t))} \\ & \times e^{j2\pi \xi_{TR}^{(n_i)}(t, \Delta t)} e^{j2\pi f_{\max} \cos(\phi_R^{(i)} - \gamma_R) \Delta t} d\phi_R^{(i)}. \end{aligned} \quad (4.19)$$

Therefore, the normalised time-variant ACF for the first tap ($i=1$) can be expressed as the summation of (4.18) and (4.19) with $i=1$, i.e.,

$$r_1(t, \Delta t) = r^{\text{LoS}}(t, \Delta t) + r^{\text{SB}_1}(t, \Delta t). \quad (4.20)$$

4.2.2.2 Time-variant SD PSD

The time-variant SD PSD can be obtained from the time-variant ST CF by applying the Fourier transformation in terms of Δt , i.e.,

$$W(t, \nu, \Delta x_T, \Delta x_R) = \int R_h(t, \Delta x_T, \Delta x_R, \Delta t) e^{-j2\pi\nu\Delta t} d\Delta t. \quad (4.21)$$

–In case of the LoS component,

$$W^{\text{LoS}}(t, \nu, \Delta x_T, \Delta x_R) = K' e^{j2\pi \left[P \cos \beta_T - Q \cos(\phi_{T_p}^{\text{LoS}}(t) - \beta_R) \right]} \delta(\nu - (G(t) + v_R)) \quad (4.22)$$

where $G(t) = f_{\max} \cos(\phi_{T_p}^{\text{LoS}}(t) - \gamma_R)$.

–In case of the SB component,

$$W^{\text{SB}_i}(t, \nu, \Delta x_T, \Delta x_R) = \int R_h^{\text{SB}_i}(t, \Delta x_T, \Delta x_R, \Delta t) e^{-j2\pi\nu\Delta t} d\Delta t. \quad (4.23)$$

This integral will have to be evaluated numerically.

4.2.2.3 LSF

It can be obtained from the time-variant space-time-frequency CF $R_L(t; \Delta t, \Delta f, \Delta x)$ using Fourier transform with respect to Δt and Δx and inverse Fourier transform with respect to Δf , i.e.,

$$C_H(t, \tau, \nu, \Omega) = \int \int \int R_L(t; \Delta t, \Delta f, \Delta x) e^{-j2\pi(\nu\Delta t - \tau\Delta f + \Omega\Delta x)} d\Delta t d\Delta f d\Delta x. \quad (4.24)$$

where the time-variant space-time-frequency CF can be obtained from (3.1c) after considering the US and antenna stationarity assumptions, i.e.,

$$R_L(t; \Delta t, \Delta f, \Delta x) = \frac{\mathbb{E} \left\{ L_{H_{pq}}(t, f) L_{H_{p'q'}}^*(t - \Delta t, f - \Delta f) \right\}}{\sqrt{\Omega_{i,pq} \Omega_{i,p'q'}}}. \quad (4.25)$$

Here, $L_{H_{pq}}(t, f)$ is the space-time-variant transfer function that can be obtained by

$$L_{H_{pq}}(t, f) = \int h_{pq}(t, \tau) e^{-j2\pi f \tau} d\tau. \quad (4.26)$$

– In the case of the LoS component,

$$\begin{aligned} R_L^{\text{LoS}}(t; \Delta t, \Delta f, \Delta x) &= K' e^{j2\pi [P \cos \beta_T - Q \cos(\phi_{T_p}^{\text{LoS}}(t) - \beta_R)]} \\ &\quad \times e^{j2\pi f_{\max} \cos(\phi_{T_p}^{\text{LoS}}(t) - \gamma_R) \Delta t - \Delta f \tau_1} \end{aligned} \quad (4.27)$$

where

$$C_H^{\text{LoS}}(t, \tau, \nu, \Omega) = \int \int \int R_L^{\text{LoS}}(t; \Delta t, \Delta f, \Delta x) e^{-j2\pi(\nu \Delta t - \tau \Delta f + \Omega \Delta x)} d\Delta t d\Delta f d\Delta x. \quad (4.28)$$

– In the case of the SB component,

$$C_H^{\text{SB}_i}(t, \tau, \nu, \Omega) = \int \int \int R_L^{\text{SB}_i}(t; \Delta t, \Delta f, \Delta x) e^{-j2\pi(\nu \Delta t - \tau \Delta f + \Omega \Delta x)} d\Delta t d\Delta f d\Delta x \quad (4.29)$$

where the time-variant space-time-frequency CF $R_L^{\text{SB}_i}(t; \Delta t, \Delta f, \Delta x)$ can be expressed as

$$\begin{aligned} R_L^{\text{SB}_i}(t; \Delta t, \Delta f, \Delta x) &= \frac{1}{2\pi I_0(k_R^{(i)}) U} \int_{-\pi}^{\pi} e^{k_R^{(i)} \cos(\phi_R^{(i)} - \mu_R^{(i)}(t))} e^{j2\pi f_{\max} \cos(\phi_R^{(i)} - \gamma_R) \Delta t} \\ &\quad \times e^{j2\pi [P \cos(\phi_T^{(i)} - \beta_T) + Q \cos(\phi_R^{(i)} - \beta_R)]} e^{-j2\pi \Delta f \tau_i} d\phi_R^{(i)}. \end{aligned} \quad (4.30)$$

It is important to mention that all the investigated statistical properties in this section, i.e., $R_h(t, \Delta x_T, \Delta x_R, \Delta t)$, $\rho(t, \Delta x_T, \Delta x_R)$, $r(t, \Delta t)$, $W(t, \nu, \Delta x_T, \Delta x_R)$, and $C_H(t, \tau, \nu, \Omega)$, are time-variant due to the non-stationarity of the proposed GBSM. For

stationary channel models, the corresponding statistical properties are not dependent on t .

4.2.2.4 Time-variant LCR

The LCR, $L(t, r)$, is by definition the average number of times per second that the signal envelope, $|h_{pq}(t)|$, crosses a specified level r with positive/negative slope. Using the traditional PDF-based method [136], we derive the expression of LCR for HST channels as

$$L(t, r) = \frac{2r\sqrt{K_{pq}(t)+1}}{\pi^{3/2}} B(t) e^{-K_{pq}(t)-(K_{pq}(t)+1)r^2} \int_0^{\pi/2} \cosh\left(2\sqrt{K_{pq}(t)(K_{pq}(t)+1)}r\cos\theta\right) \times \left[e^{-(\chi(t)\sin\theta)^2} + \sqrt{\pi}\chi(t)\sin\theta \cdot \text{erf}(\chi(t)\sin\theta)\right] d\theta, \quad (4.31)$$

where $\cosh(\cdot)$ is the hyperbolic cosine function, $\text{erf}(\cdot)$ is the error function, $B(t) = \sqrt{\frac{b_2(t)}{b_0(t)} - \frac{b_1^2(t)}{b_0^2(t)}}$, and $\chi(t)$ is equal to $\sqrt{\frac{K_{pq}(t)b_1^2(t)}{(b_0(t)b_2(t)-b_1^2(t))}}$. Finally, parameters $b_0(t)$, $b_1(t)$, and $b_2(t)$ are defined as

$$b_0(t) \triangleq \text{E}\{h_{pq}^I(t)^2\} = \text{E}\{h_{pq}^Q(t)^2\}, \quad (4.32a)$$

$$b_1(t) \triangleq \text{E}\{h_{pq}^I(t)\dot{h}_{pq}^Q(t)\} = \text{E}\{h_{pq}^Q(t)\dot{h}_{pq}^I(t)\}, \quad (4.32b)$$

$$b_2(t) \triangleq \text{E}\{\dot{h}_{pq}^I(t)^2\} = \text{E}\{\dot{h}_{pq}^Q(t)^2\}, \quad (4.32c)$$

where $h_{pq}^I(t)$ and $h_{pq}^Q(t)$ denote the in-phase and quadrature components of the complex fading envelope $h_{pq}(t)$, and $\dot{h}_{pq}^I(t)$ and $\dot{h}_{pq}^Q(t)$ denote the first derivative of $h_{pq}^I(t)$ and $h_{pq}^Q(t)$, respectively.

Using (4.1) – (4.3), the parameters $b_0(t)$, $b_1(t)$, and $b_2(t)$ can be calculated as

$$b_0(t) = \frac{1}{K_{pq}(t)+1}, \quad (4.33a)$$

$$b_1(t) = \frac{b_0(t)}{N_i} \sum_{n_i=1}^{N_i} f_{\max} \cos(\phi_R^{(n_i)} - \gamma_R), \quad (4.33b)$$

$$b_2(t) = \frac{b_0(t)}{N_i} \sum_{n_i=1}^{N_i} \left[f_{\max} \cos(\phi_R^{(n_i)} - \gamma_R) \right]^2. \quad (4.33c)$$

4.3 The Simulation Model for Wideband MIMO HST channels

4.3.1 Description of the Wideband MIMO Simulation Model

The proposed theoretical model assumes an infinite number of effective scatters and hence it cannot be used for simulations. Therefore, we need to develop a HST simulation model, which can be obtained from the theoretical one by utilising only a finite number of scatterers N . The complex space-time-variant tap coefficient of the first tap of the link T_p – R_q for the simulation model can be expressed as

$$\tilde{h}_{1,pq}(t) = \tilde{h}_{1,pq}^{\text{LoS}}(t) + \tilde{h}_{1,pq}^{\text{SB}}(t) \quad (4.34)$$

where

$$\tilde{h}_{1,pq}^{\text{LoS}}(t) = \sqrt{\frac{K_{pq}}{K_{pq} + 1}} e^{-j2\pi f_c \tau_{pq}(t)} e^{j \left[2\pi f_{\max} t \cos(\tilde{\phi}_{T_p}^{\text{LoS}}(t) - \gamma_R) \right]} \quad (4.35a)$$

and

$$\tilde{h}_{1,pq}^{\text{SB}}(t) = \sqrt{\frac{\Omega_{1,pq}}{K_{pq} + 1}} \sum_{n_1=1}^{N_1} \frac{1}{\sqrt{N_1}} e^{j(\psi_{n_1} - 2\pi f_c \tau_{pq,n_1}(t))} e^{j \left[2\pi f_{\max} t \cos(\tilde{\phi}_R^{(n_1)}(t) - \gamma_R) \right]}. \quad (4.35b)$$

The complex space-time-variant channel coefficient for the rest of the taps ($1 < i \leq I$) can be expressed as

$$\begin{aligned} \tilde{h}_{i,pq}(t) = \tilde{h}_{i,pq}^{\text{SB}}(t) = \sqrt{\Omega_{i,pq}} \sum_{n_i=1}^{N_i} \frac{1}{\sqrt{N_i}} e^{j(\psi_{n_i} - 2\pi f_c \tau_{pq,n_i}(t))} \\ \times e^{j[2\pi f_{\max} t \cos(\tilde{\phi}_R^{(n_i)}(t) - \gamma_R)]}, 1 < i \leq I. \end{aligned} \quad (4.36)$$

By comparing the simulation and theoretical models and considering the fact that the AoDs are related to the AoAs, we only need to determine the discrete AoA $\left\{ \tilde{\phi}_R^{(n_i)} \right\}_{n_i=1}^{N_i}$ for the simulation model. In case of isotropic scattering, i.e., $k_R^{(i)} = 0$, the quantities $\left\{ \tilde{\phi}_R^{(n_i)} \right\}_{n_i=1}^{N_i}$ should preferably be computed using the Extended Method of Exact Doppler Spread (EMEDS) [131], while MMEA and the Lp -Norm Method (LPNM) provide high quality solutions when the scattering is non-isotropic [131]. Here, we consider a non-isotropic scattering environment and hence we will use MMEA to calculate $\left\{ \tilde{\phi}_R^{(n_i)} \right\}_{n_i=1}^{N_i}$ for the simulation model. By applying the MMEA, the AoAs $\left\{ \tilde{\phi}_R^{(n_i)} \right\}_{n_i=1}^{N_i}$ can be determined by finding the solutions of the following equation using numerical root-finding techniques [131]:

$$\frac{n_i - \frac{1}{4}}{N_i} - \int_{\mu_R^{(i)}(t_0) - \pi}^{\tilde{\phi}_R^{(n_i)}} f(\phi_R^{(i)})(t_0) d\phi_R^{(i)} = 0, \quad n_i = 1, 2, \dots, N_i. \quad (4.37)$$

The value of N_i needs to be chosen carefully. Too small N_i will lead to inaccurate results, while too large N_i results in time-consuming simulations. Our investigations have demonstrated that choosing $N_i = 50$ is a reasonable compromise between complexity and accuracy. It is also worth noting that this agrees with the suggestion given in [131, p. 451] that the reasonable values of N_i are in the range from 40 to 50. In the future, when more HST measurement campaigns become available in the literature, a guidance to select N_i for different HST environments can be introduced.

4.3.2 Statistical Properties of the Simulation Model

Based on our wideband MIMO HST theoretical model and its statistical properties, the corresponding statistical properties for the simulation model can be derived by using discrete angle parameters.

4.3.2.1 Time-variant ST CF

The normalised time-variant ST CF can be calculated by

$$\tilde{R}_h(t, \Delta x_T, \Delta x_R, \Delta t) = \frac{\mathbb{E} \left\{ \tilde{h}_{i,pq}(t) \tilde{h}_{i,p'q'}^*(t - \Delta t) \right\}}{\sqrt{\Omega_{i,pq} \Omega_{i,p'q'}}}. \quad (4.38)$$

– In the case of the LoS component,

$$\begin{aligned} \tilde{R}_h^{\text{LoS}}(t, \Delta x_T, \Delta x_R, \Delta t) = & K' e^{j2\pi [P \cos \beta_T - Q \cos(\tilde{\phi}_{Tp}^{\text{LoS}}(t) - \beta_R)]} \\ & \times e^{j2\pi f_{\max} \cos(\tilde{\phi}^{\text{LoS}}(t - \Delta t) - \gamma_R) \Delta t}. \end{aligned} \quad (4.39)$$

– In the case of the SB component,

$$\begin{aligned} \tilde{R}_h^{\text{SB}_i}(t, \Delta x_T, \Delta x_R, \Delta t) = & \frac{1}{N_i U} \sum_{n_i=1}^{N_i} e^{j2\pi [P \cos(\tilde{\phi}_T^{(n_i)}(t) - \beta_T) + Q \cos(\tilde{\phi}_R^{(n_i)}(t) - \beta_R)]} \\ & \times e^{j2\pi \xi_{TR}^{(n_i)}(t, \Delta t)} e^{j2\pi f_{\max} \cos(\tilde{\phi}_R^{(n_i)}(t) - \gamma_R) \Delta t}. \end{aligned} \quad (4.40)$$

Similar to the procedure applied to the theoretical model, the normalised time-variant space CCF and the time-variant ACF of the simulation model can be expressed as

$$\tilde{\rho}(t, \Delta x_T, \Delta x_R) = \frac{\mathbb{E} \left\{ \tilde{h}_{i,pq}(t) \tilde{h}_{i,p'q'}^*(t) \right\}}{\sqrt{\Omega_{i,pq} \Omega_{i,p'q'}}} = \tilde{R}_h(t, \Delta x_T, \Delta x_R, 0) \quad (4.41)$$

$$\tilde{r}(t, \Delta t) = \frac{\mathbb{E} \left\{ \tilde{h}_{i,pq}(t) \tilde{h}_{i,pq}^*(t - \Delta t) \right\}}{\sqrt{\Omega_{i,pq} \Omega_{i,p'q'}}} = \tilde{R}_h(t, 0, 0, \Delta t) \quad (4.42)$$

respectively.

4.3.2.2 Time-variant SD PSD

The time-variant SD PSD of the simulation model $\tilde{W}(t, \nu, \Delta x_T, \Delta x_R)$ can be obtained from the ST CF by applying the Fourier transform in terms of Δt . Therefore, it can be expressed similar to (4.21) by replacing $R_h(t, \Delta x_T, \Delta x_R, \Delta t)$ by $\tilde{R}_h(t, \Delta x_T, \Delta x_R, \Delta t)$.

– In case of the LoS component, $\tilde{W}^{\text{LoS}}(t, \nu, \Delta x_T, \Delta x_R)$ can be obtained by replacing $\phi_{T_p}^{\text{LoS}}$ by $\tilde{\phi}_{T_p}^{\text{LoS}}$ in (4.22).

– In case of the SB component, time-variant SD PSD $\tilde{W}^{\text{SB}_i}(t, \nu, \Delta x_T, \Delta x_R)$ can be obtained from (4.23) by substituting $R_h^{\text{SB}_i}(t, \Delta x_T, \Delta x_R, \Delta t)$ by $\tilde{R}_h^{\text{SB}_i}(t, \Delta x_T, \Delta x_R, \Delta t)$.

4.3.2.3 LSF

Analogous to the theoretical model, the LSF of the simulation model $\tilde{C}_H(t, \tau, \nu, \Omega)$ can be obtained from the time-frequency-space CF $\tilde{R}_L(t; \Delta t, \Delta f, \Delta x)$. Therefore, the derived equations can be obtained from (4.24)–(4.29) by replacing the theoretical model functions and the continuous model parameters, e.g., $\phi_R^{(i)}$ with the corresponding simulation model functions and discrete model parameters, e.g., $\tilde{\phi}_R^{(n_i)}$. As a result, the LSFs of the simulation model can be expressed as

$$\tilde{C}_H(t, \tau, \nu, \Omega) = \int \int \int \tilde{R}_L(t; \Delta t, \Delta f, \Delta x) e^{-j2\pi(\nu\Delta t - \tau\Delta f + \Omega\Delta x)} d\Delta t d\Delta f d\Delta x \quad (4.43)$$

with

$$\tilde{R}_L(t, \Delta t, \Delta f, \Delta x) = \frac{\mathbb{E} \left\{ \tilde{L}_{H_{pq}}(t, f) \tilde{L}_{H_{p'q'}}^*(t - \Delta t, f - \Delta f) \right\}}{\sqrt{\Omega_{i,pq} \Omega_{i,p'q'}}} \quad (4.44)$$

where $\tilde{L}_{H_{pq}}(t, f)$ is the space-time-variant transfer function that can be obtained from

$$\tilde{L}_{H_{pq}}(t, f) = \int \tilde{h}_{pq}(t, \tau) e^{-j2\pi f \tau} d\tau. \quad (4.45)$$

– In the case of the LoS component,

$$\tilde{R}_L^{\text{LoS}}(t; \Delta t, \Delta f, \Delta x) = K' e^{j2\pi \left[P \cos \beta_T - Q \cos(\tilde{\phi}_{T_p}^{\text{LoS}}(t) - \beta_R) \right]}$$

$$\times e^{j2\pi f_{\max} \cos(\tilde{\phi}_{Tp}^{\text{LoS}}(t) - \gamma_R) \Delta t - \Delta f \tau_1} \quad (4.46)$$

$$\begin{aligned} \tilde{C}_H^{\text{LoS}}(t, \tau, \nu, \Omega) = & \int \int \int \tilde{R}_L^{\text{LoS}}(t; \Delta t, \Delta f, \Delta x) \\ & \times e^{-j2\pi(\nu \Delta t - \tau \Delta f + \Omega \Delta x)} d\Delta t d\Delta f d\Delta x. \end{aligned} \quad (4.47)$$

– In the case of the SB component,

$$\begin{aligned} \tilde{R}_L^{\text{SB}_i}(t; \Delta t, \Delta f, \Delta x) = & \frac{1}{N_i U} \sum_{n_i=1}^{N_i} e^{j2\pi f_{\max} \cos(\tilde{\phi}_R^{(n_i)}(t) - \gamma_R) \Delta t} \\ & \times e^{j2\pi [P \cos(\tilde{\phi}_T^{(n_i)}(t) - \beta_T) + Q \cos(\tilde{\phi}_R^{(n_i)}(t) - \beta_R)]} e^{-j2\pi \Delta f \tau_i} \end{aligned} \quad (4.48)$$

$$\begin{aligned} \tilde{C}_H^{\text{SB}_i}(t, \tau, \nu, \Omega) = & \int \int \int \tilde{R}_L^{\text{SB}_i}(t; \Delta t, \Delta f, \Delta x) \\ & \times e^{-j2\pi(\nu \Delta t - \tau \Delta f + \Omega \Delta x)} d\Delta t d\Delta f d\Delta x. \end{aligned} \quad (4.49)$$

4.3.2.4 Time-variant LCR

Similar to the aforementioned statistical properties, the time-variant LCR of the simulation model can be obtained from the one of the theoretical model by replacing the continuous model parameters, e.g., $\phi_R^{(i)}$ with the corresponding simulation model functions and discrete model parameters, e.g., $\tilde{\phi}_R^{(n_i)}$.

4.4 Results and Analysis

In this section, the statistical properties of the proposed theoretical model and simulation model are evaluated and analysed. Then, the proposed simulation channel model is further validated by measurements.

4.4.1 Open space

The parameters for our analysis in open space scenario are listed here or specified otherwise: the LoS Ricean factor $K_{pq} = K_{p'q'} = 6$, taps delays for the first and second taps are $\tau_1 = 0$ and $\tau_2 = 35$ ns, respectively, as for the RMa scenario in [33], $v_R = 360$ km/h, $f_c = 4$ GHz, and thus $f_{\max} = 1.34$ KHz, $D_s(t_0) = 1000$ m, $D_{\min} = 50$ m as in [15], $a_1(t_0) = \frac{D_s(t_0)}{2} + 5$ m, $a_2(t_0) = \frac{D_s(t_0)}{2} + 10.25$ m, $\xi_R^{(n_i)}(t_0) = 600$ m, $\gamma_R = 30^\circ$, $\mu_R^{(i)}(t_0) = 45^\circ$, $k_R^{(i)} = 6$ and we use a linear antenna array with $U = S = 2$ and $\beta_R = \beta_T = 60^\circ$.

4.4.1.1 Time-variant ST CFs

By adopting a BS antenna element spacing $\Delta x_T = \lambda$, the absolute values of the time-variant space CCF of non-stationary HST MIMO channel model are illustrated in Fig. 4.6(a) and Fig. 4.6(b). By using (4.16) and imposing $i=2$ in (4.15), Fig. 4.6(a) shows the absolute values of the time-variant space CCF of the first and second taps of the theoretical model at two different time instants, i.e., $t=0$ s and 2 s. From the figure, we can easily notice the higher correlation in the first tap in comparison with the second one because of the dominant LoS component. To highlight the impact of the time-varying parameters on channel statistical properties, Fig. 4.6(b) shows the absolute values of the time-variant space CCF of the second tap with time-variant and time-invariant angular parameters. It shows that time-varying angles are the only time-varying parameters that affect the time-variant space CCF. The same conclusion can be drawn from (4.15). Fig. 4.7 shows a comparison between the time-variant space CCFs of the theoretical model (4.15), simulation model (4.41), and simulation results with $N=50$ for BS antenna spacing $\Delta x_T = \lambda$ at different time instants $t=0$ s and 2 s. It shows that the simulation model provides a fairly good approximation to the theoretical one especially at small antenna spacings. The simulation results fit the simulation model very well, demonstrating the correctness of both theoretical derivations and simulations.

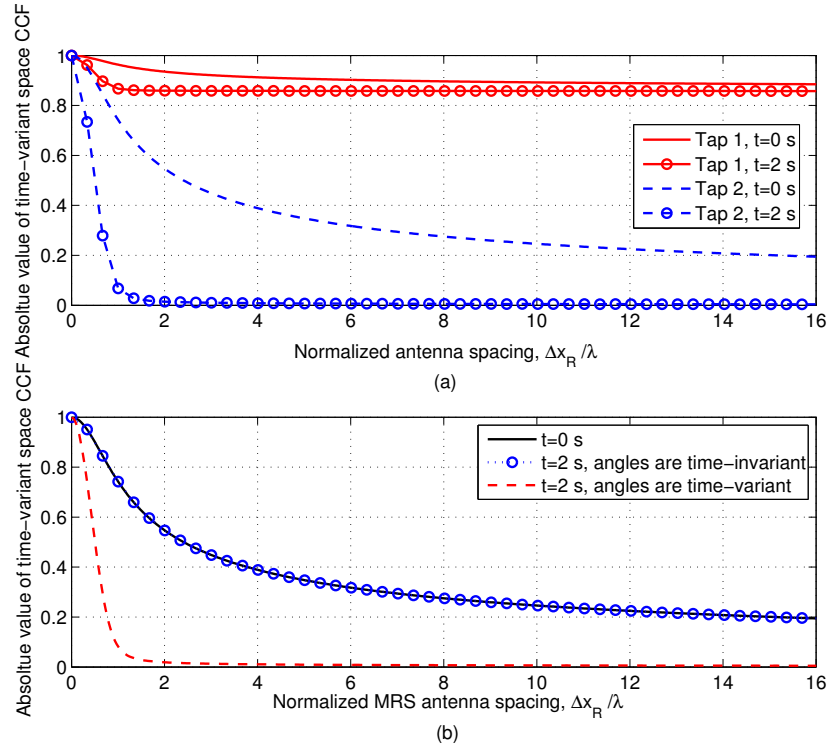


FIGURE 4.6: (a) The absolute values of the time-variant space CCF of different taps of the proposed HST channel model at different time instants. (b) The absolute values of the time-variant space CCF of the second tap with/without time-varying angular parameters.

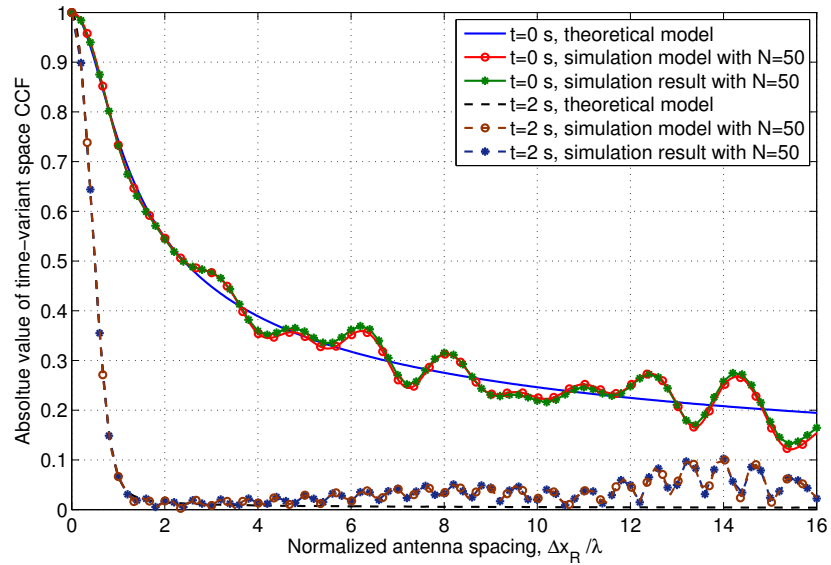


FIGURE 4.7: Comparison between the time-variant space CCFs of the second tap of the theoretical model and simulation model for different time instants.

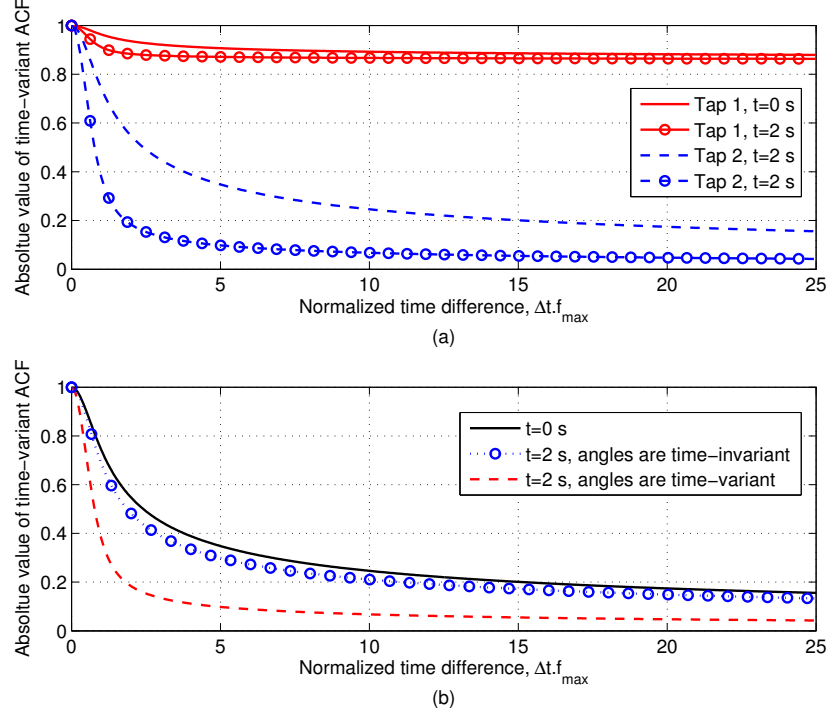


FIGURE 4.8: (a) The absolute values of the time-variant ACF of different taps of the proposed HST channel model at different time instants. (b) The absolute values of the time-variant ACF with/without time-varying angular parameters.

By using (4.20) and imposing $i = 2$ in (4.15), Fig. 4.8(a) shows the absolute values of the time-variant ACF of different taps of the proposed theoretical HST channel model at different time instants. A higher correlation in the first tap in comparison with the second can be easily noticed. Again, this is due to the dominant LoS component. Fig. 4.8(b) shows the absolute values of the time-variant ACF of the second tap with/without time-varying angular parameters. We can see that even with time-invariant angles, the absolute value of the time-variant ACF still changes with time because of the time-varying dimensions of the ellipses. The same conclusion can be drawn from (4.19). From this figure, we can also calculate *coherence time*, which quantifies the duration within which the channel is approximately constant and can be defined as the smallest value of Δt that fulfills the condition $|r(t, \Delta t)| = \frac{1}{2}|r(0, \Delta t)|$. The coherence time for time-variant and time-invariant angular parameters is equal to 1 ms and 4 ms, respectively. It is important to mention that the smaller the coherence time, the larger the Doppler spread. Fig. 4.9 shows a comparison between the time-variant ACFs of the second tap of the theoretical model (4.19), simulation model

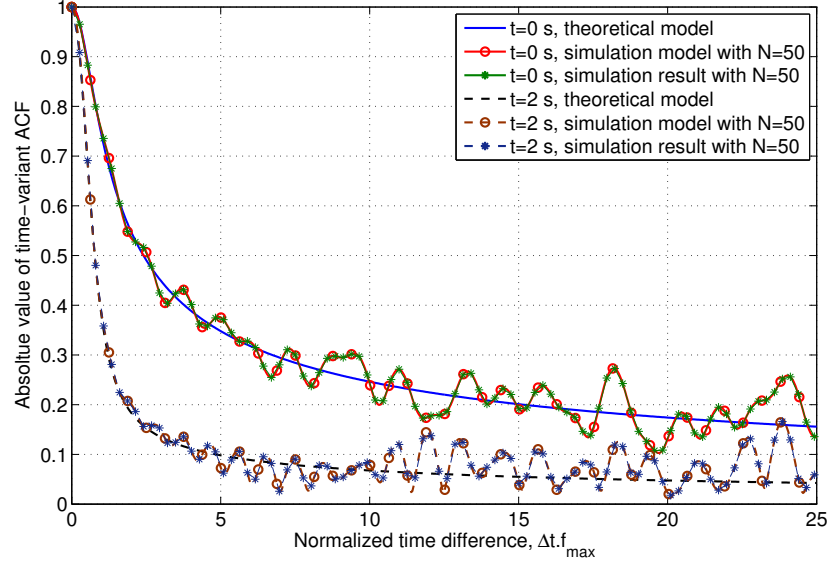


FIGURE 4.9: Comparison between the time-variant ACFs of the second tap of the theoretical model and simulation model for different time instants.

(4.42), and simulation results for different time instants. Again, the simulation model provides a fairly good approximation to the theoretical one especially in small values of time separation. The simulation results and (4.42) of the simulation model match very well, illustrating the correctness of the derivation of (4.42) and simulations.

4.4.1.2 Time-variant SD PSDs

Fig. 4.10 compares the time-variant SD PSDs of the theoretical model (4.21) for isotropic (i.e., $k_R = 0$) and non-isotropic (i.e., $k_R > 0$) scenarios at different time instants with $\Delta x_T = \Delta x_R = \lambda$. We can easily notice that the SD PSD is U-shaped for isotropic case only. To understand the impact of the angular parameters on SD PSD given in (4.23) for the theoretical model and the corresponding simulation model, Fig. 4.11 shows normalised SD PSDs of both models for different angular parameters, i.e., the angle of motion γ_R and the initial mean AoA $\mu_R(t_0)$. From this figure, it can be concluded that angular parameters of channel models affect considerably the trends of the time-variant SD PSDs.

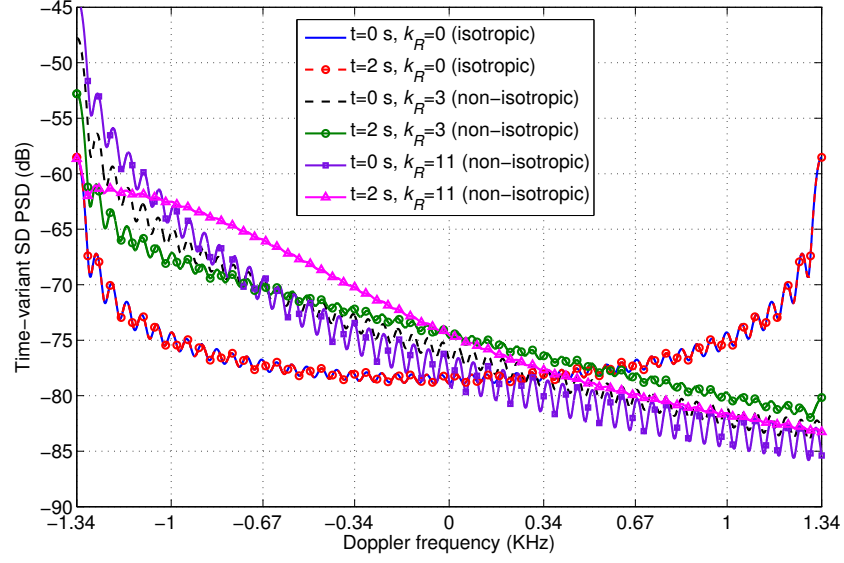


FIGURE 4.10: Time-variant SD PSDs of the theoretical model for different scenarios ($v_R = 360$ km/h, $f_{\max} = 1.34$ KHz): isotropic: $k_R = 0$ & non-isotropic: $k_R = 3$ & 11.

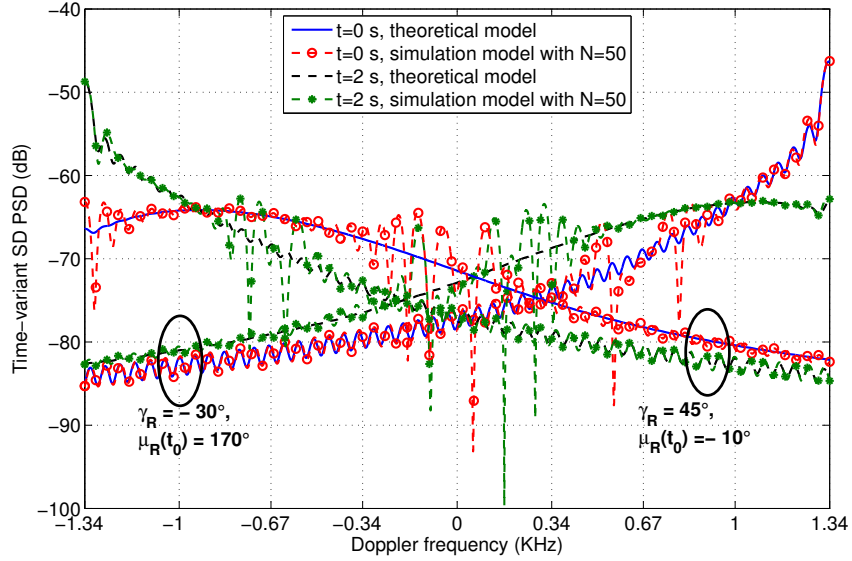


FIGURE 4.11: Time-variant SD PSDs of the theoretical and simulation models for different angular parameters ($v_R = 360$ km/h, $f_{\max} = 1.34$ KHz, $k_R = 11$).

4.4.1.3 LSFs

Fig. 4.12 shows a comparison between the LSFs of the theoretical model and simulation model with $N=50$ for different time instants. It can be noticed how the power of the effective scatterers varies with time t and the power of the components with

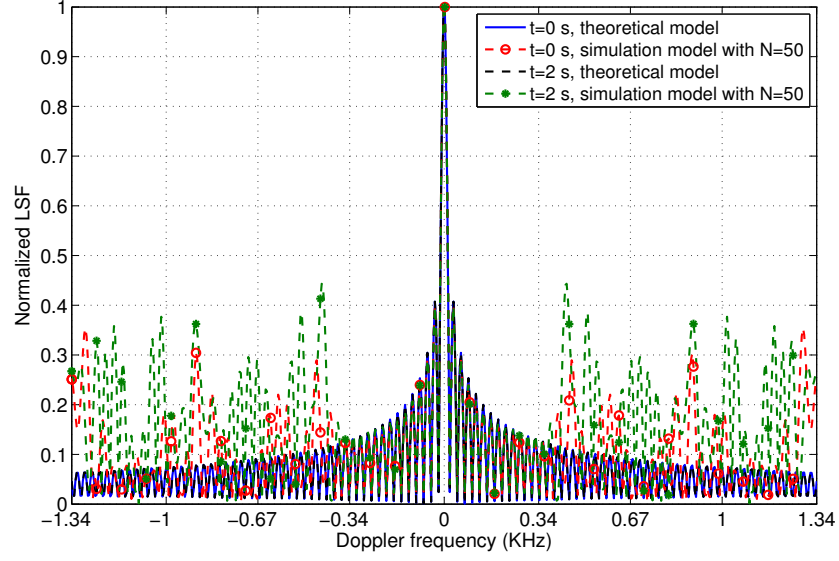


FIGURE 4.12: Comparison between the LSFs of the second tap of the theoretical model and the simulation model for different time instants.

zero Doppler frequency is higher than the rest of the components. Simulation model shows good approximation to the theoretical one at different time instants. different time instants due to the non-stationarity of the HST channel. They also demonstrate that simulation model provides a good approximation to the statistical properties of the theoretical one.

4.4.1.4 Stationary Interval/Stationary Distance

To verify our proposed channel models, we use HST measurement data presented in [77] where the authors compared the stationary interval of a measured HST channel with that of standard channel models such as IMT-A and WINNER II. The stationary interval can be calculated using Averaged Power Delay Profile (APDP) that can be expressed as [77]

$$\overline{P}_h(t_k, \tau) = \frac{1}{N_{PDP}} \sum_k^{k+N_{PDP}-1} |\tilde{h}_{pq}(t_k, \tau)|^2 \quad (4.50)$$

where N_{PDP} is the number of power delay profiles to be averaged, t_k is the time of the k -th drop (snapshot), and $\tilde{h}_{pq}(t_k, \tau) = \sum_{i=1}^I \tilde{h}_{i,pq}(t_k) \delta(\tau - \tau_i)$. The correlation

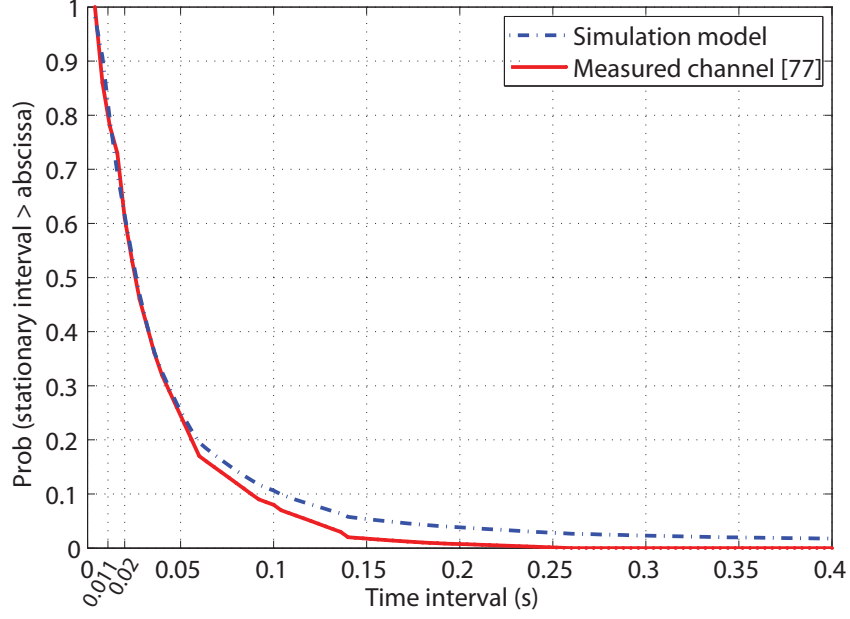


FIGURE 4.13: The empirical CCDFs of stationary intervals for the proposed HST simulation model and a measured HST channel [77].

coefficient between two APDPs can be calculated as

$$c(t_k, \Delta t) = \frac{\int \overline{P_h}(t_k, \tau) \overline{P_h}(t_k + \Delta t, \tau) d\tau}{\max\{\int \overline{P_h}(t_k, \tau)^2 d\tau, \int \overline{P_h}(t_k + \Delta t, \tau)^2 d\tau\}}. \quad (4.51)$$

The stationary interval can be then calculated as

$$T_s(t_k) = \max\{\Delta t | c(t_k, \Delta t) \geq c_{\text{thresh}}\}, \quad (4.52)$$

where c_{thresh} is a given threshold of the correlation coefficient.

Analogously, the stationary distance can be calculated as

$$SD(t_k) = \max\{\Delta D | c(t_k, \Delta t) \geq c_{\text{thresh}}\}, \quad (4.53)$$

where $\Delta D = v_R \times \Delta t$.

Fig. 4.13 shows the empirical Complementary Cumulative Distribution Function (CCDF) of stationary intervals for our proposed HST simulation model and the measured HST channel using the following simulation parameters obtained from [77]: $f_c = 930$ MHz,

$v_R = 324$ km/h, $N_{PDP} = 15$, $c_{\text{thresh}} = 0.8$. It is worth mentioning that since the measured HST channel is a narrowband one, in (4.50) we used $\tilde{h}_{pq}(t_k, \tau) = \tilde{h}_{1,pq}(t_k) \delta(\tau - \tau_1)$ where $\tilde{h}_{1,pq}(t_k)$ is given in (4.34). The excellent agreement between the proposed HST simulation model and the measurement data demonstrates the utility of our HST channel models. From Fig. 4.13, the stationary interval is equal to 11 ms for 80% and 20 ms for 60% which is considerably shorter than the ones reported for standardised channel models, i.e., 37.8 ms for 60% as we previously mentioned in the introduction.

4.4.2 Viaduct

Here, we compare the derived ACF and LCR with the ones of the measured HST channel in viaduct scenario reported in [63]. Unless specified otherwise, the parameters for our analysis, obtained from the measurement campaign in [63], are: $f_c = 930$ MHz, $v_R = 180$ km/h, $L = 15$ m, $H_{\text{viad}} = 20$ m, $H_{\text{BS}} = 44$ m, $H_{\text{MRS}} = 30$ cm, $H_{\text{train}} = 3.8$ m, cellular radius = 2502 m, therefore, $D_s(t) \in [0, 2502)$ m, $a_1 = \frac{D_s}{2} + 150$ m, $D_{BP} = 400$ m, $\gamma_R = 0$, and $N = 50$.

4.4.2.1 Time-variant ACF

Fig. 4.14 shows the absolute values of the ACFs of the proposed generic HST model and the measured ACF taken from Fig. 9 (Case 3) in [63]. Since the measurement has been conducted under GSM-R system, the measured channel is a narrowband one and hence we used $h_{pq}(t, \tau) = h_{1,pq}(t) \delta(\tau - \tau_1)$ where $h_{1,pq}(t)$ is given in (4.1). It is noteworthy that the ACFs in Fig. 4.14 are plotted as functions of distance $\Delta D = v_R \times \Delta t$ for comparison purposes.

4.4.2.2 Time-variant LCR

Fig. 4.15 shows the LCR of the measured channel, obtained from Fig. 8 in [63], and the derived LCRs of the proposed generic HST channel model. The very good agreement

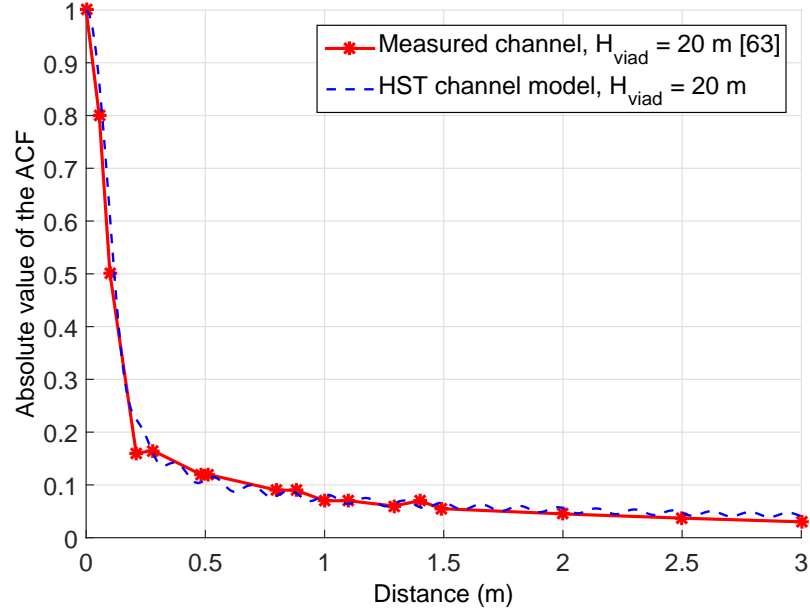


FIGURE 4.14: The absolute values of the time-variant ACFs of the generic HST channel model a measured HST channel in viaduct scenario [63] ($f_c = 930$ MHz, $v_R = 180$ km/h, $L = 15$ m, $H_{\text{viad}} = 20$ m, $H_{\text{BS}} = 44$ m, $H_{\text{MRS}} = 30$ cm, $H_{\text{train}} = 3.8$ m, $D_{\text{BP}} = 400$ m, $\gamma_R = 0$, $\beta_R = \beta_T = 45^\circ$, $\mu_R^{(i)}(t_0) = 63^\circ$, $k_R^{(i)} = 2.7$, $N = 50$).

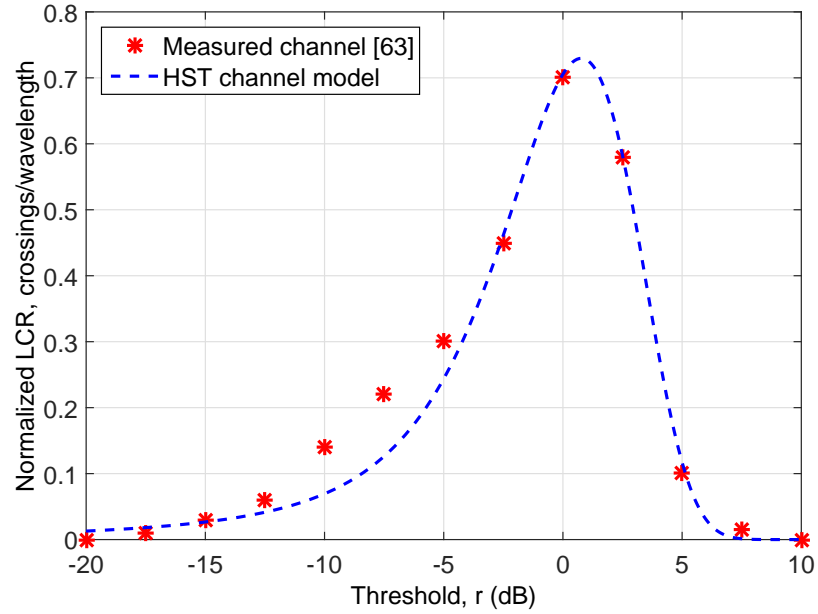


FIGURE 4.15: The LCRs of the generic HST channel model and a measured HST channel in viaduct scenario [63] ($f_c = 930$ MHz, $v_R = 180$ km/h, $L = 15$ m, $H_{\text{viad}} = 20$ m, $H_{\text{BS}} = 44$ m, $H_{\text{MRS}} = 30$ cm, $H_{\text{train}} = 3.8$ m, $D_{\text{BP}} = 400$ m, $\gamma_R = 0$, $\beta_R = \beta_T = 60^\circ$, $\mu_R^{(i)}(t_0) = 85^\circ$, $k_R^{(i)} = 7.3$, $N = 50$).

between the proposed generic model and the measurement data demonstrates the utility of our HST generic channel model in viaduct scenarios.

4.4.3 Cutting

We use the measurement in [71] to verify the applicability of the proposed generic model in cutting scenario. The simulation parameters, obtained from the measurement campaign reported in [71], are listed here or specified otherwise: $f_c = 930$ MHz, $v_R = 260$ km/h, $L = 15$ m, $H_{\text{cut}} = 7.1$ m, $H_{\text{BS}} = 28$ m, $H_{\text{MRS}} = 30$ cm, $H_{\text{train}} = 3.8$ m, $W_{\text{up}} = 53.93$ m, $W_{\text{down}} = 17.78$ m, cellular radius = 1410 m, therefore, $D_s(t) \in [0, 1410)$ m, $a_1 = \frac{D_s}{2} + 150$ m, $D_{BP} = 200$ m, $\gamma_R = 0$, and $N = 50$.

4.4.3.1 Time-variant ACF

Fig. 4.16 shows the absolute values of the ACFs $r(t, \Delta t)$ of the proposed generic HST model using different cutting's dimensions. Two cuttings scenarios from [71] are considered, i.e., Cutting 1 ($W_{\text{up}} = 53.93$ m & $W_{\text{down}} = 14.78$ m) and Cutting 2 ($W_{\text{up}} = 58.30$ m & $W_{\text{down}} = 15.16$ m). A higher correlation in Cutting 2 in comparison with Cutting 1 can be noticed. This can be explained based on the difference in the cuttings' dimensions. Since Cutting 2 is wider than Cutting 1, a stronger LoS component represented by a higher K -factor value will be observed at the receiver according to 4.9 which in turn will result in higher ACF values.

4.4.3.2 Time-variant LCR

Fig. 4.17 shows the normalised LCR of the measured channel, obtained from Fig. 9(a) in [71], and the derived LCRs of the proposed generic HST channel model. The simulation results of the HST channel model and the measured channel match very well.

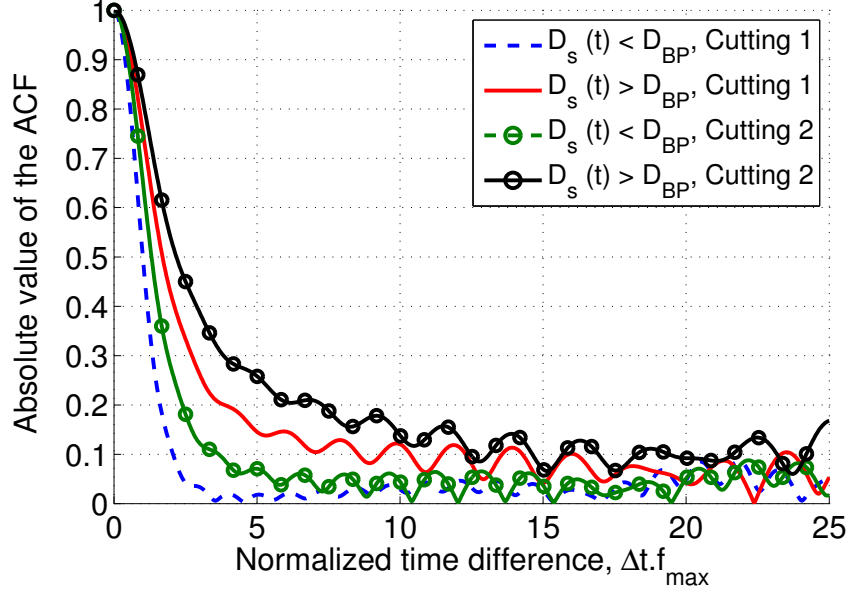


FIGURE 4.16: The absolute values of the time-variant ACFs of the generic HST channel model for different cuttings' dimensions [71] (Cutting 1: $W_{\text{up}} = 53.93$ m & $W_{\text{down}} = 14.78$ m, Cutting 2: $W_{\text{up}} = 58.30$ m & $W_{\text{down}} = 15.16$ m, $f_c = 930$ MHz, $v_R = 260$ km/h, $L = 15$ m, $H_{\text{cut}} = 7.1$ m, $H_{\text{BS}} = 28$ m, $H_{\text{MRS}} = 30$ cm, $H_{\text{train}} = 3.8$ m, $D_{\text{BP}} = 200$ m, $\gamma_R = 0$, $\beta_R = \beta_T = 45^\circ$, $\mu_R^{(i)}(t_0) = 63^\circ$, $k_R^{(i)} = 15$, $N = 50$).

4.4.3.3 Stationary Distance

Finally, Fig. 4.18 shows the stationary distances of the generic HST channel model in viaduct and cutting scenarios based on the measurement setup parameters reported in [137]. The simulation parameters, obtained from the aforementioned measurement campaign [137], are: viaduct ($f_c = 1.89$ GHz, $v_R = 285$ km/h, $L = 15$ m, $H_{\text{viad}} = 20$ m, $H_{\text{BS}} = 20$ m, $H_{\text{MRS}} = 30$ cm, $H_{\text{train}} = 3.8$ m); cutting: ($f_c = 2.35$ GHz, $v_R = 200$ km/h, $L = 20$ m, $H_{\text{cut}} = 5$ m, $H_{\text{BS}} = 28$ m, $H_{\text{MRS}} = 30$ cm, $H_{\text{train}} = 3.8$ m, $W_{\text{up}} = 40$ m, $W_{\text{down}} = 16$ m). The mean values of the stationary distances of the viaduct and cutting scenarios are 3.26 m and 2.86 m, respectively. This agrees with the range of the measured averaged stationary intervals that is reported in [137] as 2.8 m - 4.2 m.

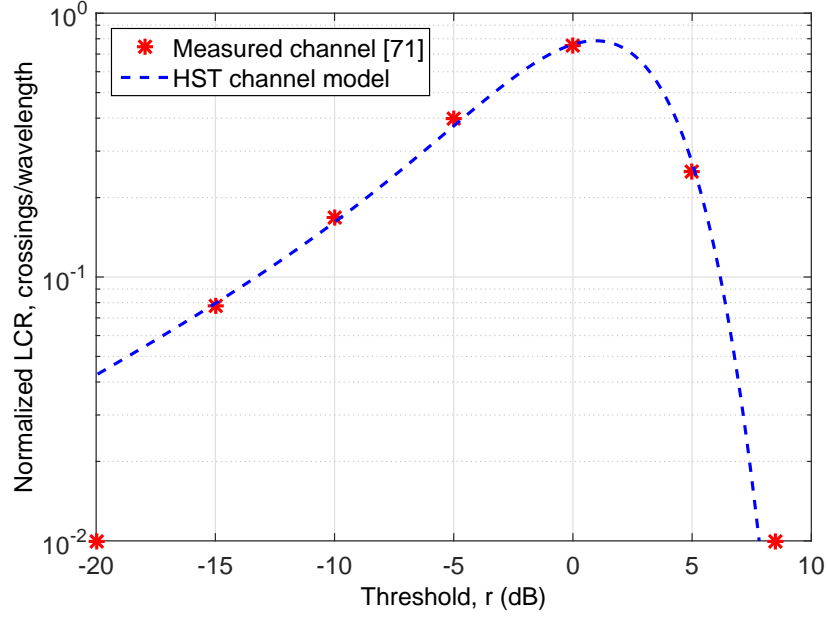


FIGURE 4.17: The LCRs of the generic HST channel model and a measured HST channel in cutting scenario [71] ($f_c = 930$ MHz, $v_R = 260$ km/h, $L = 15$ m, $H_{\text{cut}} = 7.1$ m, $H_{\text{BS}} = 28$ m, $H_{\text{MRS}} = 30$ cm, $H_{\text{train}} = 3.8$ m, $W_{\text{up}} = 53.93$ m, $W_{\text{down}} = 14.78$ m, $D_{BP} = 200$ m, $\gamma_R = 0$, $\beta_R = \beta_T = 60^\circ$, $\mu_R^{(i)}(t_0) = 145^\circ$, $k_R^{(i)} = 4$, $N = 50$).

4.5 Summary

In this chapter, we have proposed a generic non-stationary theoretical wideband MIMO HST GBSM for the outdoor channel of HST communication systems adopting MRS technology. This generic model takes into account the impact of different scenario-specific parameters of each HST scenario on the wireless channel, e.g., the height of the viaduct and the dimensions of the cuttings. The proposed model contains time-varying model parameters, i.e., angular parameters, Ricean K -factor, and distance between the Tx and Rx. Using the MMEA, a corresponding SoS simulation model has been developed. Both models can be further used to model non-stationary V2I channels. The statistical properties of both models have been investigated based on a proposed framework that describes non-stationary channels. Numerical analyses have shown that these statistical properties experience different behaviours at different time instants, demonstrating the capability of the proposed models to mimic the non-stationarity of HST channels. The dominance of the LoS component has resulted in higher correlation in the first tap of the proposed channel models in comparison

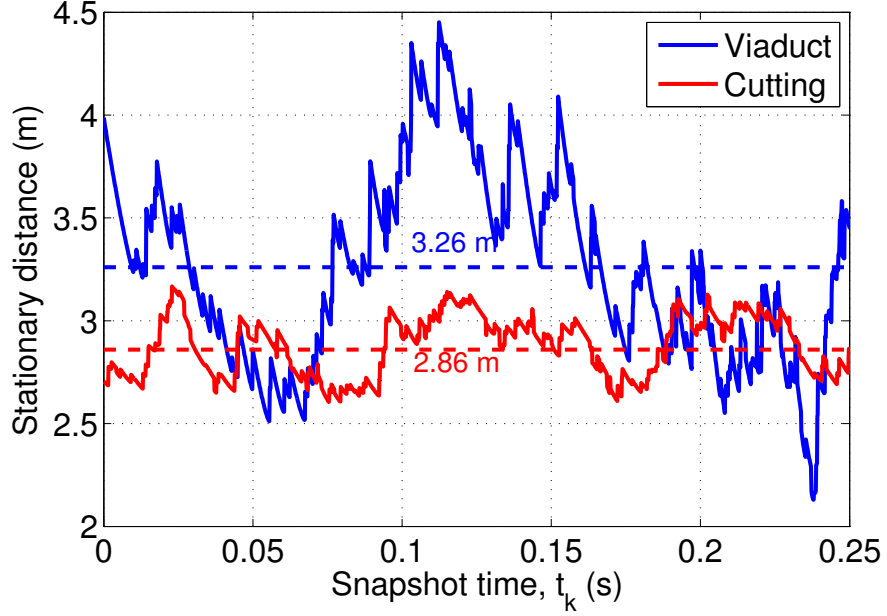


FIGURE 4.18: The stationary distances of the generic HST channel model in viaduct and cutting scenarios (viaduct: $f_c = 1.890$ GHz, $v_R = 285$ km/h, $L = 15$ m, $H_{\text{viad}} = 20$ m, $H_{\text{BS}} = 20$ m, $H_{\text{MRS}} = 30$ cm, $H_{\text{train}} = 3.8$ m, cutting: $f_c = 2.35$ GHz, $v_R = 200$ km/h, $L = 20$ m, $H_{\text{cut}} = 5$ m, $H_{\text{BS}} = 28$ m, $H_{\text{MRS}} = 30$ cm, $H_{\text{train}} = 3.8$ m, $W_{\text{up}} = 40$ m, $W_{\text{down}} = 16$ m).

with the second one. It has also been demonstrated that the time-varying angles will affect the time-variant space CCFs and time-variant ACFs while time-varying dimensions of the ellipses will only have an influence on the time variant ACFs. Moreover, the trends of the time-variant SD PSDs are considerably affected by the angular parameters of the channel models. For all statistical properties, the simulation model provides good approximation to the theoretical one. Finally, it has been shown that the statistical properties of our simulation model match well those of the measured data from three of the most common HST scenarios, i.e., open space, viaduct, and cutting, which validates the utility of the proposed model.

Chapter 5

A Generic 3D Non-Stationary Wideband MIMO Channel Model for Different High-Speed Train Scenarios

5.1 Introduction

HST channels were generally proposed and measured assuming that propagation waves are travelling in two dimensions and hence ignore the impact of the elevation angle on channel statistics. However, in reality, radio waves propagate in three dimensions and scatterers are dispersed in elevation, i.e., vertical plane, as well as in azimuth, i.e., the horizontal plane. Until very recently, the standardisation of MIMO channel models was based on the 2D assumption for the location of the scatterers, reflectors, and Tx/Rx antennas such as the 3rd Generation Partnership Project (3GPP)/3GPP2 Spatial Channel Model (SCM) [138], SCM-Extension (SCM-E) [139], WINNER II [34], and IMT-A [33] channel models. This 2D assumption limits the MIMO transmission techniques, e.g., beamforming and spatial multiplexing, to the azimuth plane [140]. The significance of elevation angles in describing the radio propagation more accurately has urged researchers to extend the 2D channel models to 3D ones [141]. Consequently, 3D extensions of SCM and the WINNERII/WINNER+ channel models

were proposed in [142] and [143], and an extension of the IMT-A channel model to the elevation plane was proposed in [144], [145]. Recently, the 3GPP has developed a 3D channel model in Urban Micro-cell (UMi) and Urban Macro-cell (UMa) scenarios following the framework of WINNER II channel model [146]. The proposed 3D 3GPP channel model introduced the Zenith Angles of Departure (ZoD) and Zenith Angles of Arrival (ZoA) that are modelled by inverse Laplacian functions [147]. However, none of the aforementioned channel models has consider any of the HST scenarios.

The geometry-based 3D channel models for HST channels can be classified in terms of their perspective modelling approach to GBDMs and GBSMs. GBDMs, that characterise channel parameters in a purely deterministic manner, are in general based on ray-tracing, which exploits high-frequency approximation of Maxwells equation, and thus needs a detailed and time-consuming description of the site-specific propagation scenarios. Therefore, GBDMs typically have high complexity and cannot be easily generalised. Examples of 3D HST GBDMs can be found in [91]–[93], [102]. GBSMs determine the physical parameters in a stochastic manner with or without presuming any underlying geometry and thus can be easily used to deal with various scenarios. GBSMs are generally derived from some predefined stochastic distribution of the scatterers/clusters by applying the fundamental laws of wave propagation. Therefore, they can be easily adapted to diverse scenarios by modifying the stochastic distribution and properties of scatterers/clusters and the shape of the scattering region. their direct involvement of scatterers/clusters renders GBSMs as one of the most promising candidates for 3D channel modelling. A 3D one-sphere RS-GBSM was proposed in [94] for open space scenario. However, this 3D channel model was proposed under the narrowband GSM-R system and it assumed that the HST channel satisfies the WSS condition that has been proved incorrect by measurements [7], [46].

In Chapter 4, a 2D multiple ellipse GBSM with time-variant angular parameters and time-variant Ricean K -factor was proposed for non-stationary MIMO HST channels. Here, this model will be extended to a 3D one by considering the elevation angular parameters. Moreover, a circular-cylinder around the Rx, i.e., the MRS in relay-supported communication systems, is considered in order to simulate the impact of

scatterers that surround the Rx. Furthermore, another level of non-stationarity of the HST channel is introduced by utilising Markov processes to simulate the birth/death process of the MPCs, which is reported in HST measurements [59]. The rest of the Chapter is organised as follows. In Section 5.2, the generic theoretical 3D non-stationary wideband MIMO HST channel model is proposed and the related time-variant channel model parameters are presented. The statistical properties of the proposed theoretical 3D HST channel model are also derived in Section 5.2. In Section 5.3, the corresponding 3D SoS simulation model for wideband MIMO HST channels is developed, and its statistical properties are investigated. Numerical and simulation results are presented and analysed in Section 5.4. Finally, the conclusions are drawn in Section 5.5.

5.2 Novel 3D Wideband Non-stationary MIMO HST Theoretical Channel Models

5.2.1 Description of the 3D Wideband MIMO Theoretical Model

Fig. 5.2 shows a typical HST communication scenario with LoS and single-bounced rays. The proposed generic wideband model employs a RS-GBSM approach to represent the multi-path propagation channel between a Tx and a Rx. Let us now consider a 3D wideband MIMO HST communication system with U transmit and S receive omni-directional antenna elements. The MIMO fading channel can be described by a matrix $\mathbf{H}(t) = [h_{pq}(t, \tau)]_{U \times S}$ of size $U \times S$. Figs. 5.2 and 5.3 illustrate the detailed 3D wideband HST channel model between the Tx and Rx with LoS components and single-bounced scattering.

We use the circular-cylinder model to mimic the nearby scattering (e.g., the slopes of the cutting, the structure of the viaduct, the acoustic barriers at along the railway tracks in open-space scenario) and the multiple confocal elliptic-cylinder models to

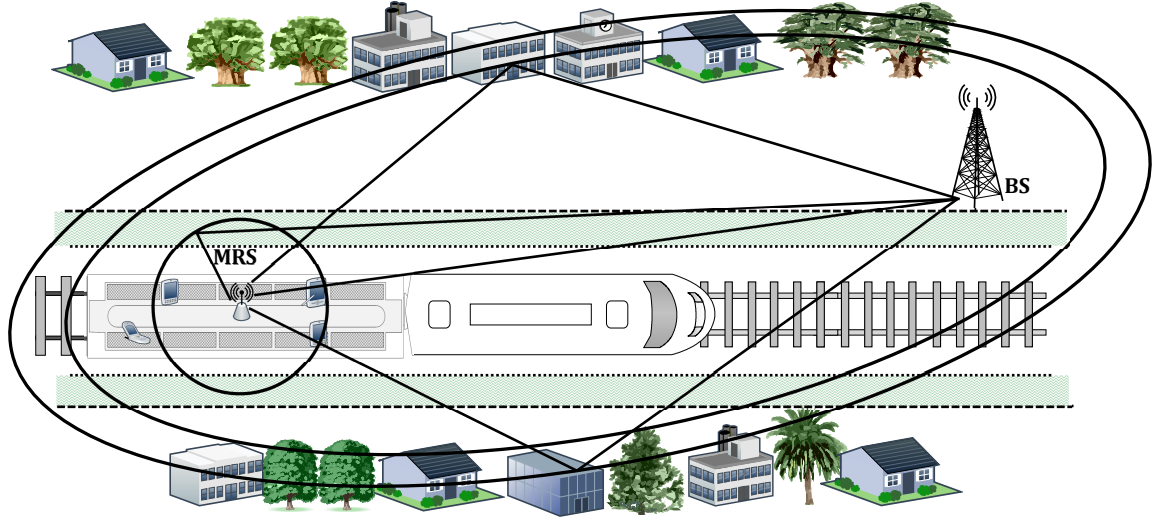


FIGURE 5.1: HST communication system in cutting scenario with LoS and single-bounced rays.

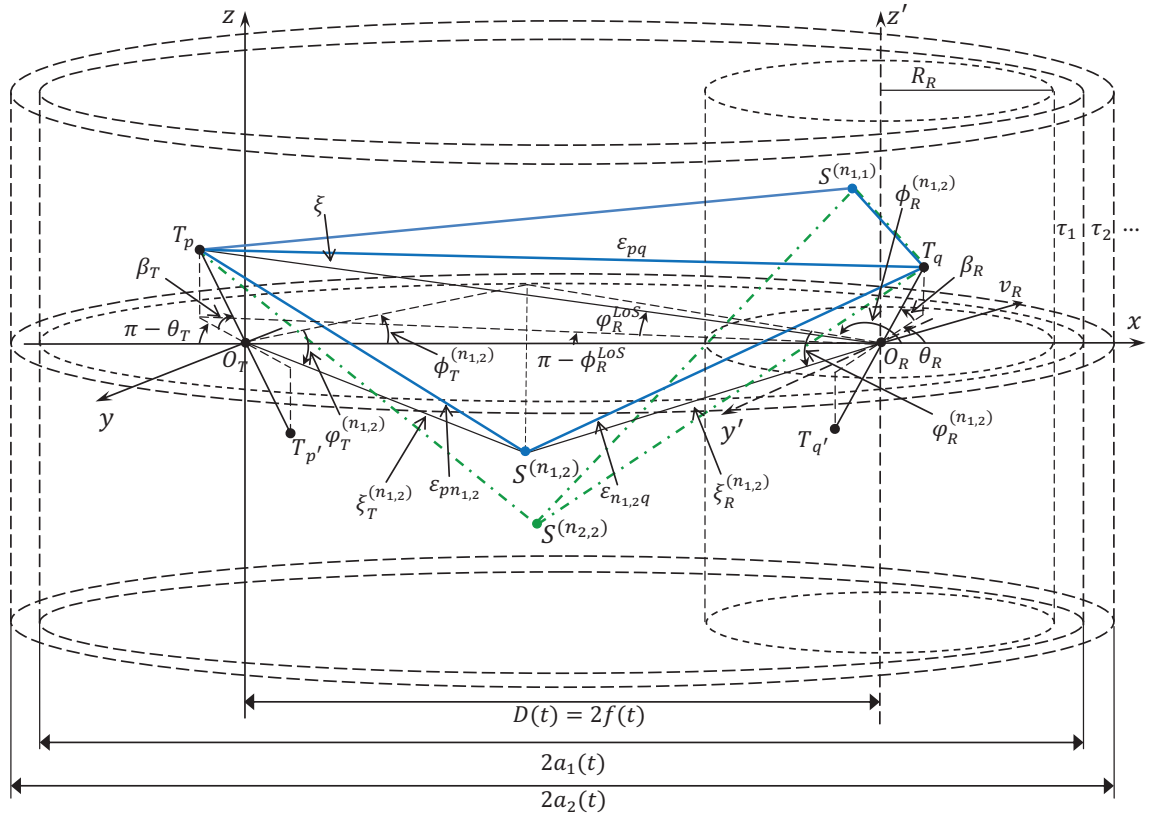


FIGURE 5.2: The proposed 3D Generic RS-GBSM combining circular-cylinder and multiple confocal elliptic-cylinder models with LoS, single-bounced rays for a wideband MIMO HST channel (Blue solid line: tap 1; Green dash-dot line: tap 2).

depict the rest of the scatterers in the environment. For better readability purposes,

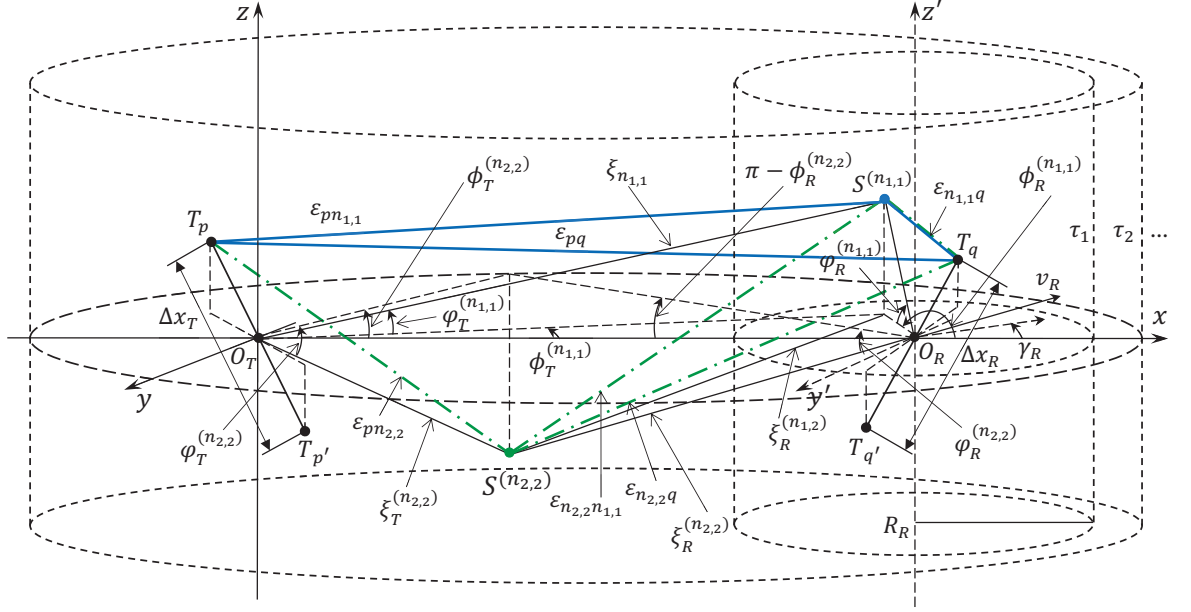


FIGURE 5.3: The detailed geometry of the single-bounced rays in the circular-cylinder and the second tap elliptic-cylinder model (Blue solid line: tap 1; Green dash-dot line: tap 2).

Fig. 5.2 only shows the geometry of LoS components and the single-bounced multiple confocal elliptic-cylinder models. The detailed geometry of the single-bounced circular-cylinder model is given in Fig. 5.3. According to the TDL concept, the complex impulse response between the p th ($p = 1, \dots, U$) antenna of Tx (i.e., T_p) and the q th ($q = 1, \dots, S$) antenna of Rx (i.e., T_q) can be expressed as

$$h_{pq}(t, \tau) = \sum_{i=1}^{I(t)} h_{i,pq}(t) \delta(\tau - \tau_i) \quad (5.1)$$

where the subscript i is the tap number and $I(t)$ is the total number of taps. $h_{i,pq}(t)$ and τ_i denote the complex time-variant tap coefficients and the discrete propagation delay of the i th tap, respectively. Hence, $h_{i,pq}(t)$ is a narrowband process.

5.2.1.1 First tap

In Fig. 5.2, we used uniform linear antenna arrays with $U = S = 2$ as an example. The circular-cylinder model defines the distribution of effective scatterers around the Rx. For the first tap, we suppose that there are $N_{1,1}$ effective scatterers around the

TABLE 5.1: Definition of parameters in Figs. 5.2 and 5.3.

$D(t)$	distance between the two foci of the elliptic-cylinder, i.e., the BS and the MRS
R_R	radius of the circular-cylinder around the MRS
$a_i(t), f(t)$	semi-major axis and half spacing between two foci of the elliptic-cylinder, respectively
$\Delta x_T, \Delta x_R$	antenna element spacing at the BS and MRS, respectively
θ_T, θ_R	orientation of the BS and MRS antenna array in the x - y plane, respectively
β_T, β_R	elevation of the BS and MRS antenna array relative to the x - y plane, respectively
v_R, γ_R	velocity and moving direction of the MRS in the x - y plane, respectively
$\phi_T^{(n_{i,m})} (m = 1, 2)$ $(i = 1, 2, \dots, I(t))$	AAoD of the waves that impinge on the effective scatterers $s^{(n_{i,m})}$
$\phi_R^{(n_{i,m})} (m = 1, 2)$ $(i = 1, 2, \dots, I(t))$	AAoA of the waves travelling from the effective scatterers $s^{(n_{i,m})}$
$\varphi_T^{(n_{i,m})} (m = 1, 2)$ $(i = 1, 2, \dots, I(t))$	E AoD of the waves that impinge on the effective scatterers $s^{(n_{i,m})}$
$\varphi_R^{(n_{i,m})} (m = 1, 2)$ $(i = 1, 2, \dots, I(t))$	E AoA of the waves travelling from the effective scatterers $s^{(n_{i,m})}$
$\phi_R^{LoS}, \varphi_R^{LoS}$	AAoA and E AoA of the LoS paths, respectively
$\varepsilon_{pq}, \varepsilon_{pn_{i,m}}, \varepsilon_{n_{i,m}q},$ $\xi, \xi_{T(R)}^{n_{i,2}}, \xi_{n_{i,1}},$ $(m = 1, 2)$ $(i = 1, 2, \dots, I(t))$	distances $d(T_p, T_q), d(T_p, s^{(n_{i,m})}), d(s^{(n_{i,m})}, T_q), d(T_p, O_R),$ $d(O_T(O_R), s^{(n_{i,2})}), d(O_T, s^{(n_{i,1})}),$ respectively

Rx lying on a sphere of radius R_R and the $n_{1,1}$ th ($n_{1,1} = 1, \dots, N_{1,1}$) effective scatterer is denoted by $s^{(n_{1,1})}$.

The multiple confocal elliptic-cylinder models with the Tx and Rx located at the foci represents the TDL structure and have $N_{i,2}$ effective scatterers on the i th elliptic-cylinder (i.e., i th tap), where $i = 1, 2, \dots, I(t)$ with $I(t)$ being the time-varying total number of elliptic-cylinders or taps. The semi-major axis of the i th elliptic-cylinder and the $n_{i,2}$ th ($n_{i,2} = 1, \dots, N_{i,2}$) effective scatterer are denoted by a_i and $s^{(n_{i,2})}$, respectively. The distance between the Tx and Rx is $D = 2f$ with f denoting the half length of the distance between the two focal points of ellipses. The antenna element spacings at the Tx and Rx are designated by Δx_T and Δx_R , respectively. The parameters in Figs. 5.2 and 5.3 are defined in Table 5.1. Note that the reasonable assumptions $D \gg R_R$ and $\min\{R_R, a - f\} \gg \max\{\Delta x_T, \Delta x_R\}$ are applied in this theoretical model [132].

From the above 3D RS-GBSM, the complex tap coefficient for the first tap of the $T_p \rightarrow T_q$ link is a superposition of the LoS and single-bounced components, and can

be expressed as

$$h_{1,pq}(t) = h_{1,pq}^{LoS}(t) + \sum_{m=1}^M h_{1,pq}^{SB_m}(t) \quad (5.2)$$

with

$$h_{1,pq}^{LoS}(t) = \sqrt{\frac{K_{pq}}{K_{pq} + 1}} e^{-j2\pi f_c \tau_{pq}(t)} e^{j2\pi f_{\max} t \cos(\phi_R^{LoS} - \gamma_R) \cos \varphi_R^{LoS}} \quad (5.3a)$$

$$h_{1,pq}^{SB_m}(t) = \sqrt{\frac{\eta_{SB_{1,m}}}{K_{pq} + 1}} \lim_{N_{1,m} \rightarrow \infty} \sum_{n_{1,m}=1}^{N_{1,m}} \frac{1}{\sqrt{N_{1,m}}} e^{j(\psi_{n_{1,m}} - 2\pi f_c \tau_{pq,n_{1,m}}(t))} \times e^{j2\pi f_{\max} t \cos(\phi_R^{(n_{1,m})} - \gamma_R) \cos \varphi_R^{(n_{1,m})}} \quad (5.3b)$$

where $\tau_{pq}(t) = \varepsilon_{pq}(t)/c$ and $\tau_{pq,n_{1,m}}(t) = (\varepsilon_{pn_{1,m}}(t) + \varepsilon_{n_{1,m}q}(t))/c$ are the travel times of the waves through the link $T_p \rightarrow T_q$ and $T_p \rightarrow s^{(n_{1,m})} \rightarrow T_q$, respectively, as shown in Figs. 5.2 and 5.3. There are two SB components in the first tap, i.e., $M=2$. The c and K_{pq} designate the speed of light and the Ricean factor, respectively. Energy-related parameters $\eta_{SB_{1,m}}$ specify how much each of the SB rays contribute to the total scattered power of the first tap. Note that these energy-related parameters are normalised to satisfy $\sum_{m=1}^M \eta_{SB_{1,m}} = 1$.

5.2.1.2 Other taps

The complex tap coefficient for other taps ($i > 1$) of the $T_p \rightarrow T_q$ link is a sum of the SB components, and can be expressed as

$$h_{i,pq}(t) = h_{i,pq}^{SB_2}(t) = \sqrt{\eta_{SB_{i,2}}} \lim_{N_{i,2} \rightarrow \infty} \sum_{n_{i,2}=1}^{N_{i,2}} \frac{1}{\sqrt{N_{i,2}}} e^{j(\psi_{n_{i,2}} - 2\pi f_c \tau_{pq,n_{i,2}}(t))} e^{j2\pi f_{\max} t \cos(\phi_R^{(n_{i,2})} - \gamma_R) \cos \varphi_R^{(n_{i,2})}} \quad (5.4)$$

where $\tau_{pq,n_{i,2}} = (\varepsilon_{pn_{i,2}} + \varepsilon_{n_{i,2}q})/c$ is the travel time of the waves through the link $T_p \rightarrow s^{(n_{i,2})} \rightarrow T_q$ as illustrated in Figs. 5.2 and 5.3. Again, energy-related parameter $\eta_{SB_{i,2}}$ specify how much the SB rays contribute to the total scattered power of other taps and it satisfies $\eta_{SB_{i,2}} = 1$. The phases $\psi_{n_{1,m}}$ and $\psi_{n_{i,2}}$ are i.i.d. random variables with uniform distributions over $[-\pi, \pi)$ and f_{\max} is the maximum Doppler frequency with respect to the MRS.

In summary, for the first tap, the SB rays are generated from the scatterers located on either the circular-cylinder or the first elliptic-cylinder. Note that only the first tap contains the LoS components, a circular-cylinder model with SB rays, and multiple confocal elliptic-cylinder models with SB rays, as shown in Figs. 5.2 and 5.3. For other taps, we assume that the SB rays are generated only from the scatterers located on the corresponding elliptic-cylinder as illustrated in Fig. 5.3.

From Figs. 5.2 and 5.3, based on the application of the law of cosines in triangles and the following assumptions $\min\{R_R, a - f\} \gg \max\{\Delta x_T, \Delta x_R\}$ and $D \gg R_R$, and using the approximation $\sqrt{1+x} \approx 1+x/2$ for small x and based on the law of cosines in appropriate triangles and small angle approximations (i.e., $\sin x \approx x$ and $\cos x \approx 1$ for small x), we have

$$\varepsilon_{pq} \approx \xi - \frac{\Delta x_R}{2\xi} \left[\frac{\Delta x_T}{2} \sin \beta_T \sin \beta_R - Q \cos \beta_R \cos \theta_R \right] \quad (5.5a)$$

$$\varepsilon_{pn_{1,1}} \approx \xi_{n_{1,1}} - \frac{\Delta x_T}{2\xi_{n_{1,1}}} \left[R_R \sin \varphi_R^{(n_{1,1})} \sin \beta_T + Q_{n_{1,1}} \cos \beta_T \cos(\phi_T^{(n_{1,1})} - \theta_T) \right] \quad (5.5b)$$

$$\varepsilon_{n_{1,1}q} \approx R_R - \frac{\Delta x_R}{2} \left[\sin \varphi_R^{(n_{1,1})} \sin \beta_R + \cos \varphi_R^{(n_{1,1})} \cos \beta_R \cos(\theta_R - \phi_R^{(n_{1,1})}) \right] \quad (5.5c)$$

$$\varepsilon_{pn_{1,2}} \approx \xi_T^{(n_{1,2})} - \frac{\Delta x_T}{2\xi_T^{(n_{1,2})}} \left[\xi_R^{(n_{1,2})} \sin \varphi_R^{(n_{1,2})} \sin \beta_T + Q_{n_{1,2}} \cos \beta_T \cos(\phi_T^{(n_{1,2})} - \theta_T) \right] \quad (5.5d)$$

$$\varepsilon_{n_{1,2}q} \approx \xi_R^{(n_{1,2})} - \Delta x_R \left[\sin \varphi_R^{(n_{1,2})} \sin \beta_R + \cos \varphi_R^{(n_{1,2})} \cos \beta_R \cos(\phi_R^{(n_{1,2})} - \theta_R) \right] \quad (5.5e)$$

$$\varepsilon_{pn_{i,2}} \approx \xi_T^{(n_{i,2})} - \frac{\Delta x_T}{2\xi_T^{(n_{i,2})}} \left[\xi_R^{(n_{i,2})} \sin \varphi_R^{(n_{i,2})} \sin \beta_T + Q_{n_{i,2}} \cos \beta_T \cos(\phi_T^{(n_{i,2})} - \theta_T) \right] \quad (5.5f)$$

$$\varepsilon_{n_{i,2q}} \approx \xi_R^{(n_{i,2})} - \Delta x_R \left[\sin \varphi_R^{(n_{i,2})} \sin \beta_R + \cos \varphi_R^{(n_{i,2})} \cos \beta_R \cos(\phi_R^{(n_{i,2})} - \theta_R) \right] \quad (5.5g)$$

where $\xi \approx Q \approx D - \frac{\Delta x_T}{2} \cos \beta_T \cos \theta_T$, $\xi_{n_{1,1}} = \sqrt{Q_{n_{1,1}}^2 + R_R^2 \sin^2 \varphi_R^{(n_{1,1})}}$, $\xi_R^{(n_{1,2})} = \frac{2a_1 - Q_{n_{1,2}}}{\cos \varphi_R^{(n_{1,2})}}$, $\xi_T^{(n_{1,2})} = \sqrt{Q_{n_{1,2}}^2 + (\xi_R^{(n_{1,2})})^2 \sin^2 \varphi_R^{(n_{1,2})}}$, $Q_{n_{1,1}} \approx D + R_R \cos \varphi_R^{(n_{1,1})} \cos \phi_R^{(n_{1,1})}$, $Q_{n_{1,2}} = \frac{a_1^2 + f^2 + 2a_1 f \cos \phi_R^{(n_{1,2})}}{a_1 + f \cos \phi_R^{(n_{1,2})}}$, $\xi_T^{(n_{i,2})} = \frac{a_i^2 + f^2 + 2a_i f \cos \phi_R^{(n_{i,2})}}{a_i + f \cos \phi_R^{(n_{i,2})}}$, and $\xi_R^{(n_{i,2})} = \frac{b_i^2}{a_i + f \cos \phi_R^{(n_{i,2})}}$ with b_i denoting the semi-minor axis of the i th elliptic-cylinder. Note that the Azimuth AoD (AAoD)/Elevation AoD (EAoD), (i.e., $\phi_T^{(n_{i,m})}$, $\varphi_T^{(n_{i,m})}$), and Azimuth AoA (AAoA)/Elevation AoA (EAoA), (i.e., $\phi_R^{(n_{i,m})}$, $\varphi_R^{(n_{i,m})}$), are correlated for SB rays. We can derive the relationship between the AoDs and AoAs of the SB rays resulting from the circular-cylinder model as $\phi_T^{(n_{1,1})} \approx \frac{R_R}{D} \sin \phi_R^{(n_{1,1})}$, $\varphi_T^{(n_{1,1})} \approx \arccos \left(\frac{D + R_R \cos \varphi_R^{(1,1)} \cos \phi_R^{(1,1)}}{\xi_{n_{1,1}}} \right)$. For the SB rays resulting from elliptic-cylinder model, the angular relationship $\phi_T^{(n_{i,2})} = \arcsin \left(\frac{b_i^2 \sin \phi_R^{(n_{i,2})}}{a_i^2 + f^2 + 2a_i f \cos \phi_R^{(n_{i,2})}} \right)$ and $\varphi_T^{(n_{i,2})} = \arccos \left[\frac{a_i^2 + f^2 + 2a_i f \cos \phi_R^{(n_{i,2})}}{(a_i + f \cos \phi_R^{(n_{i,2})}) \xi_T^{(n_{i,2})}} \right]$ hold with $b_i = \sqrt{a_i^2 - f^2}$ denoting the semi-minor axis of the i th elliptic-cylinder.

For the proposed theoretical 3D RS-GBSM, as the number of scatterers tends to infinity, the discrete AAoD $\phi_T^{(n_{i,m})}$, EAoD $\varphi_T^{(n_{i,m})}$, AAoA $\phi_R^{(n_{i,m})}$, and EAoA $\varphi_R^{(n_{i,m})}$ can be replaced by continuous random variables $\phi_T^{(i,m)}$, $\varphi_T^{(i,m)}$, $\phi_R^{(i,m)}$, and $\beta_R^{(i,m)}$, respectively. To jointly consider the impact of the azimuth and elevation angles on channel statistics, again, we use the von Mises-Fisher (VMF) Probability Density Function (PDF) to characterise the distribution of effective scatterers, which has been defined in [148]

$$f(\phi, \varphi) = \frac{k \cos \varphi}{4\pi \sinh k} \times e^{k[\cos \varphi_0 \cos \varphi \cos(\phi - \phi_0) + \sin \varphi_0 \sin \varphi]} \quad (5.6)$$

where $\phi, \varphi \in [-\pi, \pi)$, $\phi_0 \in [-\pi, \pi)$ and $\varphi_0 \in [-\pi, \pi)$ account for the mean values of the azimuth angle ϕ and elevation angle φ , respectively, and k ($k \geq 0$) is a real-valued parameter that controls the concentration of the distribution identified by the mean direction ϕ_0 and φ_0 . In this Chapter, for the angular descriptions, i.e., the AAoA $\phi_R^{(1,1)}$

and EAoA $\varphi_R^{(1,1)}$ for the circular-cylinder, and the AAoA $\phi_R^{(i,2)}$ and EAoA $\varphi_R^{(i,2)}$ for multiple elliptic cylinders, the parameters $(\phi_0, \varphi_0, \text{ and } k)$ of the VMF PDF in (5.6) can be replaced by $(\phi_{R0}^{(i,1)}, \varphi_{R0}^{(i,1)}, \text{ and } k^{(i,1)})$, and $(\phi_{R0}^{(i,2)}, \varphi_{R0}^{(i,2)}, \text{ and } k^{(i,2)})$, respectively.

5.2.2 Time-varying Channel Parameters

Here, we will introduce the time-varying parameters of the proposed non-stationary channel model.

5.2.2.1 The total number of taps

In a time-variant (i.e., non-stationary) scenario, taps may only exist over a certain time period. With ongoing time, new taps appear, i.e., born, and remain for a certain time span, i.e., survive, and then finally disappear, i.e., died. A suitable description for such a generation-recombination behaviour is given by discrete Markov processes. The time variance of HST wireless channel is mainly caused by the movement of the MS or the MRS in relay-supported network architecture. A genetic appearance (birth) and disappearance (death) process for modelling the taps, i.e., clusters or Multi-Path Component (MPC), was proposed in [149]. An NGSM based on finite-state Markov chains for HST wireless communication channels was proposed in [99]. The proposed model is able to capture the characteristics of time-varying HST wireless channel by using Markov chain to track the channel state variation at different time intervals. Authors of [101] have followed similar approach to model the dynamic evolution of MPCs, i.e., birth-death process, using four-state Markov chain model. The transition matrix of the birth-death process was calculated based on the measurement presented in [59].

Based on the process of taps' generation and recombination, the time dependent channel fluctuations caused by the movement of the MRS ($\delta_{MRS,k}$) in the time span

between t_{k-1} and t_k , can be expressed as

$$\delta_{P,k} = \delta_{MRS,k} = \int_{t_{k-1}}^{t_k} (|\vec{v}_R(t)|) dt \quad (5.7)$$

Because of the short time steps, a uniform motion in each time interval $|t_k - t_{k-1}|$ is assumed [149], [150]. This simplifies (5.7) to

$$\delta_{P,k} = |\vec{v}_R(t_k) - \vec{v}_R(t_{k-1})| = (t_k - t_{k-1})v_R. \quad (5.8)$$

Therefore, $\delta_{P,k}$ gives a measure for the correlation of Channel Impulse Response (CIR) at different time snapshots. A Markov birth-death description results in a time-varying number $I(t)$ of taps for CIR realisations. At any time instant t_k , one can distinguish between newly generated taps and survived taps that were already existing in the previous CIR at time instant t_{k-1} . The Markov process is described by a generation rate of taps (λ_G) and a recombination rate of new taps (λ_R). The expectation of the total number, also defined as the initial number, of taps in a CIR realisation is given by

$$\mathbf{E} \{I(t)\} = I(t_0) = \frac{\lambda_G}{\lambda_R}. \quad (5.9)$$

Observing a time series of CIRs, each tap remains from one CIR at t_{k-1} to a following one at t_k with the probability

$$P_{\text{remain}}(\delta_{P,k}) = e^{-\lambda_R \cdot \delta_{P,k}}. \quad (5.10)$$

Hence, a number of new taps is generated by the Markov process with expectation

$$\mathbf{E} \{I_{\text{new},k}\} = \frac{\lambda_G}{\lambda_R} (1 - e^{-\lambda_R \cdot \delta_{P,k}}). \quad (5.11)$$

The correlation between two evolving clusters is quantified by the scenario movement $\delta_{P,k}$. Mathematically, higher values of $\delta_{P,k}$ result in a reduced correlation between the

properties of an ancestor cluster at t_{k-1} and its successor at t_k . Fig. 5.4 shows the time-varying number of clusters $I(t)$ using the parameters reported in [59].

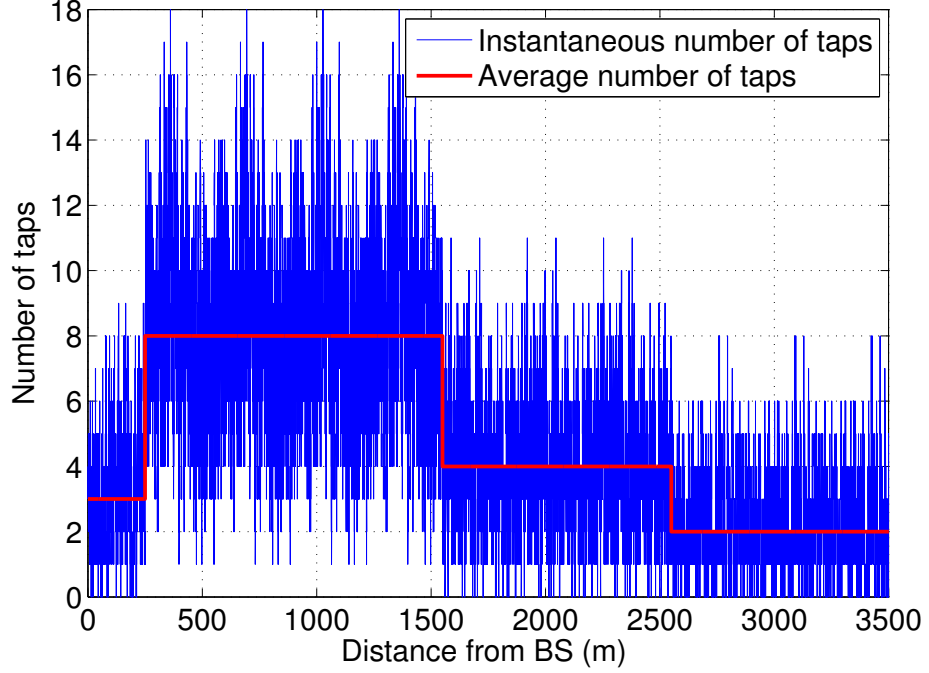


FIGURE 5.4: The total number of taps $I(t)$ as a function of distance from BS.

5.2.2.2 Time-varying distance between BS and MRS

Similar to what we have introduced in Chapter 3, the distance between the BS and MRS will change over the time and due to the high speed of the MRS, the impact of this change on the channel characteristics cannot be ignored.

5.2.2.3 Time-varying AoDs and AoAs

Based on the geometrical relationship in the model, the time-varying AoDs and AoAs can be derived as follows.

a) In the case of the LoS components, time-varying AAoA ($\phi_R^{LoS}(t)$), and EAoA ($\varphi_R^{LoS}(t)$) can be expressed as

$$\phi_R^{LoS}(t) = \begin{cases} \phi_R^{LoS}(t_0) + \arccos\left(\frac{D_s(t_0) + v_R t \cos \gamma_R}{D(t)}\right), & -\pi \leq \gamma_R \leq 0 \\ \phi_R^{LoS}(t_0) - \arccos\left(\frac{D(t_0) + v_R t \cos \gamma_R}{D(t)}\right), & 0 \leq \gamma_R \leq \pi \end{cases} \quad (5.12a)$$

where $\phi_R^{LoS}(t_0) = \arcsin\left(\frac{k_p \Delta x_T}{D(t_0)} \sin \beta_T\right)$ denotes the initial LoS AAoA at time $t = t_0$.

b) In the case of the SB components $SB_{1,1}$ resulting from Rx circular-elliptic, the time-varying AAoD ($\phi_T^{(n_{1,1})}(t)$), EAoD ($\varphi_T^{(n_{1,1})}(t)$), AAoA ($\phi_R^{(n_{1,1})}(t)$), and EAoA ($\varphi_R^{(n_{1,1})}(t)$) can be expressed as

$$\phi_T^{(n_{1,1})}(t) \approx \phi_T^{(n_{1,1})} \quad (5.13a)$$

$$\varphi_T^{(n_{1,1})}(t) \approx \varphi_T^{(n_{1,1})} \quad (5.13b)$$

$$\phi_R^{(n_{1,1})}(t) \approx \phi_R^{(n_{1,1})} \quad (5.13c)$$

$$\varphi_R^{(n_{1,1})}(t) \approx \varphi_R^{(n_{1,1})}. \quad (5.13d)$$

This is basically because the effective scatterers on the Rx circular-elliptic represent the static and uniformly distributed scatterers around the HST, e.g., the slopes of the cutting and the structure of the viaduct.

c) In the case of the SB components $SB_{i,2}$ for the i th tap resulting from the elliptic-cylinder, time-varying AAoA ($\phi_R^{(n_{i,2})}(t)$) and EAoA ($\varphi_R^{(n_{i,2})}(t)$) can be expressed as

$$\phi_R^{(n_{i,2})}(t) = \pi - \arccos \frac{v_R t - \xi_R^{(n_{i,2})} \cos \alpha_R^{(n_{i,2})}}{\sqrt{\xi_R^{(n_{i,2})2} + (v_R t)^2 - 2\xi_R^{(n_{i,2})} v_R t \cos \alpha_R^{(n_{i,2})}}} \quad (5.14a)$$

$$\varphi_R^{(n_{i,2})}(t) = \arctan \frac{\xi_R^{(n_{i,2})} \tan \beta_R^{(n_{i,2})}}{\sqrt{\xi_R^{(n_{i,2})^2} + (v_R t)^2 - 2\xi_R^{(n_{i,2})} v_R t \cos \phi_R^{(n_{i,2})}}}. \quad (5.14b)$$

Note that the time-varying AAoD ($\phi_T^{(n_{i,2})}(t)$) and EAoD ($\varphi_T^{(n_{i,2})}(t)$), are correlated with time-varying AAoA ($\phi_R^{(n_{i,2})}(t)$) and EAoA ($\varphi_R^{(n_{i,2})}(t)$) for SB rays resulting from the elliptic-cylinder model. Hence, the relationship between the AoD and AoA for multiple confocal elliptic-cylinder models can be given by

$$\phi_T^{(n_{i,2})}(t) = \arcsin \frac{b(t)^2 \sin \phi_R^{(n_{i,2})}(t)}{a(t)^2 + f(t)^2 + 2a(t)f(t) \cos \phi_R^{(n_{i,2})}(t)} \quad (5.15a)$$

$$\varphi_T^{(n_{i,2})}(t) = \arccos \frac{a(t)^2 + f(t)^2 + 2a(t)f(t) \cos \phi_R^{(n_{i,2})}(t)}{\left(a(t) + f(t) \cos \phi_R^{(n_{i,2})}(t)\right) \xi_T^{(n_{i,2})}(t)}. \quad (5.15b)$$

5.2.2.4 Time-varying Ricean K-factor

To calculate the time-varying distance-dependant Ricean K -factor in the proposed 3D theoretical model, we will use the formulas reported in the literature and presented in Chapter 4 in (4.8) and (4.9).

5.2.3 Statistical Properties of the Proposed 3D Wideband Non-stationary MIMO HST Channel Model

5.2.3.1 Time-variant ST CF

The non-stationary correlation properties of two arbitrary CIRs $h_{pq}(t, \Delta t)$ and $h_{p'q'}(t, \Delta t)$ of a MIMO HST channel can be expressed as

$$R_h(t, \Delta x_T, \Delta x_R, \Delta t) = \sum_{i=1}^{I(t)} R_{h_i}(t, \Delta x_T, \Delta x_R, \Delta t). \quad (5.16)$$

where $R_{h_i}(t, \Delta x_T, \Delta x_R, \Delta t)$ is the time-variant ST CF of the i -th tap that can be expressed as

$$R_{h_i}(t, \Delta x_T, \Delta x_R, \Delta t) = E \{ h_{i,pq}(t) h_{i,p'q'}^*(t - \Delta t) \}. \quad (5.17)$$

Since the LoS, SB components are independent to each other, based on (5.2) we have the following time-variant ST CF for the first tap ($i=1$)

$$R_{h_1}(t, \Delta x_T, \Delta x_R, \Delta t) = R_h^{\text{LoS}}(t, \Delta x_T, \Delta x_R, \Delta t) + \sum_{m=1}^M R_{h_1}^{\text{SB}_m}(t, \Delta x_T, \Delta x_R, \Delta t) \quad (5.18)$$

and $R_{h_i}(t, \Delta x_T, \Delta x_R, \Delta t) = R_{h_i}^{\text{SB}_2}(t, \Delta x_T, \Delta x_R, \Delta t)$ for other taps ($1 < i \leq I$).

– In the case of the LoS component,

$$R_h^{\text{LoS}}(t, \Delta x_T, \Delta x_R, \Delta t) = K' e^{\frac{j2\pi}{\lambda} A^{\text{LoS}}(t)} e^{-j2\pi \Delta t (-f_{\max} \cos \gamma_R)}, \quad (5.19)$$

where $A^{\text{LoS}}(t) = 2D(t) \cos \beta_R \cos \theta_R$ and $K' = \sqrt{\frac{K_{pq} K_{p'q'}}{(K_{pq}+1)(K_{p'q'}+1)}}$.

– In the case of the SB components $SB_{1,1}$ for the first tap resulting from the Rx circular-cylinder,

$$R_{h_1}^{\text{SB}_1}(t, \Delta x_T, \Delta x_R, \Delta t) = \eta_{SB_{1,1}} \int_{-\pi}^{\pi} \int_{-\pi}^{\pi} e^{\frac{j2\pi}{\lambda} A^{(1,1)}(t)} e^{j2\pi \Delta t f_{\max} B^{(1,1)}(t)} \times f(\phi_R^{(1,1)}, \varphi_R^{(1,1)}) d(\phi_R^{(1,1)}, \varphi_R^{(1,1)}), \quad (5.20)$$

where $A^{(1,1)} = \Delta x_R \left[\sin \varphi_R^{(1,1)} \sin \beta_R + \cos \varphi_R^{(1,1)} \cos \beta_R \cos \left(\theta_R - \phi_R^{(1,1)} \right) \right] + \frac{\Delta x_T}{\xi_{n_{1,1}}} \left[R_R \sin \varphi_R^{(1,1)} \times \sin \beta_T + Q_{n_{1,1}} \cos \beta_T \cos \left(\theta_T - \phi_T^{(1,1)} \right) \right]$ and $B^{(1,1)} = \cos \left(\phi_R^{(1,1)} - \gamma_R \right) \cos \left(\varphi_R^{(1,1)} \right)$.

– In the case of the SB components $SB_{i,2}$ for the i th tap resulting from the i th elliptical-cylinder,

$$R_{h_i}^{\text{SB}_2}(t, \Delta x_T, \Delta x_R, \Delta t) = \eta_{SB_{i,2}} \int_{-\pi}^{\pi} \int_{-\pi}^{\pi} e^{-\frac{j2\pi}{\lambda} A^{(i,2)}(t)} e^{j2\pi \Delta t f_{\max} B^{(i,2)}(t)} \times f(\phi_R^{(i,2)}, \varphi_R^{(i,2)}) d(\phi_R^{(i,2)}, \varphi_R^{(i,2)}), \quad (5.21)$$

with $A^{(i,2)} = \frac{\Delta x_T}{\xi_T^{(n_{i,2})}} \left[\xi_R^{(n_{i,2})} \sin \varphi_R^{(i,2)} \sin \beta_T + Q_{n_{i,2}} \cos \beta_T \cos \left(\theta_T - \phi_T^{(i,2)} \right) \right] + \Delta x_R \left[\sin \varphi_R^{(i,2)} \times \sin \beta_R + \cos \varphi_R^{(i,2)} \cos \beta_R \cos \left(\theta_R - \phi_R^{(i,2)} \right) \right]$ and $B^{(i,2)} = \cos \left(\phi_R^{(i,2)} - \gamma_R \right) \cos \left(\varphi_R^{(i,2)} \right)$.

5.2.3.2 Time-variant ACF

The time-variant ACF can be obtained by imposing $\Delta x_T = 0$ and $\Delta x_R = 0$ in (5.16), i.e.,

$$r_h(t, \Delta t) = \sum_{i=1}^{I(t)} r_{h_i}(t, \Delta t) = \sum_{i=1}^{I(t)} \mathbb{E} \{ h_{i,pq}(t) h_{i,pq}^*(t - \Delta t) \}. \quad (5.22)$$

– In the case of the LoS component,

$$r_h^{\text{LoS}}(t, \Delta t) = K e^{\frac{j2\pi}{\lambda} A^{\text{LoS}}(t)} e^{-j2\pi \Delta t (-f_{\max} \cos \gamma_R)}, \quad (5.23)$$

where $K = \frac{K_{pq}}{(K_{pq}+1)}$.

– In the case of the SB components $SB_{1,1}$ for the first tap resulting from the Rx circular-cylinder,

$$r_{h_1}^{\text{SB}_1}(t, \Delta t) = \eta_{SB_{1,1}} \int_{-\pi}^{\pi} \int_{-\pi}^{\pi} e^{j2\pi \Delta t f_{\max} B^{(1,1)}} f(\phi_R^{(1,1)}, \varphi_R^{(1,1)}) d(\phi_R^{(1,1)}, \varphi_R^{(1,1)}). \quad (5.24)$$

– In the case of the SB components $SB_{i,2}$ for the i th tap resulting from the i th elliptical-cylinder,

$$r_{h_i}^{\text{SB}_2}(t, \Delta t) = \eta_{SB_{i,2}} \int_{-\pi}^{\pi} \int_{-\pi}^{\pi} e^{j2\pi \Delta t f_{\max} B^{(i,2)}} f(\phi_R^{(i,2)}, \varphi_R^{(i,2)}) d(\phi_R^{(i,2)}, \varphi_R^{(i,2)}). \quad (5.25)$$

5.2.3.3 Time-variant space CCF

By imposing $\Delta t = 0$ in (5.16), we can get the time-variant space CCF between two arbitrary channel coefficients as

$$\rho_h(t, \Delta x_T, \Delta x_R) = \sum_{i=1}^{I(t)} \rho_{h_i}(t, \Delta x_T, \Delta x_R) = \sum_{i=1}^{I(t)} \mathbb{E} \{ h_{i,pq}(t) h_{i,p'q'}^*(t) \}. \quad (5.26)$$

– In the case of the LoS component,

$$\rho_h^{\text{LoS}}(t, \Delta x_T, \Delta x_R) = K' e^{\frac{j2\pi}{\lambda} A^{\text{LoS}}(t)} e^{-j2\pi \Delta t (-f_{\max} \cos \gamma_R)}. \quad (5.27)$$

– In the case of the SB components $SB_{1,1}$ for the first tap resulting from the Rx circular-cylinder,

$$\rho_{h_1}^{\text{SB}_1}(t, \Delta x_T, \Delta x_R) = \eta_{SB_{1,1}} \int_{-\pi}^{\pi} \int_{-\pi}^{\pi} e^{\frac{j2\pi}{\lambda} A^{(1,1)}} f(\phi_R^{(1,1)}, \varphi_R^{(1,1)}) d(\phi_R^{(1,1)}, \varphi_R^{(1,1)}). \quad (5.28)$$

– In the case of the SB components $SB_{i,2}$ for the i th tap resulting from the i th elliptical-cylinder,

$$\rho_{h_i}^{\text{SB}_2}(t, \Delta x_T, \Delta x_R) = \eta_{SB_{i,2}} \int_{-\pi}^{\pi} \int_{-\pi}^{\pi} e^{-\frac{j2\pi}{\lambda} A^{(i,2)}} f(\phi_R^{(i,2)}, \varphi_R^{(i,2)}) d(\phi_R^{(i,2)}, \varphi_R^{(i,2)}). \quad (5.29)$$

5.3 3D Non-stationary Wideband Simulation Model for MIMO HST Channels

5.3.1 Description of the 3D Wideband MIMO Simulation Model

Based on the proposed 3D theoretical GBSM described in Section 5.2, the corresponding simulation model can be further developed by using finite numbers of scatterers $N_{i,1}$ and $N_{i,2}$. Based on (5.1), the complex tap coefficient for the link $T_p \rightarrow T_q$ for the simulation model can be expressed as

$$\tilde{h}_{pq}(t, \tau) = \sum_{i=1}^{I(t)} \tilde{h}_{i,pq}(t) \delta(\tau - \tau_i) \quad (5.30)$$

where the complex tap coefficient of the first tap can be expressed as

$$\tilde{h}_{1,pq}(t) = \tilde{h}_{1,pq}^{\text{LoS}}(t) + \sum_{m=1}^M \tilde{h}_{1,pq}^{\text{SB}_m}(t), \quad (5.31)$$

and the one for the other taps can be expressed as

$$\tilde{h}_{i,pq}(t) = \tilde{h}_{i,pq}^{SB_2}(t). \quad (5.32)$$

In (5.31) and (5.32), the LoS component, the SB components of the first tap, and the SB components of the other taps can be respectively expressed as

$$\tilde{h}_{1,pq}^{LoS}(t) = \sqrt{\frac{K_{pq}}{K_{pq} + 1}} e^{-j2\pi f_c \tau_{pq}(t)} e^{j2\pi f_{\max} t \cos(\phi_R^{LoS} - \gamma_R) \cos \varphi_R^{LoS}} \quad (5.33a)$$

$$\begin{aligned} \tilde{h}_{1,pq}^{SB_m}(t) = & \sqrt{\frac{\eta_{SB_{1,m}}}{K_{pq} + 1}} \sum_{n_{1,m}=1}^{N_{1,m}} \frac{1}{\sqrt{N_{1,m}}} e^{j(\psi_{n_{1,m}} - 2\pi f_c \tau_{pq,n_{1,m}}(t))} \\ & \times e^{j2\pi f_{\max} t \cos(\phi_R^{(n_{1,m})} - \gamma_R) \cos \varphi_R^{(n_{1,m})}} \end{aligned} \quad (5.33b)$$

$$\tilde{h}_{i,pq}^{SB_2}(t) = \sqrt{\eta_{SB_{i,2}}} \sum_{n_{i,2}=1}^{N_{i,2}} \frac{1}{\sqrt{N_{i,2}}} e^{j(\psi_{n_{i,2}} - 2\pi f_c \tau_{pq,n_{i,2}})} e^{j2\pi f_{\max} t \cos(\phi_R^{(n_{i,2})} - \gamma_R) \cos \varphi_R^{(n_{i,2})}} \quad (5.33c)$$

By comparing the simulation and the theoretical models, we only need to determine the discrete AoDs and AoAs for the simulation model by using the Method of Equal Volume (MEV) [151]. The idea of MEV is to calculate the set of $\{\phi^{(n_{i,m})}, \varphi^{(n_{i,m})}\}_{n_{i,m}=1}^{N_{i,m}}$ in such a manner that the volume of the VMF PDF $f(\phi, \varphi)$ in different ranges of $\{\phi^{(n_{i,m}-1)}, \varphi^{(n_{i,m}-1)}\} \leq \{\phi, \varphi\} < \{\phi^{(n_{i,m})}, \varphi^{(n_{i,m})}\}$ are equal to each other with the initial condition, i.e.,

$$\int_{-\pi}^{\phi^{(i,m)}} \int_{-\pi}^{\varphi^{(i,m)}} f(\phi, \varphi) d\phi d\varphi = \frac{1 - 1/4}{N_{i,m}}, \quad (5.34)$$

where $f(\phi, \varphi)$ is the 3D VMF PDF introduced in (5.6).

5.3.2 Statistical Properties of The 3D Simulation Model

Based on the proposed generic 3D MIMO HST theoretical GBSM and its statistical properties, the corresponding statistical properties for the simulation model can be derived using discrete angle parameters. As the detailed derivations have been explained in Section. 5.2 for the theoretical model, those of the corresponding simulation model with similar derivations are only briefly explained here. Applying the discrete model parameters to (5.16)–(5.25), we have the corresponding statistical properties for the simulation model as follows

5.3.2.1 Time-variant ST CF

The time-variant ST CF of the proposed 3D simulation model can be expressed as

$$\tilde{R}_h(t, \Delta x_T, \Delta x_R, \Delta t) = \sum_{i=1}^{I(t)} \tilde{R}_{h_i}(t, \Delta x_T, \Delta x_R, \Delta t). \quad (5.35)$$

where $R_{h_i}(t, \Delta x_T, \Delta x_R, \Delta t)$ is the time-variant ST CF of the i -th tap that can be expressed as

$$\tilde{R}_{h_i}(t, \Delta x_T, \Delta x_R, \Delta t) = E \left\{ \tilde{h}_{i,pq}(t) \tilde{h}_{i,p'q'}^*(t - \Delta t) \right\}. \quad (5.36)$$

Similar to the theoretical model, we have the following time-variant ST CF for the first tap ($i=1$) of the simulation model

$$\tilde{R}_{h_1}(t, \Delta x_T, \Delta x_R, \Delta t) = \tilde{R}_h^{\text{LoS}}(t, \Delta x_T, \Delta x_R, \Delta t) + \sum_{m=1}^M \tilde{R}_{h_1}^{\text{SB}_m}(t, \Delta x_T, \Delta x_R, \Delta t) \quad (5.37)$$

and $\tilde{R}_{h_i}(t, \Delta x_T, \Delta x_R, \Delta t) = \tilde{R}_{h_i}^{\text{SB}_2}(t, \Delta x_T, \Delta x_R, \Delta t)$ for other taps ($1 < i \leq I$).

– In the case of the LoS component,

$$\tilde{R}_h^{\text{LoS}}(t, \Delta x_T, \Delta x_R, \Delta t) = K' e^{\frac{j2\pi}{\lambda} A^{\text{LoS}}(t)} e^{j2\pi \Delta t f_{\max} \cos(\tilde{\phi}_R^{\text{LoS}}(t - \Delta t) - \gamma_R)}, \quad (5.38)$$

- In the case of the SB components $SB_{1,1}$ for the first tap resulting from the Rx circular-cylinder,

$$\tilde{R}_{h_1}^{SB_1}(t, \Delta x_T, \Delta x_R, \Delta t) = \frac{\eta_{SB_{1,1}}}{N_{1,1}} \sum_{n_{1,1}=1}^{N_{1,1}} e^{\frac{j2\pi}{\lambda} \tilde{A}^{(1,1)}} e^{j2\pi \Delta t f_{\max} \tilde{B}^{(1,1)}}, \quad (5.39)$$

where $\tilde{A}^{(1,1)} = \Delta x_R \left[\sin \tilde{\varphi}_R^{(1,1)} \sin \beta_R + \cos \tilde{\varphi}_R^{(1,1)} \cos \beta_R \cos \left(\theta_R - \tilde{\phi}_R^{(1,1)} \right) \right] + \frac{\Delta x_T}{\xi_{n_{1,1}}} \left[R_R \sin \tilde{\varphi}_R^{(1,1)} \times \sin \beta_T + Q_{n_{1,1}} \cos \beta_T \cos \left(\theta_T - \tilde{\phi}_T^{(1,1)} \right) \right]$ and $\tilde{B}^{(1,1)} = \cos \left(\tilde{\phi}_R^{(1,1)} - \gamma_R \right) \cos \left(\tilde{\varphi}_R^{(1,1)} \right)$.

- In the case of the SB components $SB_{i,2}$ for the i th tap resulting from the i th elliptical-cylinder,

$$\tilde{R}_{h_i}^{SB_2}(t, \Delta x_T, \Delta x_R, \Delta t) = \frac{\eta_{SB_{i,2}}}{N_{i,2}} \sum_{n_{i,2}=1}^{N_{i,2}} e^{-\frac{j2\pi}{\lambda} \tilde{A}^{(i,2)}} e^{j2\pi \Delta t f_{\max} \tilde{B}^{(i,2)}}, \quad (5.40)$$

with $\tilde{A}^{(i,2)} = \frac{\Delta x_T}{\xi_T^{(n_{i,2})}} \left[\xi_R^{(n_{i,2})} \sin \tilde{\varphi}_R^{(i,2)} \sin \beta_T + Q_{n_{i,2}} \cos \beta_T \cos \left(\theta_T - \tilde{\phi}_T^{(i,2)} \right) \right] + \Delta x_R \left[\sin \tilde{\varphi}_R^{(i,2)} \times \sin \beta_R + \cos \tilde{\varphi}_R^{(i,2)} \cos \beta_R \cos \left(\theta_R - \tilde{\phi}_R^{(i,2)} \right) \right]$ and $\tilde{B}^{(i,2)} = \cos \left(\tilde{\phi}_R^{(i,2)} - \gamma_R \right) \cos \left(\tilde{\varphi}_R^{(i,2)} \right)$.

5.3.2.2 Time-variant ACF

The time-variant ACF can be obtained by imposing $\Delta x_T = 0$ and $\Delta x_R = 0$ in (5.35)

$$\tilde{r}_h(t, \Delta t) = \sum_{i=1}^{I(t)} \tilde{r}_{h_i}(t, \Delta t) = \sum_{i=1}^{I(t)} \mathbb{E} \left\{ \tilde{h}_{i,pq}(t) \tilde{h}_{i,pq}^*(t - \Delta t) \right\}. \quad (5.41)$$

- In the case of the LoS component,

$$\tilde{r}_h^{\text{LoS}}(t, \Delta t) = K e^{\frac{j2\pi}{\lambda} \tilde{A}^{\text{LoS}}(t)} e^{j2\pi \Delta t f_{\max} \cos(\tilde{\phi}_R^{\text{LoS}}(t - \Delta t) - \gamma_R)}. \quad (5.42)$$

- In the case of the SB components $SB_{1,1}$ for the first tap resulting from the Rx circular-cylinder,

$$\tilde{r}_{h_1}^{SB_1}(t, \Delta t) = \frac{\eta_{SB_{1,1}}}{N_{1,1}} \sum_{n_{1,1}=1}^{N_{1,1}} e^{j2\pi \Delta t f_{\max} \tilde{B}^{(1,1)}}. \quad (5.43)$$

- In the case of the SB components $SB_{i,2}$ for the i th tap resulting from the i th elliptical-cylinder,

$$\tilde{r}_{h_i}^{\text{SB}_2}(t, \Delta t) = \frac{\eta_{SB_{i,2}}}{N_{i,2}} \sum_{n_{i,2}=1}^{N_{i,2}} e^{j2\pi\Delta t f_{\max} \tilde{B}^{(i,2)}}. \quad (5.44)$$

5.3.2.3 Time-variant space CCF

By imposing $\Delta t = 0$ in (5.35), we can get the time-variant space CCF of the 3D simulation model as

$$\tilde{\rho}_h(t, \Delta x_T, \Delta x_R) = \sum_{i=1}^{I(t)} \tilde{\rho}_{h_i}(t, \Delta x_T, \Delta x_R) = \sum_{i=1}^{I(t)} \text{E} \left\{ \tilde{h}_{i,pq}(t) \tilde{h}_{i,p'q'}^*(t) \right\}. \quad (5.45)$$

- In the case of the LoS component,

$$\tilde{\rho}_h^{\text{LoS}}(t, \Delta x_T, \Delta x_R) = K' e^{\frac{j2\pi}{\lambda} A^{\text{LoS}}(t)}. \quad (5.46)$$

- In the case of the SB components $SB_{1,1}$ for the first tap resulting from the Rx circular-cylinder,

$$\tilde{\rho}_{h_1}^{\text{SB}_1}(t, \Delta x_T, \Delta x_R) = \frac{\eta_{SB_{1,1}}}{N_{1,1}} \sum_{n_{1,1}=1}^{N_{1,1}} e^{\frac{j2\pi}{\lambda} \tilde{A}^{(1,1)}}. \quad (5.47)$$

- In the case of the SB components $SB_{i,2}$ for the i th tap resulting from the i th elliptical-cylinder,

$$\tilde{\rho}_{h_i}^{\text{SB}_2}(t, \Delta x_T, \Delta x_R) = \frac{\eta_{SB_{i,2}}}{N_{i,2}} \sum_{n_{i,2}=1}^{N_{i,2}} e^{-\frac{j2\pi}{\lambda} \tilde{A}^{(i,2)}}. \quad (5.48)$$

5.4 Results and Analysis

In this section, the statistical properties of the proposed theoretical and simulation models are evaluated and analysed. Moreover, we compare between the statistical properties of the 3D models with the 2D simulation one to investigate the impact of

the elevation angle on channel statistics. The 2D simulation model, which will be a one-ring and multiple ellipses model, can be obtained from the 3D one by setting the elevation angles $\beta_R^{(n1)}$ and $\beta_R^{(n2)}$ to 0° . Finally, the proposed 3D simulation channel model is validated by measurements. The parameters for our analysis for each HST scenario are listed here or specified otherwise. For all the scenarios, $v_R = 250$ km/h, $f_c = 2.6$ GHz, and thus $f_{\max} = 600$ Hz, $N_{1,1} = N_{i,2} = 40$, $\beta_R = \beta_T = 45^\circ$, $\theta_T = \theta_R = 45^\circ$, $\phi_{R0}^{(1)} = 25^\circ$, $\varphi_{R0}^{(1)} = 10^\circ$, $\alpha_{R0}^{(2)} = 85^\circ$, and $\beta_{R0}^{(2)} = 15^\circ$. For open space scenario: the LoS Ricean factor $K_{pq} = K_{p'q'} = 6$, $D_s(t_0) = 1000$ m, $R_R = 50$ m, $D_{\min} = 50$ m as in [15], and $\gamma_R = 0^\circ$. The environment-related parameters $k^{(i,1)}$, and $k^{(i,2)}$ are related to the distribution of scatterers, i.e., the smaller values of $k^{(i,1)}$ and $k^{(i,2)}$ the denser scatterers in the surrounding environment. In open space scenario, the scatterers are sparse and randomly distributed at different distances from the railway track [152], therefore we have $k^{(1,1)} = 2$ and $k^{(i,2)} = 6$ and the power-related parameters for the open space scenario are $\eta_{SB_{1,1}} = 0.4$ and $\eta_{SB_{1,2}} = 0.6$ for the first tap. The parameters for viaduct scenario, obtained from the measurement campaign in [63], are: $L = 15$ m, $H_{\text{viad}} = 20$ m, $H_{\text{BS}} = 44$ m, $H_{\text{MRS}} = 30$ cm, $H_{\text{train}} = 3.8$ m, cellular radius = 2502 m, therefore, $D_s(t) \in [0, 2502)$ m, $D_{BP} = 400$ m, $R_R = 15$ m, and $\gamma_R = 0$. In viaduct scenario, the relatively high altitude of the BS antenna leads to fewer reflected and scattered components with reduced power of the NLoS components at the receiver compared with that in the open space scenario [7]. Here, we have the power-related parameters as $\eta_{SB_{1,1}} = 0.3$ and $\eta_{SB_{1,2}} = 0.6$ and environment-related parameters as $k^{(1,1)} = 1.5$ and $k^{(i,2)} = 11.5$. The simulation parameters, obtained from the measurement campaign reported in [71], are: $L = 15$ m, $H_{\text{cut}} = 7.1$ m, $H_{\text{BS}} = 28$ m, $H_{\text{MRS}} = 30$ cm, $H_{\text{train}} = 3.8$ m, $W_{\text{up}} = 53.93$ m, $W_{\text{down}} = 17.78$ m, and therefore $R_R = \frac{W_{\text{up}} + W_{\text{down}}}{2} = 38$ m, cellular radius = 1410 m, therefore, $D_s(t) \in [0, 1410)$ m, $D_{BP} = 200$ m, and $\gamma_R = 0$. As we mentioned before, an important characteristic of the cuttings scenario is the rich reflection and scattering components caused by the slopes of the cutting on both sides of the railway track. Since this rich effective scatterers are modelled here using the circular-cylinder, we have the power-related parameters as $\eta_{SB_{1,1}} = 0.75$ and $\eta_{SB_{1,2}} = 0.25$ and environment-related parameters as $k^{(1,1)} = 0.5$ and $k^{(i,2)} = 15$.

5.4.1 Time-variant ACF

By using (5.22)–(5.25) and (5.41)–(5.44), Figs. 5.5(a), (b), and (c) shows the absolute values of the time-variant ACF of the 3D theoretical model, 3D simulation model, 3D simulation result, and 2D simulation model in open space, viaduct, and cutting scenarios, respectively. Fig. 5.5 shows that the 3D simulation model closely approximates the 3D theoretical one and matches well with the 3D simulation results, indicating the correctness of our derivations and simulations. From this figure, it can be easily noticed the high value of the correlation in the three studied HST scenarios due to the dominant LoS component. This agrees with the observation in [7]. Fig. 5.5 also

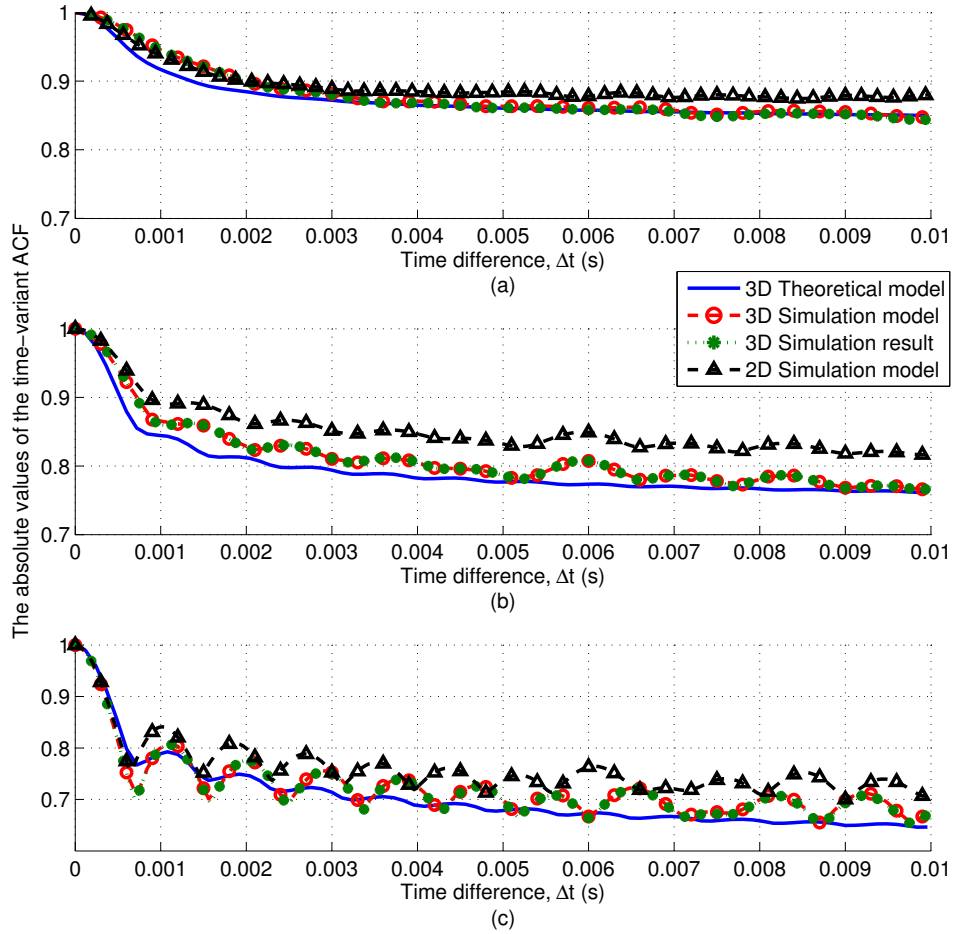


FIGURE 5.5: The absolute values of the time-variant ACF of the 3D theoretical model, the 3D simulation model, the 3D simulation result, and the 2D simulation model in (a) open space scenario, (b) viaduct scenario, and (c) cutting scenario.

shows that 2D simulation model overestimates the temporal ACF in the three aforementioned scenarios which suggests that the 2D model underestimates the spatial diversity gain.

Fig.5.6 shows the absolute values of the time-variant ACF of the 3D theoretical model, the 3D simulation model, and the 3D simulation result in cutting scenario at two different time instants, i.e., $t = 0$ s and $t = 2$ s. Due to the time-variant channel parameters of the proposed 3D generic models, the absolute values of the ACFs vary with time which agrees with observations reported in real HST measurements [71].

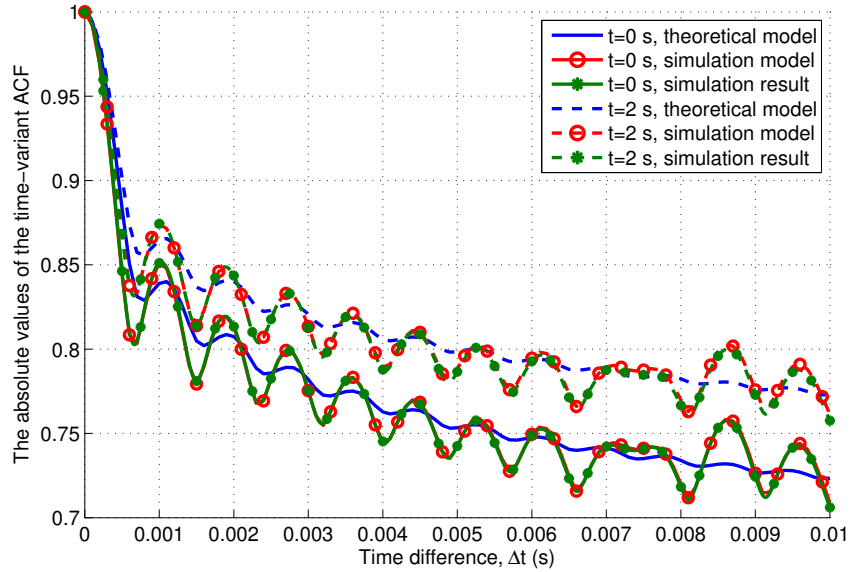


FIGURE 5.6: The absolute values of the time-variant ACF of the proposed 3D theoretical model, the proposed 3D simulation model, and the corresponding 3D simulation result in cutting scenario at different time instants.

5.4.2 Time-variant space CCF

By adopting a BS antenna element spacing $\Delta x_T = \lambda$, the absolute values of the time-variant of the space CCFs of the 3D theoretical model, 3D simulation model, 3D simulation result, and 2D simulation model in open space, viaduct, and cutting scenarios are illustrated in Figs. 5.7(a), (b), and (c), respectively. Similar to the conclusions reached for the time-variant ACF, the dominant LoS component that can

be observed at the Rx in the three different HST scenarios results in a high correlation. Moreover, as the 2D simulation model cannot capture the spatial diversity at the vertical plane, it overestimates the spatial correlation compared with the 3D models as Fig. 5.7 shows. This agrees with the conclusion withdrawn in [153] that compares between 3D and 2D ITU channel models using ray-tracing. The comparison has also showed that 3D modelling implies lower spatial correlation values compared to the 2D model that only considers the azimuth plane in modelling the channel. Accurate observation of the correlation properties leads to better estimation of the MIMO performance.

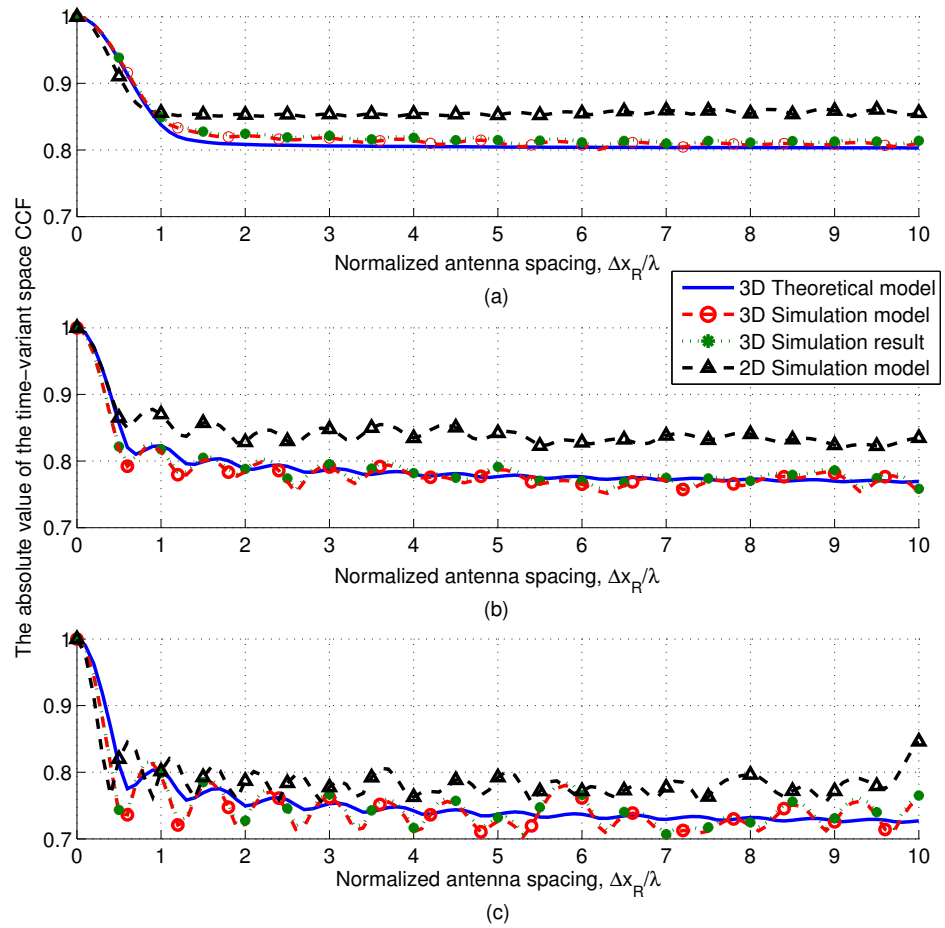


FIGURE 5.7: The absolute values of the time-variant space CCF of the 3D theoretical model, the 3D simulation model, the 3D simulation result, and the 2D simulation model in (a) open space scenario, (b) viaduct scenario, and (c) cutting scenario.

5.4.3 Stationary Interval

To verify the utility of the proposed 3D simulation model, we compare the stationary interval of our 3D HST SoS simulation model and that of the measured HST channel reported in [77] using the same formula as (4.52). It worth mentioning that the measurement in [77] has been carried out under a GSM-R system and therefore our simulation parameters, obtained from the measurement data, are: $f_c = 930$ MHz, $v_R = 324$ km/h, $N_{PDP} = 15$, $c_{\text{thresh}} = 0.8$. As Fig. 5.8 illustrates, the excellent agreement between the CCDFs of stationary intervals for our proposed 3D HST simulation model and the measurement data demonstrates the utility of our HST channel models. Moreover, the stationary interval of the 2D simulation model with the time-variant angular parameters proposed in Chapter 4 is also presented to show the improvement that is achieved by introducing the 3D model with all time-variant parameters.

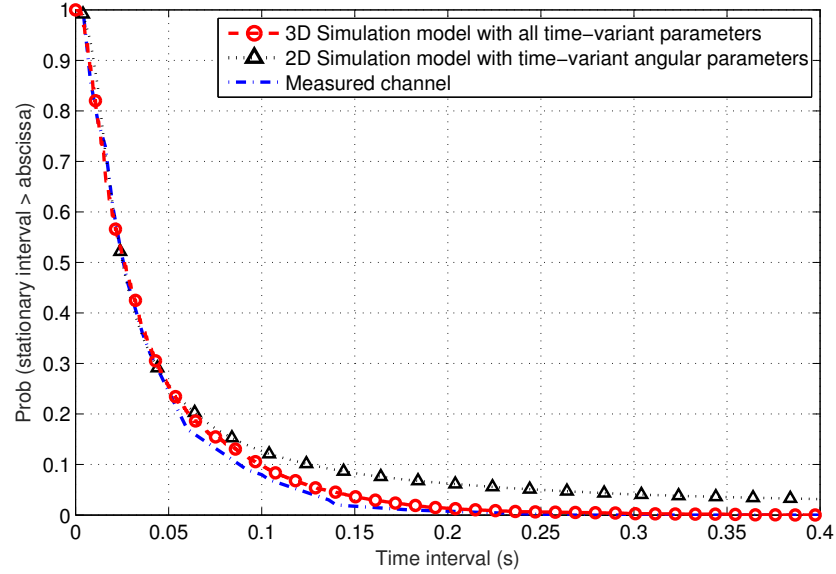


FIGURE 5.8: The empirical CCDFs of stationary intervals for the proposed 3D HST simulation model, the 2D HST simulation model, and a measured HST channel.

5.5 Summary

In this Chapter, we have proposed a novel generic 3D wideband theoretical GBSM and the corresponding simulation model for non-stationary MIMO HST fading channels. The proposed models are sufficiently generic to be applied on different HST scenario by choosing proper values of a set of scenario-specific parameters. Moreover, the proposed 3D models have the ability to investigate the impact of the elevation angle on channel statistics and mimic the non-stationarity nature of HST channels. Birth and death process of the MPC are utilised to describe the non-stationarity of HST channels along with other time-variant parameters such as the angular parameters and the Ricean K -factor. Based on the proposed models, some statistical properties have been derived and investigated in the three most common HST scenarios, namely, the open space, the viaduct, and the cutting scenarios. The proposed 3D theoretical and simulation models have been verified by simulated results which suggests the correctness of our derivations and simulations. Moreover, the proposed 3D simulation model has been verified by measurement data in terms of stationary interval. The numerical and simulation results have shown that the spatial correlation between multi-antennas elements is high due to the dependance on the dominant LoS component at the Rx side. The impact of the elevation angle on the channel statistics has been investigated by comparing the statistical properties of the proposed 3D models with 2D ones. The comparison showed that 2D models tends to overestimate the correlation properties of the channel.

Chapter 6

A Non-Stationary IMT-Advanced MIMO Channel Model for High-Mobility Wireless Communication Systems

6.1 Introduction

MIMO has attracted a lot of attention in the last decade as a promising technique that can enhance the system performance and link reliability. Wireless channel modelling plays an important role on designing and evaluating MIMO wireless communication systems. Demonstrating the feasibility of wireless systems is not possible without accurate channel models that are able to mimic key characteristics of the wireless channels.

Many standardised MIMO channel models are available in the literature, e.g., IEEE 802.11 TGn channel model [154], LTE-A channel model [15], 3GPP/3GPP2 SCM [138], SCME [139], WINNER I [155], WINNER II [34], WINNER+ [143], and IMT-A [33] channel models. However, all the aforementioned standardised channel models have neglected the non-stationarity of the fading channels assuming that modelled channels satisfy the WSS assumption.

Practical measurement campaigns [156]–[159] have proved that the WSS assumption is only valid for short intervals considering the time variation of real wireless channels. Measurement data reported in [77] has demonstrated that the stationary interval, defined as the maximum time duration over which the channel satisfies the WSS condition, of standard channel models, like IMT-A and WINNER II, is considerably longer than that of a real HST channel. In [122], measurement of vehicle-to-vehicle (V2V) channels has proved that the stationary interval of channels between vehicles driving in opposite directions can be very short. Therefore, research of non-stationary channel modelling has gradually become a hot research topic especially for high-mobility scenarios.

Different modelling approaches have been introduced in the literature to model non-stationary channels. Non-stationary V2V and HST channel models were surveyed in [120] and [152], respectively. Non-stationary GBDMs were proposed in [160] to model V2V channels and in [90], [161] to model HST channels. GBDMs incorporate detailed simulations of the actual physical wave propagation process for a given environment. Therefore, they are physically meaningful and potentially accurate. To incorporate the non-stationarity of the communication channels, ray-tracing technique were implemented in [160], [161] while [90] adopted random propagation-graph technique. Despite their accuracy, GBDMs only consider specific propagation scenarios and require detailed descriptions of the propagation environments and extensive computational resources to be implemented. NGSMs characterise physical parameters of propagation channels in a completely stochastic manner by providing their underlying probability distribution functions without assuming an underlying geometry. In [162] and [99], the authors proposed NGSMs for non-stationary V2V and HST channels, respectively. NGSMs are convenient to characterise the death/birth properties of the Moving Cluster (MC) using Markov chains. However, the local statistical properties of the non-stationary NGSMs are difficult to derive. In GBSMs, the impulse responses of HST channels are characterised by the law of wave propagation applied to specific transmitter, receiver, and scatterers' geometries which are predefined in a stochastic fashion according to certain probability distributions. Time-variant GBSMs with time-varying parameters were proposed in [128], [129], [163] for V2V channels and

in [96], [98] for HST channels where some interesting local statistical properties were derived by taking time-varying parameters into account. However, these existing time-variant GBSMs are only modeled for some specific scenarios, such as specified moving directions for MCs and MSs [163], specified roadside conditions [128], [129], and specific environments [96], [98].

In conventional cellular wireless network, the BS is fixed while a MS is moving towards a certain direction with a constant speed. In non-stationary IMT-A channel models, we assume that the movements of MCs and MSs result in the time-variant properties. Following the trajectory of the MCs and a MS, we can obtain Small-Scale Parameters (SSP), such as the number of clusters, the mean power and delay of each cluster (PDP), AoDs, and AoAs. The lack of implementation for non-stationarity IMT-A MIMO channel models and the aforementioned research gaps inspire us to propose a non-stationary channel model with the aforementioned time-varying parameters.

We summarise the major contributions and novelties of this chapter as follows:

- (1) A non-stationary IMT-A channel model with time-varying SSPs, i.e., the number of clusters, delays, the power of each cluster, AoDs, and AoAs, is proposed.
- (2) Based on the proposed non-stationary IMT-A channel model, important statistical properties, i.e., the local spatial CCF and local temporal ACF are derived and analysed.
- (3) The stationary interval of the proposed non-stationary IMT-A channel model is investigated and compared with the one of the standard IMT-A channel model and with a measurement data.

The rest of this chapter is structured as follows. In Section 6.2, the original IMT-A MIMO channel model is briefly introduced. Section 6.3 presents the proposed novel non-stationary IMT-A channel models with various time-varying SSPs. The local statistical properties of the non-stationary IMT-A channel model with time-varying parameters are derived in Section 6.4 and then simulated and analysed in Section 6.5. Finally, the conclusions are drawn in Section 6.6.

6.2 Overview of The Original IMT-A MIMO Channel Model

For the evaluation of IMT-A systems the ITU has defined a channel model [33] that consists of PL models, scenario-specific parameter sets for the Indoor Hotspot (InH), UMa, UMi, RMa, and Suburban Macro-cell (SMa) scenarios, and a so-called generic model. The generic model specifies the mathematical model and the algorithms used for channel modelling that apply to all scenarios. It is based on the WINNER II channel model [34]. This generic model employs a GBSM approach to represent the multi-path propagation channel between a BS and MSs.

In IMT-A channel model, the channel is assumed to satisfy the WSSUS assumption which means that the channel fading statistics remain invariant over a short period of time and that the scatterers with different path delays are uncorrelated. Please note that the WSSUS assumption is only valid to describe the short-term variations of the radio channel. Based on the WSSUS assumption and the TDL concept, the original IMT-A MIMO channel model has the complex CIR between the BS antenna element s ($s=1, \dots, S$) and MS antenna element u ($u=1, \dots, U$) as [33]:

$$h_{u,s}(t, \tau) = \sum_{n=1}^N h_{u,s,n}(t) \delta(\tau - \tau_n) \quad (6.1)$$

where

$$h_{u,s,n}(t) = \sqrt{\frac{P_n}{M}} \sum_{m=1}^M e^{j d_s k \sin(\phi_{n,m})} e^{j d_u k \sin(\varphi_{n,m})} e^{j 2\pi v_{n,m} t} e^{j \Phi_{n,m}}. \quad (6.2)$$

Here, $h_{u,s,n}(t)$ ($n=1, \dots, N$) denotes a narrowband process where all the M sub-paths within each of the N clusters are irresolvable rays and have the same delay τ_n , P_n is the power of the n th cluster associated with the delay τ_n , d_s and d_u are the antenna element spacings at the BS and MS, respectively, $k = \frac{2\pi}{\lambda}$ is the wave number where λ is the carrier wavelength, $\phi_{n,m}$ and $\varphi_{n,m}$ denote the AoD and AoA related to the m th ($m = 1, \dots, M$) ray within the n th ($n = 1, \dots, N$) cluster, respectively, and the

random phases $\Phi_{n,m}$ are uniformly distributed within $[-\pi, \pi)$. The Doppler frequency component is represented by $v_{n,m} = \frac{\|\vec{v}_{MS}\| \cos(\varphi_{n,m} - \theta_{MS})}{\lambda}$, where $\|\vec{v}_{MS}\|$ and θ_{MS} denote the magnitude of the MS velocity and MS direction of travel, respectively. All of the aforementioned parameters are time-invariant because of the WSSUS assumption in the original IMT-A channel model.

6.3 A Novel Non-Stationary IMT-A Channel Model with Time-Varying Parameters

In practice, because of the observable movement of MCs and/or MSs, the WSSUS assumption may be violated and the channel model parameters will change over the time. In this case, the complex CIR of the new non-stationary IMT-A channel model with time-varying parameters can be expressed as

$$h_{u,s}(t, \tau) = \sum_{n=1}^{N(t)} h_{u,s,n}(t) \delta(\tau - \tau_n(t)) \quad (6.3)$$

where

$$h_{u,s,n}(t) = \sqrt{\frac{P_n(t)}{M}} \sum_{m=1}^M e^{jd_s k \sin(\phi_{n,m}(t))} e^{jd_u k \sin(\varphi_{n,m}(t))} e^{jk \|\vec{v}_{MS}\| \cos(\varphi_{n,m}(t) - \theta_{MS})t} e^{j\Phi_{n,m}}. \quad (6.4)$$

Due to the movement of the MSs and/or MCs, the channel model parameters $N(t)$, $\tau_n(t)$, $P_n(t)$, $\phi_{n,m}(t)$, and $\varphi_{n,m}(t)$ will change over the time and therefore they need to be represented using proper time-varying functions. Fig. 6.1 illustrates the proposed non-stationary IMT-A channel model, which is derived from the original IMT-A channel model [33]. The parameters in Fig. 6.1 are defined in Table 6.1. The propagation between the first and the last interacted cluster is not defined. Thus, this approach can also model multiple interactions with the scattering media. Note that $\phi_{n,m}(t_0)$, $\varphi_{n,m}(t_0)$, $\Delta\phi_{n,m}$, and $\Delta\varphi_{n,m}$ denote the initial mean AoD, initial mean AoA, AoD offset, and AoA offset, respectively. The subscripts n, m indicate one of the N paths and one of the M rays/sub-paths in the wideband channel, respectively. The AoD

TABLE 6.1: Definitions of channel parameters in Fig. 6.1.

Parameters	Definition
$D_{BS}(t)$	distance between the BS and MC A
$D_{MS}(t)$	distance between the MS and MC Z
$D_{LoS}(t)$	distance of the LoS components between BS and MS
$\phi_{n,m}(t), \varphi_{n,m}(t)$	the AoD and AoA related to the m th ray within the n th cluster, respectively
$\phi_{LoS}, \varphi_{LoS}$	the LoS AoD and LoS AoA , respectively
$\Delta\phi_{n,m}, \Delta\varphi_{n,m}$	the AoD offset and AoA offset, respectively
$\vec{v}_A, \vec{v}_Z, \vec{v}_{MS}$	the velocity vectors of MC A , MC Z , and MS, respectively
v_A, θ_A	the MC A velocity and direction of travel, respectively
v_Z, θ_Z	the MC Z velocity and direction of travel, respectively
v_{MS}, θ_{MS}	the MS velocity and direction of travel, respectively

relates to the first bounce/cluster, i.e., Cluster A , interacted from the BS side and AoA is from the last bounce/cluster, i.e., Cluster Z . Furthermore, ϕ_{LoS} and φ_{LoS} are the LoS components for BS and MS, respectively. In Fig. 6.1, we assume that the BS is fixed while the first cluster, Cluster A , is in motion with the direction θ_A and speed v_A . As we consider multi-bounced scattering occurring for each path, Cluster Z refers to the last bounce MC, with the moving direction θ_Z and speed v_Z . For the MS, θ_{MS} is the moving direction with the speed v_{MS} . The movement of MC A , MC Z , and MS are represented in Fig. 1 using the vectors \vec{v}_A , \vec{v}_Z , and \vec{v}_{MS} , respectively. Furthermore, $D_{BS}(t_0)$ and $D_{MS}(t_0)$, which represent the initial distance between the BS and MC A , and the initial distance between the MS and MC Z , respectively, are assumed to be known. The initial distance of the LoS components between BS and MS is donated as $D_{LoS}(t_0)$. To derive the time-varying angular parameters, we set four assistant angles, i.e., $\alpha_{n,m}(t)$, β , $\gamma_{n,m}(t)$, and δ in Fig. 6.1.

Based on the aforementioned geometric description, the channel realisations of the proposed non-stationary IMT-A channel model are obtained by the procedure illustrated in Fig. 6.2. Initial values of the model parameters, i.e., $N(t_0)$, $\tau_n(t_0)$, $P_n(t_0)$, $\phi_{n,m}(t_0)$, and $\varphi_{n,m}(t_0)$, will be calculated in a similar procedure to the one presented in the IMT-A channel model (the top section of Fig. 6.2). Here, we will focus on the non-stationary properties of the proposed IMT-A channel model (the bottom section of Fig. 6.2).

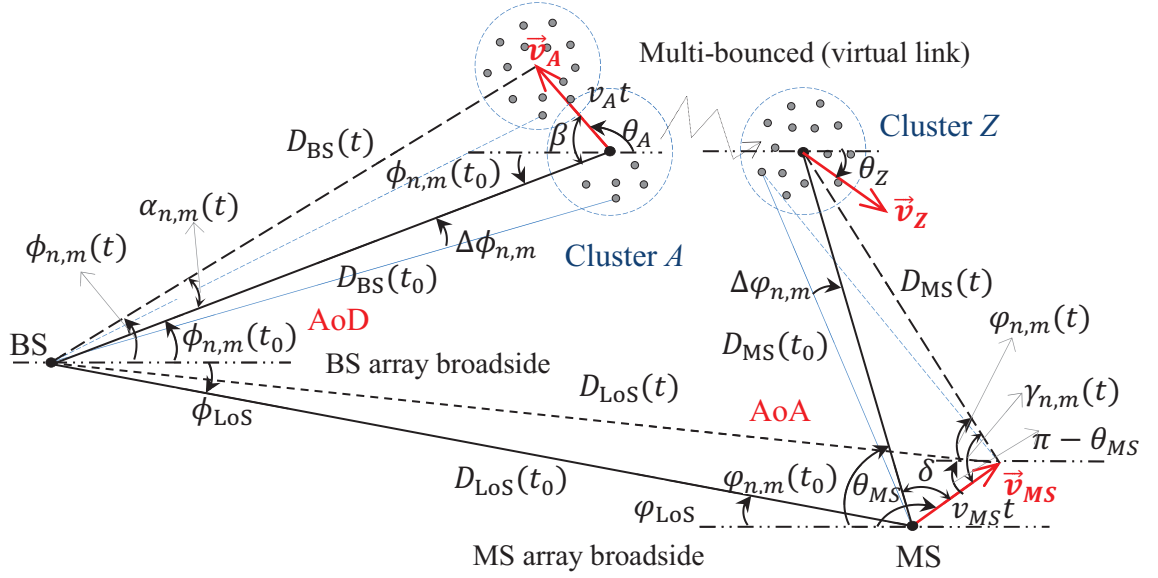


FIGURE 6.1: BS and MS angular parameters in the IMT-A channel model.

6.3.1 Update MCs and MS locations

Based on the movement direction of MC A , MC Z , and MS, the distances between BS, MCs, and MS will change with time t . By considering the concept of relative velocity MC Z and MS, we can assume that the MS is only in motion with a velocity relative to MC Z . As the velocity is a vector, which is equivalent to a specification of its speed and direction of motion, we define the velocity of MC Z as $\vec{v}_Z = v_Z \cdot e^{j\theta_Z}$ and that of MS as $\vec{v}_{MS} = v_{MS} \cdot e^{j\theta_{MS}}$.

In terms of the Newton's classical mechanics, we assume that the MC Z is fixed as a reference point, the velocity of MS relative to the MC Z can be expressed as

$$\begin{aligned}
 \vec{v}_{MS/Z} &= \vec{v}_{MS} - \vec{v}_Z \\
 &= v_{MS} \cdot e^{j\theta_{MS}} - v_Z \cdot e^{j\theta_Z} \\
 &= v_{MS} \cdot \cos \theta_{MS} + j \cdot v_{MS} \cdot \sin \theta_{MS} - v_Z \cdot \cos \theta_Z - j \cdot v_Z \cdot \sin \theta_Z \\
 &= (v_{MS} \cdot \cos \theta_{MS} - v_Z \cdot \cos \theta_Z) + j (v_{MS} \cdot \sin \theta_{MS} - v_Z \cdot \sin \theta_Z).
 \end{aligned} \tag{6.5}$$

Therefore, $v_{MS/Z}$ and $\theta_{MS/Z}$ can be calculated by taking the magnitude and argument of $\vec{v}_{MS/Z}$, i.e., $v_{MS/Z} = \|\vec{v}_{MS/Z}\|$ and $\theta_{MS/Z} = \mathbf{arg}(\vec{v}_{MS/Z})$, respectively.

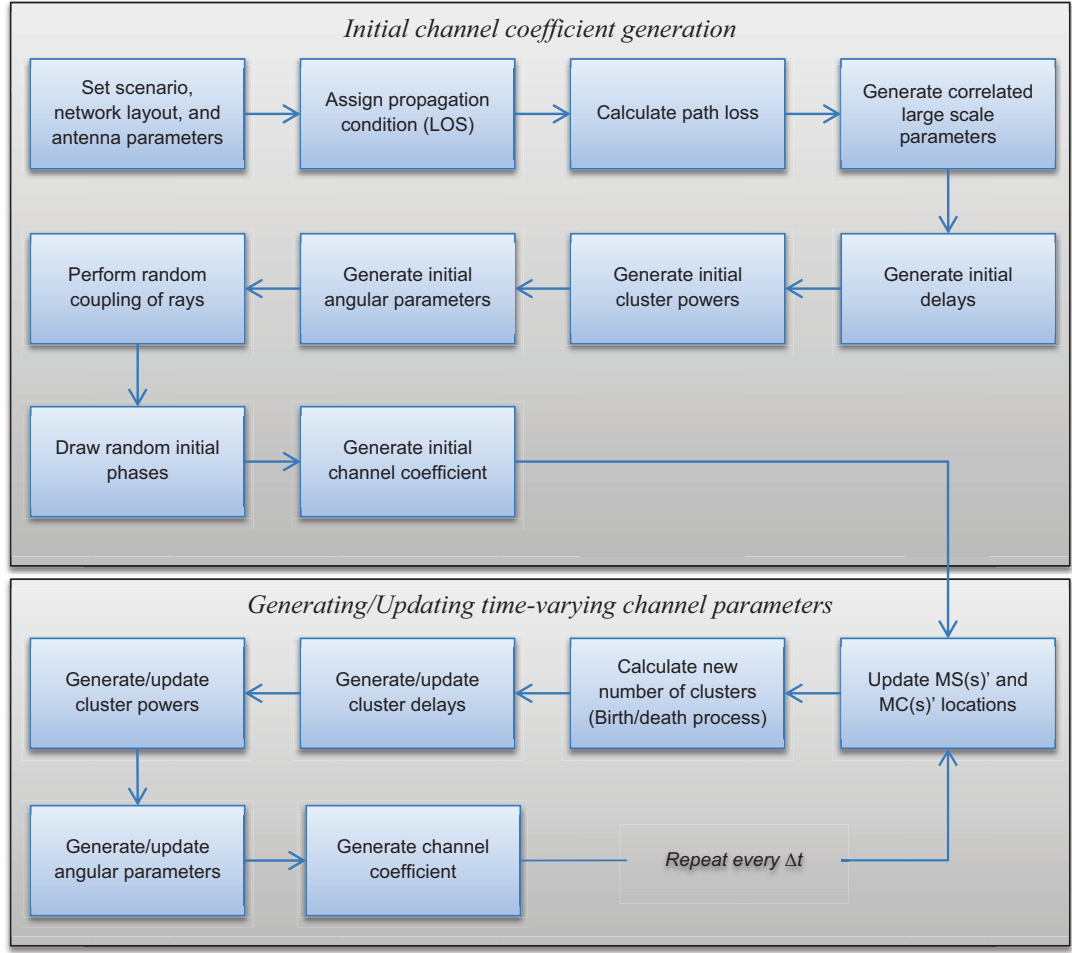


FIGURE 6.2: The non-stationary IMT-A channel coefficients generation procedure.

Assuming that the initial distances, $D_{BS}(t_0)$, $D_{MS}(t_0)$, and $D_{LoS}(t_0)$ are obtained from a measurement campaign, the time-varying distances at time t can be expressed as

$$D_{BS}(t) = \sqrt{D_{BS}^2(t_0) + (v_A t)^2 - 2 \cdot D_{BS}(t_0) \cdot v_A t \cdot \cos(\pi + \phi_{n,m}(t_0) - \theta_A)}, \quad (6.6)$$

$$D_{MS}(t) = \sqrt{D_{MS}^2(t_0) + (v t)^2 - 2 \cdot a(t_0) \cdot v t \cdot \cos(\varphi_{n,m}(t_0) - \theta_v)}, \quad (6.7)$$

$$D_{LoS}(t) = \sqrt{D_{LoS}^2(t_0) + (v_{MS} t)^2 - 2 \cdot D_{LoS}(t_0) \cdot v_{MS} t \cdot \cos(\theta_{MS} - \varphi_{LoS})}. \quad (6.8)$$

6.3.2 The number of clusters

A genetic appearance (birth) and disappearance (death) process for modeling the clusters, or MPCs, was proposed in [149]. In a time-variant (i.e., non-stationary) scenario, clusters may only exist over a certain time period. With ongoing time, new clusters appear, i.e., born, and remain for a certain time span, i.e., survive, and then finally disappear, i.e., died. A suitable description for such a generation-recombination behavior is given by discrete Markov processes. The time variance of a wireless channel is mainly caused by movements of MCs and MS. Based on the process of clusters' generation and recombination, the time dependent channel fluctuations caused by the movement of the MCs ($\delta_{MC,k}$) as well as the movement of MS ($\delta_{MS,k}$) in the time span between t_{k-1} and t_k , can be expressed as

$$\delta_{P,k} = \delta_{MC,k} + \delta_{MS,k}, \quad (6.9)$$

with

$$\delta_{MC,k} = \int_{t_{k-1}}^{t_k} P_c (|\vec{v}_Z(t)| + |\vec{v}_A(t)|) dt \quad (6.10)$$

and

$$\delta_{MS,k} = \int_{t_{k-1}}^{t_k} (|\vec{v}_{MS}(t)|) dt \quad (6.11)$$

where P_c is a percentage of moving clusters. Because of the short time steps, a uniform motion in each time interval $|t_k - t_{k-1}|$ is assumed [149], [150]. This simplifies (6.10) and (6.11) to

$$\delta_{MC,k} = (t_k - t_{k-1})P_c (v_Z + v_A), \quad (6.12)$$

$$\delta_{MS,k} = |\vec{v}_{MS}(t_k) - \vec{v}_{MS}(t_{k-1})| = (t_k - t_{k-1})v_{MS}. \quad (6.13)$$

Therefore, $\delta_{P,k}$ gives a measure for the correlation of CIR at different time snapshots. A Markov birth-death description results in a time-varying number $N(t)$ of clusters for CIR realisations. At any time instant t_k , one can distinguish between newly generated clusters and survived clusters that were already existing in the previous CIR at time instant t_{k-1} . The Markov process is described by a generation rate of clusters (λ_G) and a recombination rate of new paths (λ_R). The expectation of the total number, also defined as the initial number, of clusters in a CIR realisation is given by

$$\mathbf{E} \{N(t)\} = N(t_0) = \frac{\lambda_G}{\lambda_R}. \quad (6.14)$$

Observing a time series of CIRs, each cluster remains from one CIR at t_{k-1} to a following one at t_k with the probability

$$P_{\text{remain}}(\delta_{P,k}) = e^{-\lambda_R \cdot \delta_{P,k}}. \quad (6.15)$$

Hence, a number of new clusters is generated by the Markov process with expectation

$$\mathbf{E} \{N_{\text{new},k}\} = \frac{\lambda_G}{\lambda_R} (1 - e^{-\lambda_R \cdot \delta_{P,k}}). \quad (6.16)$$

The correlation between two evolving clusters is quantified by the scenario movement $\delta_{P,k}$. Mathematically, higher values of $\delta_{P,k}$ result in a reduced correlation between the properties of an ancestor cluster at t_{k-1} and its successor at t_k . Fig. 6.3 illustrates the time-variation of the number of clusters with birth-death process at the initial number of clusters $N(t_0) = 20$ taken from IMT-A channel models at NLoS UMa scenario assuming $\lambda_G = 0.8/\text{m}$, $\lambda_R = 0.04/\text{m}$, $v_{MS} = 60 \text{ m/s}$, $v_A = 15 \text{ m/s}$, $v_Z = 5 \text{ m/s}$, and $P_c = 0.3$. In Fig. 6.3, starting from the initial status ($N(t_0) = 20$), clusters are appear/disappear with the time going. In addition, Fig. 6.4 shows the time-varying number of clusters $N(t)$.

For the newly generated clusters, the delays, powers, and angular parameters will be generated similar to the initial parameters based on the procedure illustrated in

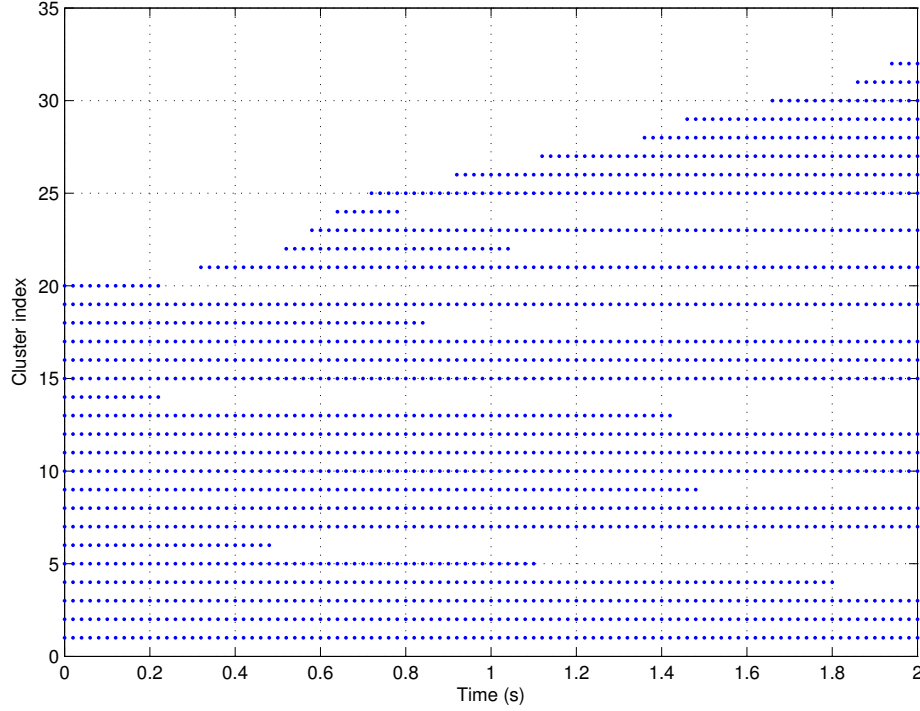


FIGURE 6.3: Time-varying clusters with death/birth process. ($N(t_0) = 20$, $\lambda_G = 0.8/\text{m}$, $\lambda_R = 0.04/\text{m}$, $v_{MS} = 60\text{ m/s}$, $v_A = 15\text{ m/s}$, $v_Z = 5\text{ m/s}$, and $P_c = 0.3$)

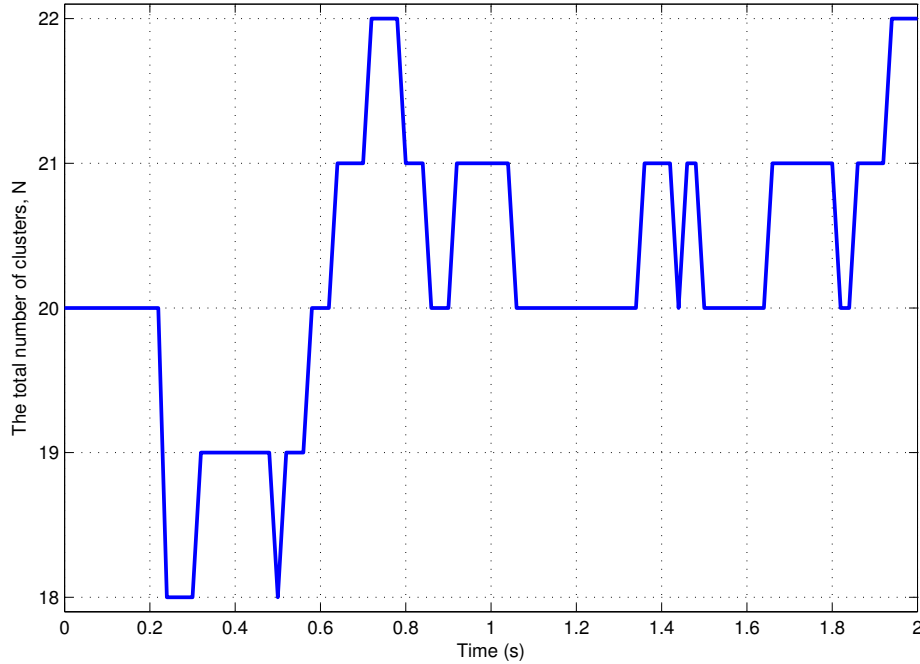


FIGURE 6.4: The total number of clusters $N(t)$ vs. time. ($N(t_0) = 20$, $\lambda_G = 0.8/\text{m}$, $\lambda_R = 0.04/\text{m}$, $v_{MS} = 60\text{ m/s}$, $v_A = 15\text{ m/s}$, $v_Z = 5\text{ m/s}$, and $P_c = 0.3$)

Fig. 6.2 and explained in [33]. For the surviving clusters, the delays, powers, and

angular parameters will be updated as follows.

6.3.3 Time-varying delays

With the movements of MCs (including MC A and MC Z) and MS, the propagation distance of the n th cluster will be time-variant and can be determined by using some trigonometric functions on the basis of the initial distance of the n th cluster as (6.6)–(6.8). The calculation of the time-varying delay $\tau_n(t)$ can be expressed as follows:

$$\begin{aligned}\tau_n(t) &= \frac{\Delta D}{c_0} + \tilde{\tau}_n(t) = \frac{\Delta D_{\text{BS}} + \Delta D_{\text{MS}}}{c_0} + \tilde{\tau}_n(t) \\ &= \frac{(D_{\text{BS}}(t) - D_{\text{BS}}(t_0)) + (D_{\text{MS}}(t) - D_{\text{MS}}(t_0))}{c_0} + \tilde{\tau}_n(t)\end{aligned}\quad (6.17)$$

where c_0 is the speed of light, $\Delta D = \Delta D_{\text{BS}} + \Delta D_{\text{MS}}$ is the alteration of the propagation distance resulted from the movement of the MS and MCs. $\Delta D_{\text{BS}} = D_{\text{BS}}(t) - D_{\text{BS}}(t_0)$ is the distance difference between BS and MC A , $\Delta D_{\text{MS}} = D_{\text{MS}}(t) - D_{\text{MS}}(t_0)$ is the distance difference between MC Z and MS, and $\tilde{\tau}_n(t)$ is the delay of the virtual link between MC A and MC Z . The delay of the virtual link, i.e., $\tilde{\tau}_n$, can be calculated at time instant $t = t_k$ using a first-order filtering algorithm as [164]

$$\tilde{\tau}_n(t_k) = e^{((t_{k-1}-t_k)/\varsigma)} \tilde{\tau}_n(t_{k-1}) + (1 - e^{((t_{k-1}-t_k)/\varsigma)}) X \quad (6.18)$$

where $X \sim U(D_{\text{LoS}}/c_0, \tau_{\text{max}})$, ς is a parameter that depends on the coherence of a virtual link and scenarios, and τ_{max} is the maximum delay and can be obtained from [33], e.g., $\tau_{\text{max}} = 1885$ ns for UMa NLoS scenario.

It is worth to be noted that $\tilde{\tau}_n(t_0)$ can be calculated as

$$\tilde{\tau}_n(t_0) = \tau_n(t_0) - \frac{D_{\text{BS}}(t_0) + D_{\text{MS}}(t_0)}{c_0} \quad (6.19)$$

where the initial delay $\tau_n(t_0)$ are randomly drawn from the exponential delay distribution, as explained in the original IMT-A channel models, for a given scenario [33].

Substituting (6.6), (6.7), (6.8) into (6.17), we therefore can obtain the time-varying delays for n th cluster at different instant time t , i.e., $\tau_n(t)$. Delays are then normalised by subtracting the minimum delay and sort the normalised delays to descending order. The normalised delays are to be used in channel coefficient generation (6.3) but not in cluster power generation.

6.3.4 Time-varying power of clusters

Cluster powers are calculated assuming a single slope exponential power delay profile. The random averaged power for the n th cluster at time t_0 , denoted as $P_n(t_0)$, can be generated from the parameters given by the original IMT-A channel model [33]. Hence, the random average powers for the n th cluster at time t based on the time-varying delays calculated above, can be expressed as

$$P'_n(t) = e^{\frac{(1-r_{DS})(\tau_n(t))}{r_{DS} \cdot \sigma_{DS}}} \times 10^{-\frac{\xi_n}{10}} \quad (6.20)$$

where r_{DS} is the delay distribution proportionality factor, σ_{DS} is Delay Spread (DS), and ξ_n is the per cluster shadowing term in dB and they all can be obtained from Table A1-7 in [33]. Then, the calculated powers are usually normalised so that the total power for all cluster powers is equal to one, i.e.,

$$P_n(t) = \frac{P'_n(t)}{\sum_{n=1}^{N(t)} P'_n(t)}. \quad (6.21)$$

6.3.5 Time-varying AoDs

In terms of the interaction of relevant parameters, the time-varying function of AoD $\phi_{n,m}(t)$ can be expressed as follows [135]:

1) if $-\pi \leq \phi_{n,m}(t_0) < 0$,

$$\phi_{n,m}(t) = \phi_{n,m}(t_0) - \alpha_{n,m}(t), \quad \text{if } -\pi \leq \theta_A \leq \phi_{n,m}(t_0) \cup \phi_{n,m}(t_0) + \pi \leq \theta_A < \pi, \quad (6.22)$$

$$\phi_{n,m}(t) = \phi_{n,m}(t_0) + \alpha_{n,m}(t), \quad \text{if } \phi_{n,m}(t_0) < \theta_A < \phi_{n,m}(t_0) + \pi. \quad (6.23)$$

2) if $0 \leq \phi_{n,m}(t_0) < \pi$,

$$\phi_{n,m}(t) = \phi_{n,m}(t_0) + \alpha_{n,m}(t), \quad \text{if } -\pi \leq \theta_A \leq \phi_{n,m}(t_0) - \pi \cup \phi_{n,m}(t_0) \leq \theta_A < \pi, \quad (6.24)$$

$$\phi_{n,m}(t) = \phi_{n,m}(t_0) - \alpha_{n,m}(t), \quad \text{if } \phi_{n,m}(t_0) - \pi < \theta_A < \phi_{n,m}(t_0), \quad (6.25)$$

where

$$\alpha_{n,m}(t) = \arccos \frac{D_{BS}(t_0) + v_A t \cos(\phi_{n,m}(t_0) - \theta_A)}{\sqrt{D_{BS}^2(t_0) + (v_A t)^2 + 2D_{BS}(t_0)v_A t \cos(\phi_{n,m}(t_0) - \theta_A)}}. \quad (6.26)$$

Note that $\phi_{n,m}(t_0)$, $D_{BS}(t_0)$, θ_A and v_A are assumed to be obtained from measurement.

6.3.6 Time-varying AoAs

Similarly, based on the interaction of relevant parameters, the time-varying function of AoA $\varphi_{n,m}(t)$ can be expressed as follows [135]:

1) If $-\pi \leq \varphi_{n,m}(t_0) < 0$,

$$\varphi_{n,m}(t) = \theta_v - \gamma_{n,m}(t) \pm \pi, \quad \text{if } -\pi \leq \theta_v < \varphi_{n,m}(t_0) \cup \pi + \varphi_{n,m}(t_0) < \theta_v < \pi, \quad (6.27)$$

$$\varphi_{n,m}(t) = \theta_v + \gamma_{n,m}(t) \pm \pi, \quad \text{if } \varphi_{n,m}(t_0) \leq \theta_v \leq \pi + \varphi_{n,m}(t_0), \quad (6.28)$$

2) if $0 \leq \varphi_{n,m}(t_0) < \pi$,

$$\varphi_{n,m}(t) = \theta_v + \gamma_{n,m}(t) \pm \pi, \quad \text{if } -\pi \leq \theta_v < \varphi_{n,m}(t_0) - \pi \cup \varphi_{n,m}(t_0) < \theta_v < \pi, \quad (6.29)$$

$$\varphi_{n,m}(t) = \theta_v - \gamma_{n,m}(t) \pm \pi, \quad \text{if } \varphi_{n,m}(t_0) - \pi \leq \theta_v \leq \varphi_{n,m}(t_0), \quad (6.30)$$

where

$$v = v_{MS/Z} = \|\vec{v}_{MS/Z}\|, \quad (6.31)$$

$$\theta_v = \theta_{MS/Z} = \mathbf{arg}(\vec{v}_{MS/Z}), \quad (6.32)$$

$$\gamma_{n,m}(t) = \arccos \frac{vt - D_{MS}(t_0) \cos(\theta_v - \varphi_{n,m})}{\sqrt{D_{MS}^2(t_0) + (vt)^2 - 2D_{MS}(t_0) v t \cos(\theta_v - \varphi_{n,m})}}. \quad (6.33)$$

Again, $\varphi_{n,m}(t_0)$, $D_{MS}(t_0)$, θ_Z , v_Z , θ_{MS} , and v_{MS} are assumed to be obtained from measurement campaign. It worth mentioning that “ $\pm\pi$ ” in (6.27) – (6.30) is the corrector to ensure $\varphi_{n,m}(t)$ within the range of $[-\pi, \pi)$.

6.4 Statistical Properties of Non-Stationary IMT-A MIMO Channel Models

6.4.1 Local spatial CCF

For WSSUS channels, the spatial CCF depends only on the relative BS and MS antenna element spacings, $\Delta d_s = |d_{s1} - d_{s2}|$ and $\Delta d_u = |d_{u1} - d_{u2}|$, respectively. However, for non-stationary systems, the spatial CCF does not only depend on the relative antenna spacings, but also on time t . Due to this dependency, spatial CCF of non-stationary channel model is called local spatial CCF and can be expressed as [98]

$$\begin{aligned} \rho_{s_2 u_2, n}^{s_1 u_1}(t, \Delta d_s, \Delta d_u) &= \mathbf{E} \{ h_{u_1, s_1, n}(t) h_{u_2, s_2, n}^*(t) \} \\ &= \frac{1}{M} \sum_{m=1}^M \mathbf{E} \{ P_n(t) e^{jk \Delta d_s \sin(\phi_{n,m}(t))} e^{jk \Delta d_u \sin(\varphi_{n,m}(t))} \} \end{aligned} \quad (6.34)$$

where $(\cdot)^*$ denotes the complex conjugation operation and $\mathbf{E}\{\cdot\}$ designates the statistical expectation operator.

Under the WSSUS assumption, the AoAs and AoDs are considered as time-invariant. In this case, the spatial CCF will be reduced to [165]

$$\begin{aligned} \rho_{s_2 u_2, n}^{s_1 u_1}(\Delta d_s, \Delta d_u) &= \mathbf{E} \{ h_{u_1, s_1, n}(t) h_{u_2, s_2, n}^*(t) \} \\ &= \frac{P_n}{M} \sum_{m=1}^M \mathbf{E} \{ e^{jk \Delta d_s \sin(\phi_{n,m})} e^{jk \Delta d_u \sin(\varphi_{n,m})} \}. \end{aligned} \quad (6.35)$$

6.4.2 Local temporal ACF

Considering the birth/death process, a cluster has a probability of $e^{-\lambda_R(v_{MS}\Delta t + P_c(v_Z + v_A)\Delta t)}$ to survive from $(t - \Delta t)$ to t . Therefore, the local temporal ACF of the non-stationary IMT-A channel model of the n th cluster can be expressed as

$$\begin{aligned} r_n(t, \Delta t) &= \mathbf{E} \{ h_{u,s,n}(t) h_{u,s,n}^*(t - \Delta t) \} \\ &= e^{-\lambda_R(v_{MS}\Delta t + P_c(v_Z + v_A)\Delta t)} \frac{1}{M} \sum_{m=1}^M \mathbf{E} \{ P_n(t) A_{\varphi_{n,m}}(t, \Delta t) B_{\phi_{n,m}}(t, \Delta t) C_{\varphi_{n,m}}(t, \Delta t) \} \end{aligned} \quad (6.36)$$

where

$$A_{\varphi_{n,m}}(t, \Delta t) = e^{jkd_u[\sin(\varphi_{n,m}(t)) - \sin(\varphi_{n,m}(t + \Delta t))]}, \quad (6.37a)$$

$$B_{\phi_{n,m}}(t, \Delta t) = e^{jkd_s[\sin(\phi_{n,m}(t)) - \sin(\phi_{n,m}(t + \Delta t))]}, \quad (6.37b)$$

$$C_{\varphi_{n,m}}(t, \Delta t) = e^{-jk||v||[\cos(\varphi_{n,m}(t) - \theta_v)(t) - \cos(\varphi_{n,m}(t + \Delta t) - \theta_v)(t + \Delta t)]}. \quad (6.37c)$$

By applying the WSSUS assumption on (6.37), we get

$$A_{\varphi_{n,m}}(t, \Delta t) = 1, \quad (6.38a)$$

$$B_{\phi_{n,m}}(t, \Delta t) = 1, \quad (6.38b)$$

$$C_{\varphi_{n,m}}(t, \Delta t) = e^{jk||v||\cos(\varphi_{n,m} - \theta_v)\Delta t}. \quad (6.38c)$$

Therefore, (6.36) can be written as [165]

$$r_n(\Delta t) = \frac{P_n}{M} \sum_{m=1}^M \mathbf{E} \{ e^{jk||v||\cos(\varphi_{n,m} - \theta_v)\Delta t} \}. \quad (6.39)$$

6.4.3 Stationary Interval

The stationary interval can be calculated using APDPs that can be expressed as [77]

$$\overline{P_h}(t_k, \tau) = \frac{1}{N_{PDP}} \sum_k^{k+N_{PDP}-1} |h_{u,s}(t_k, \tau)|^2 \quad (6.40)$$

where N_{PDP} is the number of power delay profiles to be averaged, t_k is the time of the k th drop (snapshot), and $h_{u,s}(t_k, \tau) = \sum_{n=1}^N h_{u,s,n}(t_k) \delta(\tau - \tau_n)$. The correlation coefficient between two APDPs can be calculated as

$$c(t_k, \Delta t) = \frac{\int \overline{P_h}(t_k, \tau) \overline{P_h}(t_k + \Delta t, \tau) d\tau}{\max\{\int \overline{P_h}(t_k, \tau)^2 d\tau, \int \overline{P_h}(t_k + \Delta t, \tau)^2 d\tau\}}. \quad (6.41)$$

The stationary interval can be then calculated as

$$T_s(t_k) = \max\{\Delta t | c(t_k, \Delta t) \geq c_{\text{thresh}}\}, \quad (6.42)$$

where c_{thresh} is a given threshold of the correlation coefficient.

6.5 Simulation Results and Analysis

6.5.1 Local spatial CCF

By using the NLoS UMa scenario and main simulation parameters as follows: $\phi_{n,m}(t_0) = \text{random}$, $c(t_0) = 100$ m, $\theta_c = 15^\circ$, $v_c = 30$ m/s, $\varphi_{n,m}(t_0) = \text{random}$, $a(t_0) = 150$ m, $\theta_v = 120^\circ$, and $v = 20$ m/s, Fig. 6.5 shows the absolute values of three-dimensional (3D) local spatial CCF of the non-stationary IMT-A channel model. It is obvious that the absolute value of the local spatial CCF changes with time t due to the non-stationarity of the channel.

To highlight these changes, Fig. 6.6 shows two-dimensional (2D) analytical and simulated local spatial CCFs at three time instants, i.e., $t = 0, 5, 10$ s. It is clear that simulated results match analytical ones very well, verifying the correctness of our theoretical derivations as well as simulations.

6.5.2 Local temporal ACF

Still using the NLoS UMa scenario, the following parameters are used for simulating the local temporal ACF: $\phi_{n,m}(t_0) = \text{random}$, $c(t_0) = 100$ m, $\theta_c = 15^\circ$, $v_c = 30$ m/s,

$\varphi_{n,m}(t_0) = \text{random}$, $a(t_0) = 70$ m, $\theta_{MC} = -140^\circ$, $v_{MC} = 5$ m/s, $\theta_{MS} = 120^\circ$, and $v_{MS} = 20$ m/s.

Fig. 6.7 shows the absolute value of the 3D local temporal ACF of the non-stationary IMT-A channel model for the NLoS UMa scenario. Similar to the local spatial CCF, the absolute value of the local temporal ACF varies with time t because of the time-varying AoDs and AoAs. Fig. 6.8 illustrates this difference by plotting the 2D analytical and simulated local temporal ACF at three different time instants, i.e., $t = 0$ s, $t = 5$ s, and $t = 10$ s. Again, the simulated results match analytical results very well, verifying the correctness of our theoretical derivations as well as simulations.

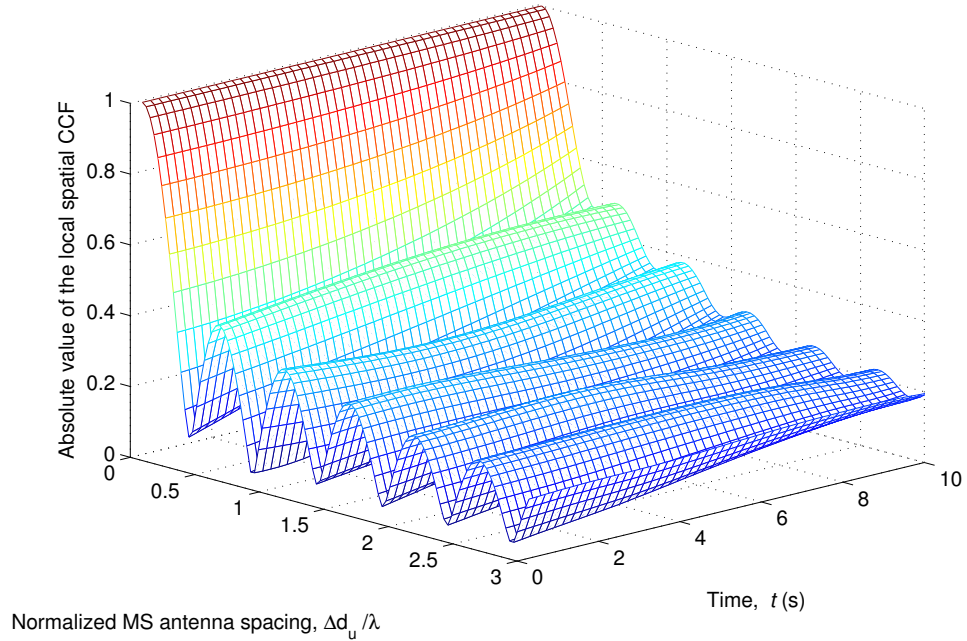


FIGURE 6.5: The absolute value of the local spatial CCFs of the non-stationary IMT-A channel model (UMa NLoS scenario, $\phi_{n,m}(t_0) = \text{random}$, $c(t_0) = 100$ m, $\theta_c = 15^\circ$, $v_c = 30$ m/s, $\varphi_{n,m}(t_0) = \text{random}$, $a(t_0) = 150$ m, $\theta_v = 120^\circ$, and $v = 20$ m/s).

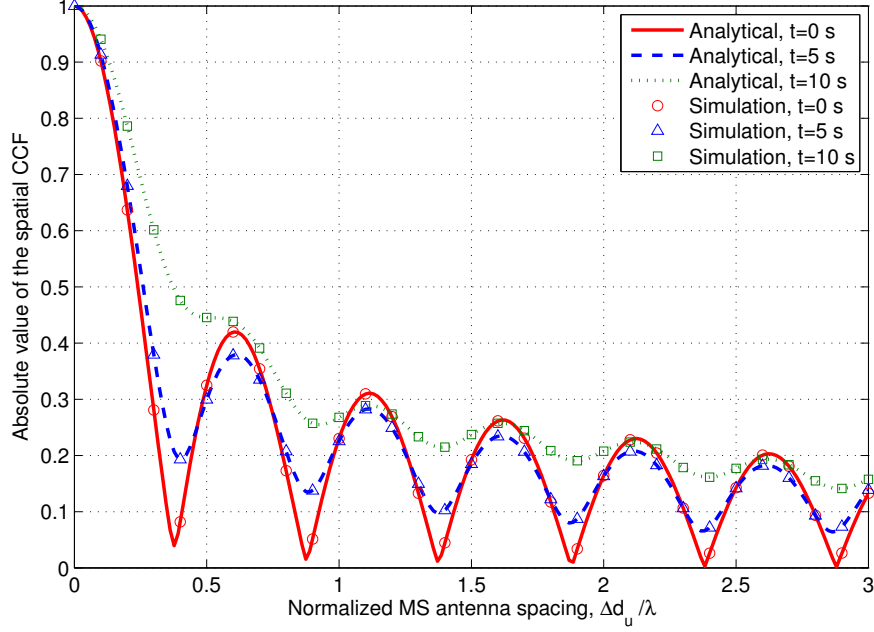


FIGURE 6.6: The analytical and simulated local spatial CCFs of the non-stationary IMT-A at different time instants (UMa NLoS scenario, $\phi_{n,m}(t_0) = \text{random}$, $c(t_0) = 100$ m, $\theta_c = 15^\circ$, $v_c = 30$ m/s, $\varphi_{n,m}(t_0) = \text{random}$, $a(t_0) = 150$ m, $\theta_v = 120^\circ$, and $v = 20$ m/s).

6.5.3 Stationary Interval

Fig. 6.9 shows the empirical CCDFs of the stationary intervals for our proposed non-stationary IMT-A channel model, the original IMT-A channel model, and the measured HST channel in [77]. The simulation parameters are selected according to the measurement setup in [77], which are listed as follows: $f_c = 2$ GHz, $v = 90$ m/s, $c_{\text{thresh}} = 0.8$. For the non-stationary channel model, $\theta_A = 15^\circ$, $D_{\text{BS}}(t_0) = 100$ m, $v_A = 30$ m/s, $D_{\text{MS}}(t_0) = 70$ m, and $\theta_v = 0^\circ$. It is worth mentioning that since the measured HST channel is narrowband one, in (6.40) we used $h_{u,s}(t_k, \tau) = h_{u,s,1}(t_k) \delta(\tau - \tau_1)$ where $h_{u,s,1}(t_k)$ can be obtained from (6.4). The good agreement between the proposed channel model and the measured channel demonstrates the feasibility of our non-stationary IMT-A channel model. From Fig. 6.9, the stationary interval of the proposed model is equal to 12.5 ms for 80% and 20 ms for 60% while the measured data is 9 ms for 80% and 20 ms for 60%, which are considerably shorter than the ones of original IMT-A channel model, i.e., 22.5 ms for 80% and 38.3 ms for 60%.

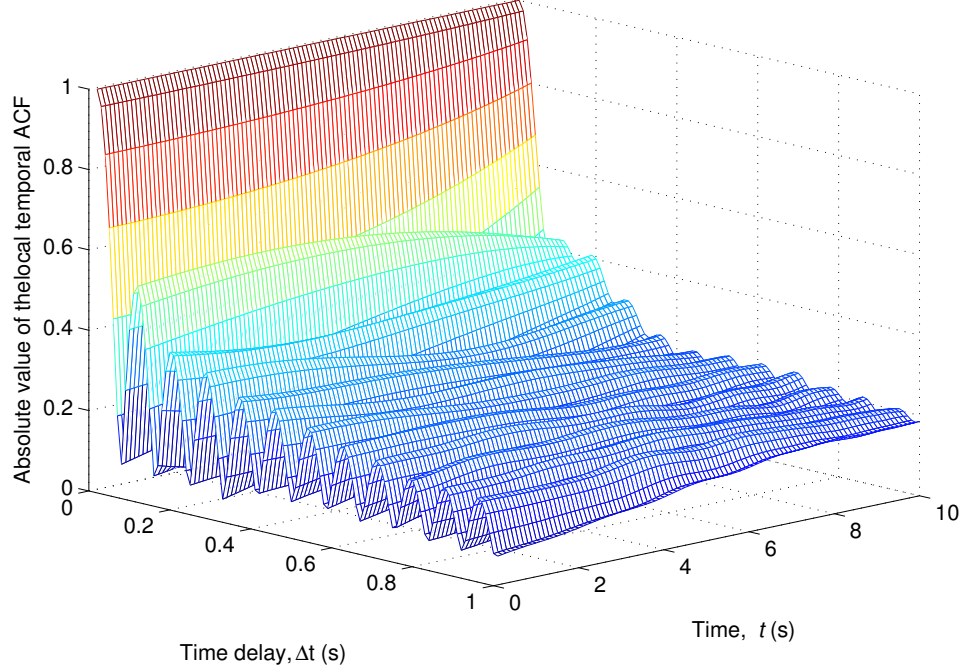


FIGURE 6.7: The absolute value of the local temporal ACFs of the non-stationary IMT-A channel model (UMa NLoS scenario, $\phi_{n,m}(t_0) = \text{random}$, $c(t_0) = 100$ m, $\theta_c = 15^\circ$, $v_c = 30$ m/s, $\varphi_{n,m}(t_0) = \text{random}$, $a(t_0) = 70$ m, $\theta_{MC} = -140^\circ$, $v_{MC} = 5$ m/s, $\theta_{MS} = 120^\circ$, and $v_{MS} = 20$ m/s).

To highlight the impact of the time-variant model parameters on the stationary interval, Fig. 6.10 shows the empirical CCDF of stationary intervals for the original IMT-A channel model and the proposed non-stationary IMT-A channel model with all time-variant parameters, time-variant delays and powers, and time-variant angular parameters. The simulation parameters are the same as the ones of Fig. 6.9 apart from the relative speed which is $v = 60$ m/s. According to Fig. 6.9, the time-variant angular parameters have more noticeable impact on the stationary interval compared with the time-variant clusters' delays and powers.

Finally, it should also be noted that the stationary intervals of the proposed non-stationary IMT-A channel model depend on the movement parameters, e.g., the MS moving direction, the MC moving direction, the AoA spread, and so on.

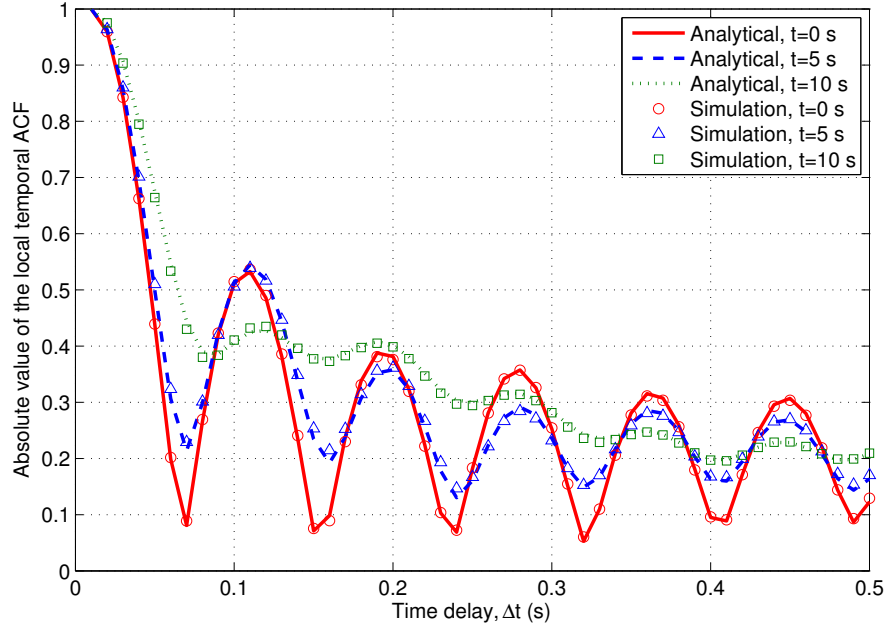


FIGURE 6.8: The analytical and simulated local temporal ACFs of the non-stationary IMT-A at different time instants (UMa NLoS scenario, $\phi_{n,m}(t_0) = \text{random}$, $c(t_0) = 100$ m, $\theta_c = 15^\circ$, $v_c = 30$ m/s, $\varphi_{n,m}(t_0) = \text{random}$, $a(t_0) = 70$ m, $\theta_{MC} = -140^\circ$, $v_{MC} = 5$ m/s, $\theta_{MS} = 120^\circ$, and $v_{MS} = 20$ m/s).

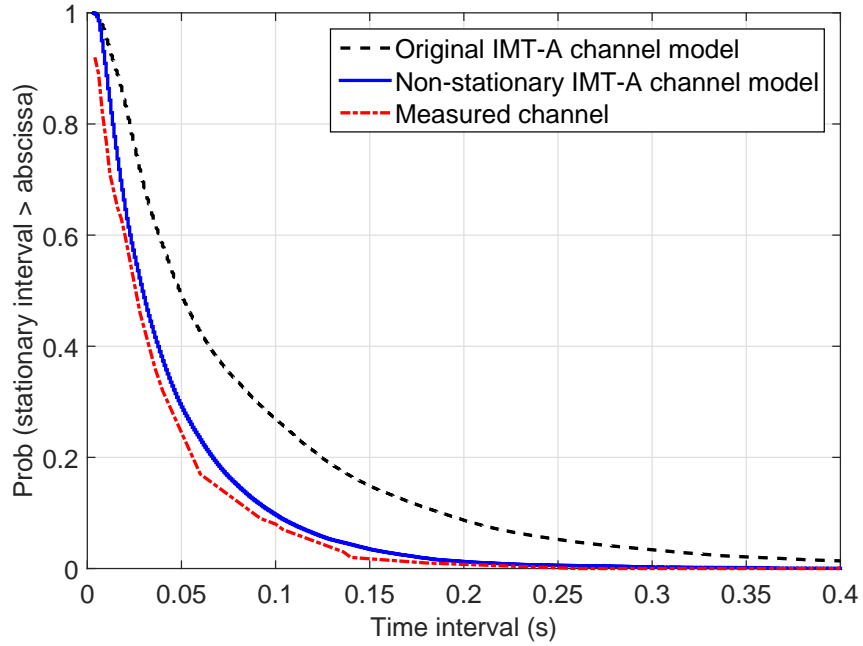


FIGURE 6.9: The empirical CCDF of stationary intervals for the proposed non-stationary IMT-A model, the original IMT-A model, and a measured HST channel ($f_c = 2$ GHz, $v = 90$ m/s, $N_{PDP} = 15$, $c_{\text{thresh}} = 0.8$).

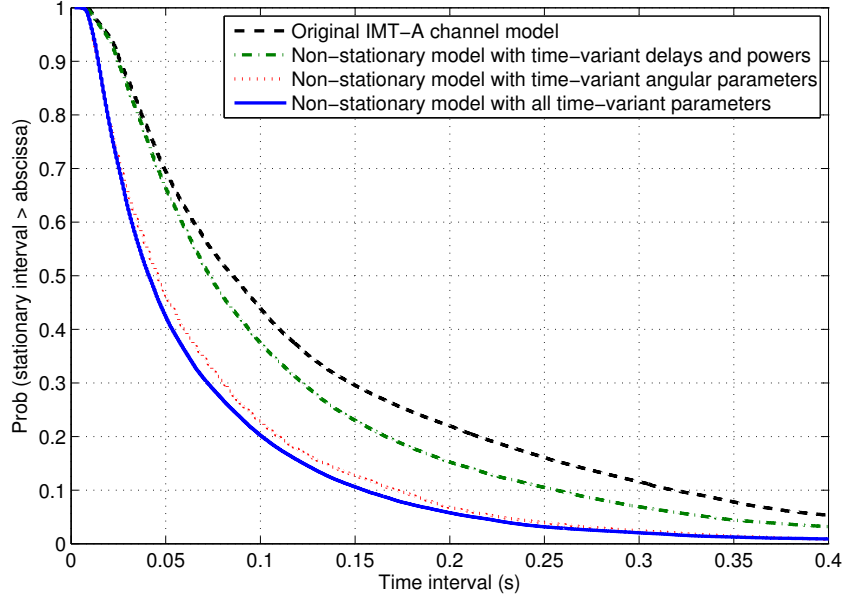


FIGURE 6.10: The empirical CCDF of stationary intervals for the original IMT-A model and the proposed non-stationary IMT-A model with all time-variant parameters, time-variant delays and powers, and time-variant angular parameters ($f_c = 2$ GHz, $v = 60$ m/s, $N_{PDP} = 15$, $c_{\text{thresh}} = 0.8$).

6.6 Summary

In this chapter, we have proposed a non-stationary IMT-A MIMO channel model to investigate the time variation of the wireless channels in different moving scenarios by considering small-scale time-varying parameters, i.e., the number of clusters, delays, and the powers of clusters, and time-varying AoDs, AoAs. Based on the proposed non-stationary IMT-A channel model, the statistical properties in terms of the local spatial CCF and local temporal ACF have been derived. The simulation results have shown that the statistical properties would vary with time due to the time-variant parameters of the proposed channel model. The good agreement between the analytical and simulation results has verified the correctness of the analytical derivations as well as simulations. In addition, a channel characteristic called stationary interval has been investigated in terms of APDPs. Corresponding simulation results have proved that the stationary intervals of the proposed non-stationary IMT-A channel model match well that of the measured data and are considerably shorter than those in the original standard WSSUS IMT-A channel model, demonstrating the ability of the proposed model to accurately mimic the characteristics of high-mobility channels.

Chapter 7

Conclusions and Future Work

Accurate channel models that are able to mimic key characteristics of wireless channels play an important role in designing and testing future HST communication systems. This thesis presents a comprehensive research on geometry-based wireless channel modelling and simulation for MIMO HST communication systems. The novelty and importance of this research has been introduced in details. In this chapter, the key findings of my PhD research are summarised and several potential future research directions are outlined.

7.1 Summary of Results

In Chapter 3, a theoretical framework that explains in details the characterisation of non-stationary mobile fading channels is established. The proposed framework introduces important system functions and CFs of non-stationary channel and highlight the relation between these functions. This framework is used as a guideline to derive the statistical properties of the non-stationary channel models proposed in this thesis.

In Chapter 4, a novel and generic non-stationary theoretical GBSM and the corresponding simulation model have been proposed for wideband MIMO HST channels. The proposed models are the first generic models that are adaptable to the most common HST scenarios, i.e, the open space, viaduct, and cutting scenarios. The proposed

models have the ability to investigate the impact of different scenario-specific parameters of each HST scenario on the wireless channel, e.g., the height of the viaduct, the dimensions of the cuttings, and the isotropy of the environment in open space. To mimic the non-stationarity of the HST channels, the proposed models have several time-varying parameters, i.e., angular parameters, Ricean K -factor, and distance between the Tx and Rx. The application of the proposed models are not limited to HST channels nor the aforementioned scenarios. In other words, they can be further used to model non-stationary V2I channels in other 5G high-mobility scenarios, e.g., highway scenario, and can be applied on other HST scenarios, e.g., hilly terrain, by choosing proper values of different channel parameters. The statistical properties of both models have been investigated thoroughly. The results show that the simulation model closely approximates the reference model. The statistics of the simulation model have been verified by simulation. Moreover, the close agreement between the statistics of the simulation model and those of measured channels in the three aforementioned HST scenarios confirms the utility of the proposed generic model. Numerical analyses have shown that these statistical properties experience different behaviours at different time instants, demonstrating the capability of the proposed models to mimic the non-stationarity of HST channels. The dominance of the LoS component in HST open space scenario has resulted in higher correlation in the first tap of the proposed channel models in comparison with the second one. It has also been demonstrated that the time-varying angles will affect the time-variant space CCFs and time-variant ACFs while the time-varying dimensions of the ellipses will only have an influence on the time-variant ACFs. Moreover, the trends of the time-variant SD PSDs are considerably affected by the angular parameters of the channel models. Furthermore, it has been demonstrated that wider cutting's dimensions can result in a stronger LoS component observed at the receiver. This in turn will result in higher Ricean K -factor values which will lead to higher ACF values. Finally, it has been shown that the stationary intervals of our simulation model are considerably shorter than that of the standard channel models and match well with the ones reported in measurement campaigns in the literature.

In Chapter 5, a generic 3D non-stationary theoretical GBSM has been proposed for

non-isotropic scattering wideband MIMO HST fading channels. Using a parameter computation method called MEV, the corresponding SoS simulation model has been developed. The proposed models have the ability to investigate the impact of the non-stationarity, the key scenario-specific parameters, and the elevation angles on the channel statistics in different HST scenarios. Based on the proposed models, important non-stationary statistical properties have been derived and thoroughly investigated, i.e., the time-variant ST CF, the time-variant CCF, and the time-variant ACF besides the stationary interval. The simulation results have shown that elevation angle has considerable impact on the CFs. Finally, it has been shown that the stationary intervals of our proposed non-stationary 3D simulation model have excellent agreement with those of a measured HST channel.

In Chapter 6, a non-stationary IMT-A MIMO channel model is proposed to investigate the time variation of the wireless channels in high-mobility scenarios. The developed model takes into account several small-scale time-varying parameters, i.e., the number of clusters, the delays & the powers of clusters, and time-varying AoDs & AoAs. Based on the proposed non-stationary IMT-A channel model, the statistical properties in terms of the non-stationary spatial CCF and non-stationary temporal ACF have been derived. The simulation results have shown that the statistical properties would vary with time due to the time-variant parameters of the proposed channel model. The good agreement between the analytical and simulation results has verified the correctness of the analytical derivations as well as simulations. Simulation results have proved that the stationary intervals of the proposed non-stationary IMT-A channel model match well that of the measured data and are considerably shorter than those in the original standard WSSUS IMT-A channel model, demonstrating the ability of the proposed model to accurately mimic the characteristics of high-mobility channels.

7.2 Future Research Topics

7.2.1 Channel Measurements and Models for HST-to-HST Communication

HST-to-HST communication is proposed to enable HSTs exchange controlling and traffic information such as road obstacles and accidents via the wireless communication links. A HST-to-HST communication model based on multihop and cooperation was proposed in [166]. In the proposed model, a source train uses trains on other tracks as relays to transmit signals to destination train on the same track. Based on proposed HST-to-HST channel model, the Bit Error Rate (BER) performance was investigated in [166] using suburban scenario of COST207 channel model, and the outage capacity was analysed in [167] using Nakagami- m channel model. Despite its importance as a safety measure to avoid accidents, the measurements of HST-to-HST channels and the development of corresponding channel models are still in its preliminary phase and further investigations are required. The proposed BS-to-HST channel models presented in this thesis can be further developed to HST-to-HST ones by assuming a moving vector at the BS side.

7.2.2 Massive MIMO for HST Communication Systems

Since HST scenarios have been recognised as one of the typical scenarios for 5G, related 5G key technologies and the corresponding channel modelling in HST scenarios should be paid more attention. Massive MIMO systems [168], which are equipped with tens or even hundreds of antennas, emerged as an enhanced MIMO technique that can help in meeting the increasing demand on data of the 5G wireless communication systems. Unlike the case of limited space in small wireless devices such as MSs, the vast room at the top of the HST leaves no concern regarding the possibility of deploying large antenna arrays at the MRS side. However, due to the huge number of antennas in massive MIMO systems, massive MIMO channel models need to consider

new phenomena unprecedented in conventional MIMO systems, such as the non-stationarity on the array axis [117], [164]. Therefore, measurements and channel models of massive MIMO channels in HST communications systems should be paid more attention.

7.2.3 Tunnel Scenario

In this thesis, we have presented generic channel models that can be applied in various HST scenarios, i.e., open space, viaduct, and cuttings, and can be easily further developed to consider other scenarios such as hilly terrains. However, due to the unique environment of tunnels, the propagation characteristics of signals inside them are different from those of other HST scenarios. Conventional channel modelling techniques suitable for other HST scenarios are not directly applicable to tunnel scenarios. Moreover, research on channel modeling inside tunnels is yet to solve main problems such as the accurate characterisation of multimode waveguide propagation and the determination of breakpoint for different propagation mechanisms inside tunnels. In addition, the research on 3D channel models for tunnels is still in its very early stages and accurate generic channel models that can be applied to different types of tunnel channels are still missing in the literature. Therefore, channel characterisation and modelling for tunnel scenario are still a quite challenging topic and needs to be further investigated.

7.2.4 Indoor Scenario

Most HST channel measurements and models in the literature have focused on the outdoor HST scenarios while indoor one has rarely been investigated. The measurement campaign, presented in [42], has studied the propagation loss in HST channels when the Tx and Rx are located inside the same HST carriage and when they are located in different carriages. The measured results showed that the waves travelling inside the train carriages are dominant compared to the ones reflected from scatterers outside the HST due to the high penetration loss of wireless signals traveling through

the metal body of the carriages. On the contrary, the waves reflected from outer scatterers are dominant compared to the waves travelling inside the train carriages when the communicating devices are located in different carriages due to the high insulation between these carriages. The aforementioned results can be greatly related to design of the HST and the measurement scenario. Therefore, more measurements for indoor scenarios in HSTs are needed before confirming that these observations are conclusive and accurate indoor HST channel models are required. By combining accurate indoor HST channel models with the outdoor ones presented in this thesis we can have end-to-end channel models that are indispensable for the development of future HST communication systems.

References

- [1] C.-X. Wang, F. Haider, X. Gao, X.-H. You, Y. Yang, D. Yuan, H. Aggoune, H. Haas, S. Fletcher, E. Hepsaydir, “Cellular architecture and key technologies for 5G wireless communication networks,” *IEEE Commun. Mag.*, vol. 52, no. 2, pp. 122–130, Feb. 2014.
- [2] A. Osseiran, F. Boccardi, V. Braun, K. Kusume, P. Marsch, M. Maternia, O. Queseth, M. Schellmann, H. Schotten, H. Taoka, H. Tullberg, M. A. Uusitalo, B. Timus, and M. Fallgren, “Scenarios for 5G mobile and wireless communications: the vision of the METIS project,” *IEEE Commun. Mag.*, vol. 52, no. 2, pp. 26–35, May 2014.
- [3] J. G. Andrews, S. Buzzi, W. Choi, S. V. Hanly, A. Lozano, A.C.K. Soong, and J. C. Zhang, “What Will 5G Be?,” *IEEE J. Sel. Areas Commun.*, vol. 32, no. 6, pp. 1065–1082, June 2014.
- [4] F. Abrishamkar and J. Irvine, “Comparison of current solutions for the provision of voice services to passengers on high speed trains,” in *Proc. IEEE VTC’00-Fall*, Boston, USA, Sept. 2000, pp. 1498–1505.
- [5] D. T. Fokum and V. S. Frost, “A survey on methods for broadband internet access on trains,” *IEEE Commun. Surveys Tuts*, vol. 12, no. 2, pp. 171–185, 2nd Quarter 2010.

- [6] J. Calle-Sánchez, M. Molina-Garcia, J. I. Alonso, and A. FernándezDurán, “Long term evolution in high speed railway environments: Feasibility and challenges,” *Bell Labs Techn. J.*, vol. 18, no. 2, pp. 237-253, Sept. 2013.
- [7] B. Ai, X. Cheng, T. Kurner, Z.-D. Zhong, K. Guan, R.-S. He, L. Xiong, D. W. Matolak, D. G. Michelson, and C. Briso-Rodriguez, “Challenges toward wireless communications for high-speed railway,” *IEEE Trans. Intell. Transp. Syst.*, vol. 15, no. 5, pp. 2143–2158, Oct. 2014.
- [8] M. Goller, “Application of GSM in high speed trains: measurements and simulations,” *IEE Colloquium Radiocommunications Trans.*, pp. 1–7, May 1995.
- [9] C. Briso, C. Cortes, F. J. Arques, and J. I. Alonso, “Requirements of GSM technology for the control of high speed trains,” in *Proc. IEEE PIMRC’02*, Lisbon, Portugal, Sept. 2002, pp. 792–793.
- [10] K. Kastell, S. Bug, A. Nazarov, and R. Jakoby, “Improvements in railway communication via GSM-R,” in *Proc. IEEE VTC’06-Spring*, Melbourne, Australia, May 2006, pp. 3026–3030.
- [11] K. Guan, Z. Zhong, and B. Ai, “Assessment of LTE-R using high speed railway channel model,” in *Proc. CMC’11*, Qingdao, China, Apr. 2011, pp. 461–464.
- [12] M. Cheng, X. Fang, and W. Luo, “Beamforming and positioning-assisted handover scheme for long-term evolution system in high-speed railway,” *IET Commun.*, vol. 6, no. 15, pp. 2335–2340, Oct. 2012.
- [13] M. Alasali and C. Beckman, “LTE MIMO performance measurements on trains,” in *Proc. EuCAP’13*, Gothenburgh, Sweden, Apr. 2013, pp. 2327–2330.
- [14] F. J. Martin-Vega, I. M. Delgado-Luque, F. Blázquez-Casado, G. Gomez, M. C. Aguayo-Torres, and J. T. Entrambasaguas, “LTE performance over high speed railway channel,” in *Proc. IEEE VTC’13-Fall*, Las Vegas, USA, Sept. 2013, pp. 1–5.

- [15] 3GPP, TS36.101, V12.7.0, “3rd Generation Partnership Project; Technical Specification Group Radio Access Network; Evolved Universal Terrestrial Radio Access (E-UTRA); User Equipment (UE) radio transmission and reception (Release 12),” Mar. 2015.
- [16] A. Diaz Zayas, C. A. Garcia Perez, and P. Merino Gomez, “Third-generation partnership project standards: For delivery of critical communications for railways,” *IEEE Veh. Technol. Mag.*, vol. 9, no. 2, pp. 58–68, June 2014.
- [17] K. Yamada, Y. Sakai, T. Suzuki, Y. Kawahara, T. Asami, and H. Aida, “A communication system with a fast handover under a high speed mobile environment,” in *Proc. IEEE VTC’10-Fall*, Ottawa, Canada, Sept. 2010, pp. 1–5.
- [18] J. Wang, H. Zhu, and N. J. Gomes, “Distributed antenna systems for mobile communications in high speed trains,” *IEEE J. Sel. Areas Commun.*, vol. 30, no. 4, pp. 675–683, May 2012.
- [19] H.-A. Hou and H.-H. Wang, “Analysis of distributed antenna system over high-speed railway communication,” in *Proc. IEEE PIMRC’12*, Sydney, Australia, Sept. 2012, pp. 1300–1305.
- [20] C. Yang, L. Lu, C. Di, and X. Fang, “An on-vehicle dual-antenna handover scheme for high-speed railway distributed antenna system,” in *Proc. IEEE WiCOM’10*, Chengdu, China, Sept. 2010, pp. 1–4.
- [21] D. Lee, H. Seo, B. Clerckx, E. Hardouin, D. Mazzarese, S. Nagata, and K. Sayana, “Coordinated multipoint transmission and reception in LTE-advanced: deployment scenarios and operational challenges,” *IEEE Commun. Mag.*, vol. 50, no. 2, pp. 148–155, Feb. 2012.
- [22] C.-X. Wang, X. Hong, X. Ge, X. Cheng, G. Zhang, and J. S. Thompson, “Cooperative MIMO channel models: a survey,” *IEEE Commun. Mag.*, vol. 48, no. 2, pp. 80–87, Feb. 2010.

- [23] O. B. Karimi, L. J. Liu, and C. Wang, “Seamless wireless connectivity for multimedia services in high speed trains,” *IEEE J. Sel. Areas Commun.*, vol. 30, no. 4, pp. 729–739, May 2012.
- [24] L. Tian, Y. Zhou, J. Li, Y. Huang, J. Shi, and J. Zhou, “A novel handover scheme for seamless wireless connectivity in high-speed rail,” in *Proc. IEEE WiMob’11*, Wuhan, China, Oct. 2011, pp. 230–236.
- [25] L. Tian, J. Li, Y. Huang, J. Shi, and J. Zhou, “Seamless dual-link handover scheme in broadband wireless communication systems for high-speed rail,” *IEEE J. Sel. Areas Commun.*, vol. 30, no. 4, pp. 708–718, May 2012.
- [26] Y. Zhou, Z. Pan, J. Hu, J. Shi, and X. Mo, “Broadband wireless communications on high speed trains,” in *Proc. IEEE WOCC’11*, New Jersey, USA, Apr. 2011, pp. 1–6.
- [27] F. Haider, C.-X. Wang, H. Haas, D. Yuan, H. Wang, X. Gao, X.-H. You, and E. Hepsaydir, “Spectral efficiency analysis of mobile femtocell based cellular systems,” in *Proc. IEEE ICCT’11*, Jinan, China, Sept. 2011, pp. 347–351.
- [28] F. Haider, C.-X. Wang, B. Ai, H. Haas, and E. Hepsaydir, “Spectral-energy efficiency trade-off of cellular systems with mobile femtocell deployment,” *IEEE Trans. Veh. Technol.*, accepted for publication.
- [29] X. Qian, H. Wu, and J. Meng, “A dual-antenna and mobile relay station based handover in distributed antenna system for high-speed railway,” in *Proc. IEEE IMIS’13*, Taichung, Taiwan, July 2013, pp. 585–590.
- [30] W. Luo, R. Zhang, and X. Fang, “A CoMP soft handover scheme for LTE systems in high speed railway,” *EURASIP J. Wireless Commun. Networking*, vol. 2012, 9 pages, 2012. doi:10.1186/1687-1499-2012-196.
- [31] B. Lannoo, D. Colle, M. Pickavet, and P. Demeester, “Radio-over-fiber-based solution to provide broadband internet access to train passengers,” *IEEE Commun. Mag.*, vol. 45, no. 2, pp. 56–62, Feb. 2007.

- [32] J.-Y. Zhang, Z.-H. Tan, and X.-X. Yu, "Coverage efficiency of radio-over-fiber network for high-speed railways," in *Proc. IEEE WiCOM'10*, Chengdu, China, Sept. 2010, pp. 1–4.
- [33] ITU-R M.2135-1, "Guidelines for Evaluation of Radio Interface Technologies for IMT-Advanced," Geneva, Switzerland, Rep. ITU-R M.2135-1, Dec. 2009.
- [34] P. Kyosti, et al., "WINNER II channel models," IST-4-027756, WINNER II D1.1.2, v1.2, Apr. 2008.
- [35] ITU-R M.2320-0, "Future technology trends of terrestrial IMT systems," Geneva, Switzerland, Rep. ITU-R M.2320-0, Nov. 2011.
- [36] B. Ai, R. He, Z. Zhong, K. Guan, B. Chen, P. Liu, and Y. Li, "Radio wave propagation scene partitioning for high-speed rails," *Int. J. Antennas Propag.*, vol. 2012, Article ID 815232, 7 pages, 2012. doi:10.1155/2012/815232.
- [37] "Universal Mobile Telecommunications System (UMTS); Radio Frequency (RF) system scenarios (Release 12)," 3GPP TR 25.942, version 12.0.0, Oct. 2014.
- [38] L. Liu, J. Poutanen, F. Quitin, K. Haneda, F. Tufvesson, P. De Doncker, P. Vainikainen, and C. Oestges, "The COST 2100 MIMO channel model," *IEEE Wireless Commun.*, vol. 19, no. 6, pp. 92-99, Dec. 2012.
- [39] "Requirements for the Radio Interface(s) for International Mobile Telecommunications-2000 (IMT-2000)," ITU, Geneva, Switzerland, Tech. Rep. ITU-R M.1034-1, 2000.
- [40] J. Yang, B. Ai, and Z. Zhong "Construction and capacity analysis of high-rank LoS MIMO channels in high speed railway scenarios," *Int. J. Antennas Propag.*, vol. 2012, Article ID 423759, 7 pages, 2012. doi:10.1155/2012/423759.
- [41] J. Rodríguez-Piñeiro, J. A. García-Naya, Á. Carro-Lagoa, and L. Castedo, "A testbed for evaluating LTE in high-speed trains," in *Proc. IEEE DSD'13*, Santander, Spain, Sept. 2013, pp. 175–182.

- [42] N. Kita, T. Ito, S. Yokoyama, M-C. Tseng, Y. Sagawa, M. Ogasawara, and M. Nakatsugawa, “Experimental study of propagation characteristics for wireless communications in high-speed train cars,” in *Proc. IEEE EuCAP’09*, Berlin, Germany, Mar. 2009, pp. 897–901.
- [43] W. Dong, G. Liu, L. Yu, H. Ding, and J. Zhang, “Channel properties of indoor part for high-speed train based on wideband channel measurement,” in *Proc. CHINACOM’10*, Beijing, China, Aug. 2010, pp. 1–4.
- [44] M. Zhao, M. Wu, Y. Sun, D. Yu, S. Di, P. Zhou, X. Zeng, and S. Ge, “Analysis and modeling for train-ground wireless wideband channel of LTE on high-speed railway,” in *Proc. IEEE VTC’13-Spring*, Dresden, Germany, June 2013, pp. 1–5.
- [45] K. Pekka, “WINNER II channel models part II radio channel measurement and analysis results,” IST-4-027756, WINNER II D1.1.2, v1.0, Sep. 2007.
- [46] R. Parviainen, P. Kyosti, Y. Hsieh, P. Ting, and J. Chiou, “Results of high speed train channel measurements,” in *COST 2100 TD’08*, Lille, France, Oct. 2008.
- [47] R. He, A. F. Molisch, Z. Zhong, B. Ai, J. Ding, R. Chen, and Z. Li, “Measurement based channel modeling with directional antennas for high-speed railways,” in *Proc. IEEE WCNC’13*, Shanghai, China, Apr. 2013, pp. 2932–2936.
- [48] F. Luan, Y. Zhang, L. Xiao, C. Zhou, and S. Zhou, “Fading characteristics of wireless channel on high-speed railway in hilly terrain scenario,” *Int. J. Antennas Propag.*, vol. 2013, Article ID 378407, 9 pages, 2013. doi:10.1155/2013/378407.
- [49] Y. Zhang, Z. He, W. Zhang, L. Xiao, and S. Zhou, “Measurement-based delay and Doppler characterizations for high-speed railway hilly scenario,” *Int. J. Antennas Propag.*, vol. 2014, Article ID 875345, 8 pages, 2014. doi:10.1155/2014/875345.

- [50] H. Wei, Z. Zhong, K. Guan, and B. Ai, "Path loss models in viaduct and plain scenarios of the high-speed railway," in *Proc. CHINACOM'10*, Beijing, China, Aug. 2010, pp. 1–5.
- [51] J. Lu, G. Zhu, and B. Ai, "Radio propagation measurements and modeling in railway viaduct area," in *Proc. IEEE WiCOM'10*, Chengdu, China, Sept. 2010, pp. 1–5.
- [52] L. Gao, Z. Zhong, B. Ai, and L. Xiong, "Estimation of the Ricean K factor in the high speed railway scenarios," in *Proc. CHINACOM'10*, Beijing, China, Aug. 2010, pp. 1–5.
- [53] R. He, Z. Zhong, and B. Ai, "Path loss measurements and analysis for high-speed railway viaduct scene," in *Proc. IWCMC'10*, Caen, France, July 2010, pp. 266–270.
- [54] R. He, Z. Zhong, B. Ai, L. Xiong, and H. Wei, "A novel path loss model for high-speed railway viaduct scenarios," in *Proc. IEEE WiCOM'11*, Wuhan, China, Sept. 2011, pp. 1–4.
- [55] R. He, Z. Zhong, B. Ai, L. Xiong, and J. Ding, "The effect of reference distance on path loss prediction based on the measurements in high-speed railway viaduct scenarios," in *Proc. CHINACOM'11*, Harbin, China, Aug. 2011, pp. 1201–1205.
- [56] R. He, Z. Zhong, B. Ai, and J. Ding, "An empirical path loss model and fading analysis for high-speed railway viaduct scenarios," *IEEE Antennas Wireless Propag. Lett.*, vol. 10, pp. 808–812, Aug. 2011.
- [57] H. Wei, Z. Zhong, L. Xiong, B. Ai, and R. He, "Study on the shadow fading characteristic in viaduct scenario of the high-speed railway," in *Proc. CHINACOM'11*, Harbin, China, Aug. 2011, pp. 1216–1220.
- [58] L. Gao, Z. Zhong, B. Ai, L. Xiong, and H. Zhang, "Analysis and emulation of the small-scale fading characteristics in the high-speed rail scenarios," in *Proc. CHINACOM'11*, Harbin, China, Aug. 2011, pp. 1181–1185.

- [59] L. Liu, C. Tao, J. Qiu, H. Chen, L. Yu, W. Dong, and Y. Yuan, "Position-based modeling for wireless channel on high-speed railway under a viaduct at 2.35 GHz," *IEEE J. Sel. Areas Commun.*, vol. 30, no. 4, pp. 834–845, May 2012.
- [60] R. He, Z. Zhong, B. Ai, and J. Ding, "Measurements and analysis of short-term fading behavior for high-speed rail viaduct scenario," in *Proc. IEEE ICC'12*, Ottawa, Canada, June 2012, pp. 4563–4567.
- [61] R. He, Z. Zhong, B. Ai, and J. Ding, "Distance-dependent model of Ricean K-factors in high-speed rail viaduct channel," in *Proc. IEEE VTC'12-Fall*, Québec City, Canada, Sept. 2012, pp. 1–5.
- [62] Y. Guo, J. Zhang, C. Zhang, and L. Tian, "Correlation analysis of high-speed railway channel parameters based on channel measurement," in *Proc. HMWC'13*, Shanghai, China, Nov. 2013, pp. 1–5.
- [63] R. He, Z. Zhong, B. Ai, G. Wang, J. Ding, and A. F. Molisch, "Measurements and analysis of propagation channels in high-speed railway viaducts," *IEEE Trans. Wireless Commun.*, vol. 12, no. 2, pp. 794–805, Feb. 2013.
- [64] B. Zhang, Z. Zhong, B. Ai, D. Yao, and R. He, "Measurements and modeling of cross-correlation property of shadow fading in high-speed railways," in *Proc. IEEE VTC'14-Fall*, Vancouver, Canada, Sept. 2014, pp. 1–5.
- [65] Q. Wang, C. Xu, M. Zhao, and D. Yu, "Results and analysis for a novel 2x2 channel measurement applied in LTE-R at 2.6 GHz," in *Proc. IEEE WCNC'14*, Istanbul, Turkey, Apr. 2014, pp. 177–181.
- [66] R. Sun, C. Tao, L. Liu, Z. Tan, L. Zhang, and T. Zhou, "Nonisotropic scattering characteristic in an alternant tree-blocked viaduct scenario on high-speed railway at 2.35 GHz," *Int. J. Antennas Propag.*, vol. 2014, Article ID 642894, 9 pages, 2014. doi:10.1155/2014/642894.
- [67] T. Zhou, C. Tao, L. Liu, and Z. Tan, "A semiempirical MIMO channel model in obstructed viaduct scenarios on high-speed railway," *Int. J. Antennas Propag.*, vol. 2014, Article ID 287159, 10 pages, 2014. doi:10.1155/2014/287159.

- [68] J. Lu, G. Zhu, and C. Briso-Rodriguez, “Fading characteristics in the railway terrain cuttings,” in *Proc. IEEE VTC’11-Spring*, Budapest, Hungary, May 2011, pp. 1–5.
- [69] R. He, Z. Zhong, B. Ai, and J. Ding, “Propagation measurements and analysis for high-speed railway cutting scenario,” in *Electron. Lett.*, vol. 47, no. 21, pp. 1167–1168, Oct. 2011.
- [70] R. He, Z. Zhong, B. Ai, J. Ding, and Y. Yang, “Propagation measurements and analysis of fading behavior for high speed rail cutting scenarios,” in *Proc. IEEE GLOBALCOM’12*, California, USA, Dec. 2012, pp. 5015–5020.
- [71] R. He, Z. Zhong, B. Ai, J. Ding, Y. Yang, and A. F. Molisch, “Short-term fading behavior in high-speed railway cutting scenario: measurements, analysis, and statistical models,” *IEEE Trans. Antennas Propag.*, vol. 61, no. 4, pp. 2209–2222, Apr. 2013.
- [72] R. Sun, C. Tao, L. Liu, and Z. Tan, “Channel measurement and characterization for HSR U-Shape groove scenarios at 2.35 GHz,” in *Proc. IEEE VTC’13-Fall*, Las Vegas, USA, Sept. 2013, pp. 1–5.
- [73] L. Tian, J. Zhang, and C. Pan, “Small scale fading characteristics of wideband radio channel in the U-Shape cutting of high-speed railway,” in *Proc. IEEE VTC’13-Fall*, Las Vegas, USA, Sept. 2013, pp. 1–6.
- [74] C. Briso-Rodriguez, J. M. Cruz, and J. I. Alonso, “Measurements and modeling of distributed antenna systems in railway tunnels,” *IEEE Trans. Veh. Technol.*, vol. 56, no. 5, pp. 2870–2879, Sept. 2007.
- [75] P. Aikio, R. Gruber, and P. Vainikainen, “Wideband radio channel measurements for train tunnels,” in *Proc. IEEE VTC’98*, Ottawa, Canada, May 1998, pp. 460–464.
- [76] Y. Wen, Y. Ma, X. Zhang, X. Jin, and F. Wang, “Channel fading statistics in high-speed mobile environment,” in *Proc. IEEE APWC’12*, Cape Town, South Africa, Sept. 2012, pp. 1209–1212.

- [77] B. Chen, Z. Zhong, and B. Ai, "Stationarity intervals of time-variant channel in high speed railway scenario," *J. China Commun.*, vol. 9, no. 8, pp. 64–70, Aug. 2012.
- [78] J. Qiu, C. Tao, L. Liu, and Z. Tan, "Broadband channel measurement for the high-speed railway based on WCDMA," in *Proc. IEEE VTC'12-Spring*, Yokohama, Japan, May 2012, pp. 1–5.
- [79] L. Liu, C. Tao, T. Zhou, Y. Zhao, X. Yin, and H. Chen, "A highly efficient channel sounding method based on cellular communications for high-speed railway scenarios," *EURASIP J. Wireless Commun. Networking*, vol. 2012, 16 pages, 2012. doi:10.1186/1687-1499-2012-307.
- [80] K. Guan, Z. Zhong, B. Ai, and T. Kurner, "Propagation measurements and analysis for train stations of high-speed railway at 930 MHz," *IEEE Trans. Veh. Technol.*, vol. 63, no. 8, pp. 3349–3516, Oct. 2014.
- [81] K. Guan, Z. Zhong, B. Ai, and T. Kurner, "Empirical models for extra propagation loss of train stations on high-speed railway," *IEEE Trans. Antennas Propag.*, vol. 62, no. 3, pp. 1395–1408, Mar. 2014.
- [82] K. Guan, Z. Zhong, B. Ai, and T. Kurner, "Propagation measurements and modeling of crossing bridges on high-speed railway at 930 MHz," *IEEE Trans. Veh. Technol.*, vol. 63, no. 8, pp. 502–517, Feb. 2014.
- [83] R. He, D. Zhong, B. Ai, and C. Oestges, "Shadow fading correlation in high-speed railway environments," *IEEE Trans. Veh. Technol.*, vol. 64, no. 7, pp. 2762–2772, July 2015.
- [84] R. He, Z. Zhong, B. Ai, and B. Zhang, "Measurement-based auto-correlation model of shadow fading for the high-speed railways in urban, suburban, and rural environments," in *Proc. APSURSI'14*, Memphis, TN, USA, July 2014, pp. 949–950.

- [85] J. Lu, G. Zhu, and B. Ai, “Fading analysis for the high speed railway viaduct and terrain cutting scenarios,” *Int. J. Antennas Propag.*, vol. 2012, Article ID 862945, 9 pages, 2012.
- [86] M. Dohler and Y. Li, *Cooperative Communications: Hardware, Channel & PHY*. Chippenham: Wiley, 2010.
- [87] D. Wang, L. Song, X. Kong, and Z. Zhang, “Near-ground path loss measurements and modeling for wireless sensor networks at 2.4 GHz,” *Int. J. Distributed Sensor Net.*, vol. 2012, Article ID 969712, 10 pages, 2012. doi:10.1155/2012/969712.
- [88] K. Guan, Z. D. Zhong, J. I. Alonso, and C. Briso-Rodriguez, “Measurement of distributed antenna system at 2.4GHz in a realistic subway tunnel environment,” *IEEE Trans. Veh. Technol.*, vol. 61, no. 2, pp. 834–837, Feb. 2012.
- [89] K. Guan, Z. D. Zhong, and B. Ai, “Statistic modeling for propagation in tunnels based on distributed antenna systems,” in *Proc. IEEE APSURSI’13*, Florida, USA, July 2013, pp. 1920–1921.
- [90] L. Tian, X. Yin, Q. Zuo, J. Zhou, Z. Zhong, and S. Lu, “Channel modeling based on random propagation graphs for high speed railway scenarios,” in *Proc. IEEE PIMRC’12*, Sydney, Australia, Sept. 2012, pp. 1746–1750.
- [91] S. Knorzer, M. A. Baldauf, T. Fugen, and W. Wiesbeck, “Channel analysis for an OFDM-MISO train communications system using different antennas,” in *Proc. IEEE VTC’07-Fall*, Baltimore, USA, Oct. 2007, pp. 809–813.
- [92] D. J. Cichon, T. C. Becker, and W. Wiesbeck, “Determination of time-variant radio links in high-speed train tunnels by ray optical modeling,” in *Proc. IEEE APS/URSI’95*, California, USA, June 1995, pp. 508–511.
- [93] D. J. Cichon, T. Zwick, and W. Wiesbeck, “Ray optical modeling of wireless communications in high-speed railway tunnels,” in *Proc. IEEE VTC’96-Spring*, Atlanta, USA, May 1996, pp. 546–550.

- [94] B. Chen and Z. Zhong, “Geometry-based stochastic modeling for MIMO channel in high-speed mobile scenario,” *Int. J. Antennas Propag.*, vol. 2012, Article ID 184682, 6 pages, 2012. doi:10.1155/2012/184682.
- [95] Q. Zheng, C. Xu, and M. Wu, “A novel MIMO channel model for high speed railway system,” in *Proc. IEEE ICCT’12*, Chengdu, China, Nov. 2012, pp. 31–35.
- [96] A. Ghazal, C.-X. Wang, H. Haas, M. A. Beach, X. Lu, and D. Yuan, “A non-stationary MIMO channel model for high speed train communication systems,” in *Proc. IEEE VTC’12-Spring*, Yokohama, Japan, May 2012, pp. 1–5.
- [97] A. Ghazal, C.-X. Wang, H. Haas, M. Beach, R. Mesleh, D. Yuan, X. Ge, and M. K. Chahine, “A non-stationary geometry-based stochastic model for MIMO high-speed train channels,” invited paper, in *Proc. ITST’12*, Taipei, Taiwan, Nov. 2012, pp. 7–11.
- [98] A. Ghazal, C.-X. Wang, B. Ai, D. Yuan, and H. Haas, “A non-stationary wideband MIMO channel model for high-mobility intelligent transportation systems,” *IEEE Trans. Intell. Transp. Syst.*, vol. 16, no. 2, pp. 885–897, Apr. 2015.
- [99] S. Lin, Z. Zhong, L. Cai, and Y. Luo, “Finite state Markov modelling for high speed railway wireless communication channel,” in *Proc. IEEE GLOBE-COM’12*, California, USA, Dec. 2012, pp. 5421–5426.
- [100] S. Lin, L. Kong, L. He, K. Guan, B. Ai, Z. Zhong, and C. Rodriguez, “Finite-state Markov modeling for high-speed railway fading channels,” *IEEE Antennas Wireless Propag. Lett.*, vol. 14, pp. 954–957, Dec. 2015.
- [101] L. Liu, C. Tao, J. Qiu, T. Zhou, R. Sun, and H. Chen, “The dynamic evolution of multipath components in high-speed railway in viaduct scenarios: From the birth-death process point of view,” in *Proc. IEEE PIMRC’12*, Sydney, Australia, Sept. 2012, pp. 1774–1778.

- [102] K. Guan, Z. Zhong, B. Ai, and T. Kurner, "Deterministic propagation modeling for the realistic high-speed railway environment," in *Proc. IEEE VTC'13-Spring*, Dresden, Germany, June 2013, pp. 1–5.
- [103] B. Chen, Z. Zhong, B. Ai, and D. Michelson, "A geometry-based stochastic channel model for high-speed railway cutting scenarios," *IEEE Antennas Wireless Propag. Lett.*, vol. 14, pp. 851–854, Dec. 2015.
- [104] Y. Liu, C.-X. Wang, A. Ghazal, S. Wu, and W. Zhang, "A multi-mode waveguide tunnel channel model for high-speed train wireless communication systems", in *Proc. EuCAP'15*, Lisbon, Spain, Apr. 2015, pp. 1–5.
- [105] R. He, Z. Zhong, and C. Briso, "Broadband channel long delay cluster measurements and analysis at 2.4GHz in subway tunnels," in *Proc. IEEE VTC'11-Spring*, Budapest, Hungary, May 2011, pp. 1–5.
- [106] K. Guan, Z. Zhong, B. Ai, and T. Kurner, "Semi-deterministic path-loss modeling for viaduct and cutting scenarios of high-speed railway," *IEEE Antennas Wireless Propag. Lett.*, vol. 12, pp. 789–792, June 2013.
- [107] R. He, B. Ai, Z. Zhong, A. F. Molisch, R. Chen, and Y. Yang, "A measurement-based stochastic model for high-speed railway channels," *IEEE Trans. Intell. Transp. Syst.*, vol. 16, no. 3, pp. 1120–1135, June 2015.
- [108] P. Bello, "Characterization of randomly time-variant linear channels," *IEEE Trans. on Wireless Commun.*, vol. 11, no. 4, pp. 360–393, Dec. 1963.
- [109] R. Kattenbach, "Statistical modeling of small-scale fading in directional radio channels," *IEEE J. Sel. Areas Commun.*, vol. 20, no. 3, pp. 584–592, Apr. 2002.
- [110] B. H. Fleury, "First and second order characterization of direction dispersion and space selectivity in the radio channel", *IEEE Trans. Inform. Theory*, vol. 46, no. 6, pp. 2027–2044, Sept. 2000.
- [111] A. F. Molisch, *Wireless communications*. 2nd Edition. New York: Wiley-IEEE press, 2011.

- [112] S. Salous, *Radio propagation measurements and channel modelling*. Malaysia: Wiley, 2013.
- [113] M. Patzold, “System function and characteristics quantities of spatial deterministic Gaussian uncorrelated scattering processes,” in *Proc. IEEE VTC’03-Spring*, Jeju, Korea, Apr. 2003, pp. 256–261.
- [114] F. Hlawatsch and G. Matz, *Wireless communications over rapidly time-varying channels*. San Diego: Elsevier, 2011.
- [115] G. Matz, “On non-WSSUS wireless fading channels,” *IEEE Trans. on Wireless Commun.*, vol. 4, no. 5, pp. 2465–2478, Sept. 2005.
- [116] M. Herdin, “Non-Stationary Indoor MIMO Radio Channels,” PhD thesis, Technische Universitat Wien, Aug. 2004.
- [117] S. Payami and F. Tufvesson, “Channel measurements and analysis for very large array systems at 2.6 GHz,” in *Proc. EuCAP’12*, Prague, Czech Republic, Mar. 2012, pp. 433–437.
- [118] R. Vaughan and J. Bach-Anderson, *Channels, Propagation and Antennas for Mobile Communications*, London: IET, 2003.
- [119] D. W. Matolak and Q. Wu, “Vehicle-to-vehicle channels: are we done yet?,” in *Proc. IEEE GLOBECOM’09*, Hawaii, USA, Dec. 2009.
- [120] C.-X. Wang, X. Cheng, and D. I. Laurenson, “Vehicle-to-vehicle channel modeling and measurements: recent advances and future challenges”, *IEEE Commun. Mag.*, vol. 47, no. 11, pp. 96–103, Nov. 2009.
- [121] A. F. Molisch, F. Tufvesson, J. Karedal, and C. F. Mecklenbrauker, “A survey on vehicle-to-vehicle propagation channels,” *IEEE Trans. Wireless Commun.*, vol. 16, no. 6, pp. 12–22, Dec. 2009.
- [122] A. Paier, T. Zemen, L. Bernado, G. Matz, J. Karedal, N. Czink, C. Dumard, F. Tufvesson, A. F. Molisch, and C. F. Mecklenbrauker, “Non-WSSUS vehicular channel characterization in highway and urban scenarios at 5.2 GHz using the

- local scattering function,” in *WSA '08*, Darmstadt, Germany, Feb. 2008, pp. 9–15.
- [123] D. W. Matolak, “Channel modeling for vehicle-to-vehicle communications,” *IEEE Commun. Mag.*, vol. 46, no. 5, pp. 76–83, May 2008.
- [124] K. Pahlavan and A. Levesque, *Wireless Information Networks*. 2nd ed. NewYork: Wiley, 2005.
- [125] C.-X. Wang, M. Patzold, and D. Yuan, “Accurate and efficient simulation of multiple uncorrelated Rayleigh fading waveforms,” *IEEE Trans. Wireless Commun.*, vol. 6, no. 3, pp. 833–839, Mar. 2007.
- [126] C.-X. Wang, X. Hong, H. Wu, and W. Xu, “Spatial temporal correlation properties of the 3GPP spatial channel model and the Kronecker MIMO channel model,” *EURASIP J. Wireless Commun. Networking*, vol. 2007, Article ID 39871, 9 pages, 2007. doi:10.1155/2007/39871.
- [127] X. Cheng, C.-X. Wang, H. Wang, X. Gao, X.-H. You, D. Yuan, B. Ai, Q. Huo, L. Song, and B. Jiao, “Cooperative MIMO channel modeling and multi-link spatial correlation properties,” *IEEE J. Sel. Areas Commun.*, vol. 30, no. 2, pp. 388–396, Feb. 2012.
- [128] A. Chelli and M. Patzold, “A non-stationary MIMO vehicle-to-vehicle channel model derived from the geometrical street model,” in *Proc. IEEE VTC'11-Fall*, San Francisco, USA, Sept. 2011.
- [129] A. Chelli and M. Patzold, “A non-stationary MIMO vehicle-to-vehicle channel model based on the geometrical T-junction model,” in *Proc. IEEE WCSP'09*, Nanjing, China, Nov. 2009, pp. 1–5.
- [130] X. Cheng, Q. Yao, M. Wen, C.-X. Wang, L. Song, and B. Jiao, “Wideband channel modeling and ICI cancellation for vehicle-to-vehicle communication systems,” *IEEE J. Sel. Areas Commun.*, vol. 31, no. 9, pp. 434–448, Sept. 2013.
- [131] M. Patzold, *Mobile Radio Channels*. 2nd ed. Chichester: Wiley, 2011.

- [132] X. Cheng, C.-X. Wang, D. I. Laurenson, S. Salous, and A. V. Vasilakos, “An adaptive geometry-based stochastic model for non-isotropic MIMO mobile-to-mobile channels,” *IEEE Trans. Wireless Commun.*, vol. 8, no. 9, Sept. 2009, pp. 4824–4835.
- [133] Y. Ma and M. Patzold, “A wideband one-ring MIMO channel model under non-isotropic scattering conditions,” in *Proc. IEEE VTC’08-Spring*, Singapore, May 2008, pp. 424–429.
- [134] X. Cheng, C.-X. Wang, and D. I. Laurenson, “Multiple-ring based modeling and simulation of wideband space-time-frequency MIMO channels,” in *Proc. IEEE ICC’09*, Dresden, Germany, June 2009, pp. 4586–4590.
- [135] Y. Yuan, A. Ghazal, Q. Yao, and C.-X. Wang, “Non-stationary IMT-A MIMO channel model with time-varying AoDs and AoAs,” Huawei Project WP3 Internal Report, May 2012.
- [136] N. Youssef, C.-X. Wang, and M. Patzold, “A study on the second order statistics of Nakagami-Hoyt mobile fading channels,” *IEEE Trans. Veh. Technol.*, vol. 54, no. 4, pp. 1259–1265, July 2005.
- [137] *High speed railway channel characteristics*, draft revision to Recommendation ITU-R P.1411-7, Document 3K/143-E, Apr. 2015.
- [138] 3GPP TR 25.996 v12.0.0, “Spatial channel model for multiple input multiple output (MIMO) simulations,” Release 12, Sept. 2014.
- [139] D. S. Baum, J. Hansen, J. Salo, G. Del Galdo, M. Milojević and P. Kyosti, “An interim channel model for beyond-3G systems: extending the 3GPP spatial channel model (SCM),” in *Proc. IEEE VTC’05-Spring*, Stockholm, Sweden, May-June 2005, pp. 3132–3136.
- [140] X. Cheng, B. Yu, L. Yang, J. Zhang, G. Liu, Y. Wu, and L. Wan, “Communicating in the real world: 3D MIMO,” *IEEE Wireless Commun.*, vol. 21, no. 4, pp. 136–144, Aug. 2014.

- [141] J. Zhang, C. Pan, F. Pei, G. Liu, and X. Cheng, “Three-dimensional fading channel models: A survey of elevation angle research,” *IEEE Commun. Mag.*, vol. 52, no. 6, pp. 218–226, June 2014.
- [142] M. Shafi, M. Zhang, P. J. Smith, A. L. Moustakas, and A. F. Molisch, “The impact of elevation angle on MIMO capacity,” in *Proc. IEEE ICC’06*, Istanbul, Turkey, June 2006, pp. 4155–4160.
- [143] J. Meinila, P. Kyosti, L. Hentila, T. Jamsa, E. Suikkanen, E. Kunnari, and M. Narandzia, “D5.3: WINNER+ final channel models,” CELTIC/CP5-026, June 2010.
- [144] T. A. Thomas, F. W. Vook, E. Mellios, G. S. Hilton, A. R. Nix, and E. Visotsky, “3D Extension of the 3GPP/ITU Channel Model,” in *Proc. IEEE VTC’13-Spring*, Dresden, Germany, June 2013, pp. 1–5.
- [145] R. Almesaeed, A. S. Ameen, E. Mellios, A. Doufexi, and A. R. Nix, “A proposed 3D extension to the 3GPP/ITU channel model for 800 MHz and 2.6 GHz bands,” in *Proc. EuCAP’14*, Hague, Netherlands, Apr. 2014, pp. 3039–3043.
- [146] 3GPP TR 36.873 V12.2.0, “Study on 3D channel model for LTE,” June 2015.
- [147] B. Mondal, T. Thomas, E. Visotsky, F. Vook, A. Ghosh, Y.-H. Nam, Y. Li, J. Zhang, M. Zhang, Q. Luo, Y. Kakishima, K. Kitao, “3D channel model in 3GPP,” *IEEE Commun. Mag.*, vol. 53, no. 3, pp. 16–23, Mar. 2015.
- [148] K. V. Mardia and P. E. Jupp, *Directional Statistics*. Chichester: John Wiley & Sons, 2000.
- [149] T. Zwick, C. Fischer, D. Didascalou, and W. Wiesbeck, “A stochastic spatial channel model based on wave-propagation modeling,” *IEEE J. Sel. Areas Commun.*, vol. 18, no. 1, pp. 6–15, Jan. 2000.
- [150] S. Wu, C.-X. Wang, H. Haas, H. Aggoune, M. M. Alwakeel, and B. Ai, “A non-stationary wideband channel model for massive MIMO communication systems,” *IEEE Trans. Wireless Commun.*, vol. 14, no. 3, pp. 1434–1446, Mar. 2015.

- [151] Y. Yuan, C.-X. Wang, X. Cheng, B. Ai, and D. I. Laurenson, "Novel 3D geometry-based stochastic models for non-isotropic MIMO vehicle-to-vehicle channels", *IEEE Trans. Wireless Commun.*, vol. 13, no. 1, pp. 298–309, Jan. 2014.
- [152] C.-X. Wang, A. Ghazal, B. Ai, and P. Fan, "Channel measurements and models for high-speed train communication systems: a survey," *IEEE Commun. Surveys Tuts*, accepted for publication.
- [153] R. Almesaeed, A. S. Ameen, A. Doufexi, N. Dahnoun, and A. R. Nix, "A comparison study of 2D and 3D ITU channel model," in *Proc. IEEE Wireless Days*, Valencia, Spain, Nov. 2013, pp. 1–7.
- [154] V. Erceg, et al., IEEE 802.11 document 03/940r4, "TGn channel models," May 2004.
- [155] D. S. Baum, H. El-Sallabi, et al., "Final report on link level and system level channel models," IST-2003-507581, WINNER D5.4 v1.4, Nov. 2005.
- [156] O. Renaudin, V. M. Kolmonen, P. Vainikainen, and C. Oestges, "Non-stationary narrowband MIMO inter-vehicle channel characterization in the 5-GHz band," *IEEE Trans. Veh. Technol.*, vol. 59, no. 4, pp. 2007–2015, May 2010.
- [157] J. Karedal, F. Tufvesson, N. Czink, A. Paier, C. Dumard, T. Zemen, C. F. Mecklenbrauker, and A. F. Molisch, "A geometry-based stochastic MIMO model for vehicle-to-vehicle communications," *IEEE Trans. Wireless Commun.*, vol. 8, no. 7, pp. 3646–3657, Jul. 2009.
- [158] J. W. Wallace and M. A. Jensen, "Measurement and characterization of the time variation of indoor and outdoor MIMO channels at 2.4 and 5.2 GHz," in *Proc. IEEE VTC'05-Fall*, Dallas, USA, vol. 2, Sept. 2005, pp. 1289–1293.
- [159] J. W. Wallace and M. A. Jensen, "Time-varying MIMO channels: measurement, analysis, and modeling," *IEEE Trans. Antennas Propag.*, vol. 54, no. 11, pp. 3265–3273, Nov. 2006.

- [160] J. Karedal, F. Tufvesson, N. Czink, A. Paier, C. Dumard, T. Zemen, C. F. Mecklenbrauker, and A. F. Molisch, "Measurement-based modeling of vehicle-to-vehicle MIMO channels," in *Proc. IEEE ICC'09*, Dresden, Germany, June 2009, pp. 1-6.
- [161] S. Knorzer, M. A. Baldauf, T. Fugen, and W. Wiesbeck, "Channel analysis for an OFDM-MISO train communications system using different antennas," in *Proc. IEEE VTC'07-Fall*, Baltimore, USA, Oct. 2007, pp. 809–813.
- [162] I. Sen and D. W. Matolak, "Vehicle-vehicle channel models for the 5-GHz band," *IEEE Trans. Intell. Transp. Syst.*, vol. 9, no. 2, pp. 235–245, June 2008.
- [163] H. Xiao, A. G. Burr, and L. Song, "A time-variant wideband spatial channel model based on the 3GPP model," in *Proc. IEEE VTC'06-Fall*, Montreal, Canada, Sept. 2006, pp. 1–5.
- [164] S. Wu, C.-X. Wang, H. Aggoune, M. M. Alwakeel, and Y. He, "A non-stationary 3D wideband twin-cluster model for 5G massive MIMO channels," *IEEE J. Sel. Areas Commun.*, vol. 32, no. 6, pp. 1207–1218, June 2014.
- [165] Q. Yao, Y. Yuan, A. Ghazal, C.-X. Wang, L. Luan, and X. Lu, "Comparison of the statistical properties of the LTE-A and IMT-A channel models," in *Proc. IEEE WCNC'12*, Paris, France, Apr. 2012, pp. 393–398.
- [166] P. Liu, B. Ai, Z. Zhong, and X. Zhou, "A novel train-to-train communication model design based on multihop in high-speed railway," *Int. J. Antennas and Propag.*, vol. 2012, Article ID 475492, 9 pages, 2012. doi:10.1155/2012/475492.
- [167] P. Liu, X. Zhou, and Z. Zhong, "Outage analysis of train-to-train communication model over Nakagami- m channel in high-speed railway," *Int. J. Antennas Propag.*, vol. 2013, Article ID 617895, 10 pages, 2013. doi:10.1155/2013/617895.
- [168] E. Larsson, O. Edfors, F. Tufvesson, and T. Marzetta, "Massive MIMO for next generation wireless systems," *IEEE Commun. Mag.*, vol. 52, no. 2, pp. 186–195, Feb. 2014.